OBSERVATIONS AND MODELLING OF DEEP EQUATORIAL CURRENTS IN THE CENTRAL PACIFIC

by

Rui Vasques de Melo Ponte

B.S., University of Rhode Island
(1982)

M.S., Massachusetts Institute of Technology
(1985)

SUBMITTED IN PARTIAL FULFILLMENT OF THE
REQUIREMENTS FOR THE DEGREE OF

DOCTOR OF PHILOSOPHY

at the

MASSACHUSETTS INSTITUTE OF TECHNOLOGY

and the

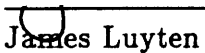WOODS HOLE OCEANOGRAPHIC INSTITUTION

January, 1988

©Rui V. D. M. Ponte 1988

Signature of the author

Joint Program in Oceanography,
Massachusetts Institute of Technology –
Woods Hole Oceanographic Institution

Certified by

James Luyten
Thesis supervisor

Accepted by

Joseph Pedlosky
Chairman, Joint Committee for Physical Oceanography.
Massachusetts Institute of Technology –
Woods Hole Oceanographic Institution.

Observations and Modelling of Deep Equatorial Currents
in the Central Pacific

by

Rui Vasques de Melo Ponte

Abstract

Analysis of vertical profiles of absolute horizontal velocity collected in January 1981, February 1982 and April 1982 in the central equatorial Pacific as part of the Pacific Equatorial Ocean Dynamics (PEQUOD) program, revealed two significant narrow band spectral peaks in the zonal velocity records, centered at vertical wavelengths of 560 and 350 stretched meters (sm). Both signals were present in all three cruises, but the 350 sm peak showed a more steady character in amplitude and a higher signal-to-noise ratio. In addition, its vertical scales corresponded to the scales of the conspicuous alternating flows generically called the equatorial deep jets in the past (the same terminology will be used here). Meridional velocity and vertical displacement spectra did not show any such energetic features.

Energy in the 560 sm band roughly doubled between January 1981 and April 1982. Time lagged coherence results suggested upward phase propagation at time scales of about 4 years. East-west phase lines computed from zonally lagged coherences, tilted downward towards the west, implying westward phase propagation. Estimates of zonal wavelength (on the order of 10000 km) and period based on these coherence calculations, and the observed energy meridional structure at this vertical wavenumber band, seem consistent, within experimental errors, with the presence of a first meridional mode long Rossby wave packet, weakly modulated in the zonal direction.

The equatorial deep jets, identified with the peak centered at 350 sm, are best defined as a finite narrow band process in vertical wavenumber (311-400 sm), accounting for only 20% of the total variance present in the broad band energetic background. At the jets wavenumber band, latitudinal energy scaling compared well with Kelvin wave theoretical values and a general tilt of phase lines downward towards the east yielded estimates of 10000-16000 km for the zonal wavelengths. Time-lagged coherence calculations revealed evidence for vertical shifting of the jets on interannual time scales. Interpretation of results in terms of single frequency linear wave processes led to inconsistencies, but finite bandwidth (in frequency and wavenumber) Kelvin wave processes of periods on the order of three to five years could account for the observations. Thus, the records do not preclude equatorial waves as a reasonable kinematic description of the jets.

At all wavenumber bands in general, power levels decayed away from the equator over scales broader than the Kelvin wave scale, suggesting the presence of Rossby wave energy. Cross-spectral analysis showed Rossby and Kelvin wave motions to be dominant at the equator over the 933 sm and the 140-400 sm vertical wavelength bands, respectively. The latter agrees with the findings of Eriksen (1981) in the western Pacific, and thus seems to be a climatological feature of the deep equatorial Pacific fields.

In an attempt to model the observed zonal velocity signals, alternative forcing mechanisms for the deep ocean (other than direct surface winds) were tried. The probable presence of deep energy sources at the ocean side walls (e.g., Kawase, 1987) was explored by considering the linear response of an equatorial ocean to a time varying zonal jet placed at the lateral boundaries. In another simple model, we examined the character of stationary Kelvin wave solutions obtained in the presence of vertically sheared mean westward flows. In this case, the waves are forced below the thermocline by a vertical velocity representing large scale convergence or divergence patterns associated with the upper ocean circulation. Results suggest that both ideas remain potentially important to the existence of deep baroclinic currents in the equatorial ocean.

Thesis supervisor: Dr. James Luyten
Senior Scientist
Woods Hole Oceanographic Institution

Table of contents

CHAPTER 1
Introduction

In recent years, considerable attention has been given to the study of the tropical ocean-atmosphere system, in an effort to improve understanding of the El Niño /Southern Oscillation phenomena. The strong interannual and seasonal variability is one of the distinct features of the tropical regions (especially the Pacific). But the ocean circulation in the equatorial band differs in many other aspects from mid-latitude flow regimes, exhibiting a variety of spatial and temporal scales and a complex pattern of mean zonal currents and countercurrents not seen at higher latitudes (see, e.g., Firing, 1987). The rich current structure is not confined to the upper layers, but seems to extend to the deep ocean as well (Luyten and Swallow, 1976; Eriksen, 1981; Firing, 1987). From a theoretical point of view, the equator is dynamically different because of the vanishing and change in sign of the vertical component of the earth's rotation vector. This fact implies in general the breakdown of geostrophy and permits the existence of equatorially trapped waves. Unlike mid-latitudes, where there is a frequency gap between Rossby and gravity waves where no free oscillations can occur, at the equator, free waves exist at all periods, with the additional presence of Kelvin and mixed-Rossby modes.

Equatorially trapped waves can carry energy from the more actively forced surface layers to the ocean's interior. Such is the case in the atmosphere, where Kelvin and mixed-Rossby waves propagating energy upward from the troposphere have been observed in the stratosphere (e.g., Holton, 1975). Furthermore, the interaction between these waves and the mean zonal winds is the mechanism behind the quasi-biennial oscillation seen in the tropical atmosphere (e.g., Holton, 1975). This phenomenon illustrates how dissipation of wave energy leads to the generation of mean flows. The enhancement in dissipation rates occurring near critical layers (where the vertical group

speed of the waves vanish) may cause the waves to deposit their momentum in regions far from where they are forced, depending on where the critical level occurs. These are some of the reasons why it is important to determine the existence of equatorial waves in the deep ocean.

Although the oceanic observational data base is not nearly as complete as the atmospheric one, several studies have tried to interpret deep equatorial velocity records as being associated with equatorially trapped waves. Eriksen (1980, 1981) emphasized the statistical approach by attempting to describe the deep fields in terms of broad band spectral sums of equatorial wave modes, much like Garrett and Munk (1979) did for mid-latitude internal waves. Others (e.g., O'Neill, 1982; Lukas and Firing, 1985) were able to identify the presence of single wave modes in their records. Although these and other researchers had some success in relating the observations to linear equatorial waves, much more data was clearly needed before one was able to describe the average state of the deep ocean fields.

An interesting aspect of the deep equatorial circulation is the presence of strong, alternating zonal currents closely trapped to the equator, and with vertical scales on the order of 100 m. These energetic flows, usually called the equatorial deep jets (EDJ), were first observed by Luyten and Swallow (1976) in the Western Indian ocean. The basic structure of the velocity field did not change during one month of observations, suggesting time scales larger than a few months. This prompted Wunsch (1977) to construct a simple model that could account for the jet-like flows. The alternating jets in his solutions consisted of vertically propagating long Rossby waves forced at the surface at annual or semiannual period.

A more extensive treatment of the Indian ocean data set, carried out by O'Neill (1982) confirmed earlier findings but revealed some contradictions between the records and Wunsch's model results. In particular, the hypothesis of a first meridional mode

7

long Rossby wave originally suggested by Wunsch (1977) did not fit the observed merid-
ional structure of the jets. The proximity of the slanting coast of East Africa was
invoked as a probable reason for the discrepancies between the linear wave theory and
the records. The lack of sufficient time and zonal coverage in the data made it impos-
sible to estimate the zonal and time scales of the jets, thus affecting the theoretical
interpretation.

Since their discovery, EDJ have also been observed in the Pacific. A number of
profiles made at 110°W (Hayes and Milburn, 1980) indicated high vertical mode deep
currents with zonal velocities of up to 20 cm/s at a depth of 1500 m. A more interesting
set of observations was obtained by Leetmaa and Spain (1981). Their series of velocity
profiles along the equator, from 125°W to 159°W, revealed short vertical wavelength
(300 m) structures, persistent over the whole longitudinal extent of the records, thus
suggesting very long zonal scales for the EDJ. Assuming that linear equatorial waves
were responsible for the observed currents, they used rough estimates of 6000 km and
300 m for the zonal and vertical wavelengths to hint at the presence in the data of a
Kelvin wave with period of about two years or a Rossby wave with period of about six
years.

A more extensive data set on the deep velocity fields was collected by Eriksen
(1981) in the Western Pacific, near the Gilbert islands. Vertical profiles of current and
density made within 5° latitude of the equator, from 168°E to 179°E, showed again the
same multiple cell structure of alternating zonal flows with short vertical scales, but the
time scales were still not resolved by the one month long records. Based on coherence
calculations showing zonal current lagging vertical displacement by $\pi/2$ with depth,
Eriksen inferred the presence of Kelvin waves in the records. In a later paper, Eriksen
(1982) compared geostrophic velocities with direct current measurements finding rea-
sonable agreement between them at latitudes within 1° of the equator. This agreement

seemed to corroborate the Kelvin wave hypothesis advanced earlier as a possible explanation of the EDJ. In addition, analysis of GEOSECS data from the Atlantic ocean revealed enhancement of potential energy at the equator, a fact suggesting the presence of these Kelvin waves (and consequently deep jets in his interpretation) in the Atlantic as well. However, to obtain statistical reliability in his spectral and cross-spectral analysis, Eriksen had to average over several vertical wavenumber bands, with inherent loss of resolution (perhaps because of this averaging, the apparent narrow band character of the EDJ in vertical wavenumber, as seen in the raw records, did not translate into a visible peak in the vertical wavenumber power spectrum). Therefore, it was not clear whether his results represented a description of the deep jets, or instead reflected the characteristics of the broad band background.

These earlier studies on the jets stimulated interest in the deep equatorial circulation and demonstrated the need for better observational data, if one were to have a clear picture of the spatial and temporal scales of the EDJ, or be able to differentiate between the mean and time dependent circulation in general. Several other interesting questions about the EDJ remained unanswered. What was the energy source for these strong flows? Was their vertical scale set by a peak in the forcing or by some resonance mechanism? The Pacific Equatorial Ocean Dynamics (PEQUOD) experiment which took place during the years 1981 through 1983, was designed to clarify some of these issues. The program included a moored current meter array (Eriksen, 1985), a 16 month time series of vertical profiles of horizontal velocity along 159°W (Firing, 1987), and a series of 76 vertical profiles of horizontal velocity taken during three different months (January 1981, February and April 1982), in a spatial array intended to provide good latitudinal and longitudinal coverage of the EDJ. It is this last data set which will be considered here. A complete description of the data and its general treatment is given in Chapter 2.

The interpretation of the EDJ as vertically propagating equatorial waves was generally accepted in light of the data available prior to PEQUOD, but the existing records could not resolve their time and space scales. The PEQUOD data set provided the best opportunity to test the validity of the linear wave hypothesis advanced earlier by several studies (e.g., Wunsch, 1977; Eriksen, 1981; McCreary, 1984). The records assured a better resolution of the vertical and zonal structure of the deep flows. Unlike earlier studies (e.g., Eriksen, 1981), there were enough realizations of the data so that the conspicuous dominant vertical scale of the jets should be brought out of the background "noise". The temporal lags between cruises were also long enough to check for vertical phase propagation at scales on the order of one year or longer. One of the main purposes of this work is to determine whether the PEQUOD profiler records support the general wave hypothesis, by investigating if the observed spatial and temporal scales of the jets (or any other energetic signals present) correspond to a point (or a region) in the dispersion curves for equatorially trapped waves. This constitutes Chapter 3 of this dissertation.

In addition to providing a better description of the jets, the PEQUOD data set represented the best realization of the average characteristics of deep equatorial fields over a broad range of vertical scales, at least for the central Pacific ocean. With the collection of similar records in the future, one may start to look for a wave climatology of the deep equatorial ocean by comparing different observations and searching for common features between them. As a first step in that direction, the extent to which the general deep fields observed during PEQUOD can be explained in terms of equatorial waves is examined in Chapter 4. A comparison of our results with earlier ones (Eriksen, 1981) is also carried out.

The theoretical work of Chapter 5 is motivated in part by the PEQUOD observations and by recent studies related to the deep equatorial circulation (McCreary and

Lukas, 1986; Kawase, 1987). Most tentative explanations of the EDJ involved low frequency waves, but the existence of such waves in the deep ocean had been questioned on several grounds. Because energy rays associated with such waves descend from the surface at very small angles to the horizontal (McCreary, 1984), it is difficult to get energy at these long periods to propagate to great depth. On the other hand, waves of short vertical scales may be strongly absorbed at critical layers existing near the surface, where strong vertically sheared mean flows occur (McPhaden *et al.*, 1986). Therefore, it is difficult to accept that features such as the EDJ are associated with low frequency waves forced by the wind at the ocean surface.

Chapter 5 is an attempt to circumvent these problems by considering other possible forcing mechanisms for the deep ocean. Kawase (1987) showed that the circulation induced by an off-equatorial mass source located at the western boundary included a strong equatorial zonal component. This suggested a connection between deep energy sources, possibly located at lateral oceanic boundaries, and the existence of low frequency motions in the interior. In another development, McCreary and Lukas (1986) suggested that stationary Kelvin waves could perhaps be related to the existence of jets in the deep ocean. In their model, the stationary waves were forced by a steady wind patch acting on an ocean with a mean westward flow constant from top to bottom, but for deep ocean solutions qualitatively resembling the observations, the upper ocean currents were very unrealistic. In addition, the mean flow they assumed was not really representative of the upper ocean mean circulation. This result led us to consider instead putting the forcing at the base of the thermocline to mimic processes such as convergence or divergence patterns associated with upper ocean currents, as suggested in Philander and Pacanowski (1981). Since deep mean zonal flows (if they do indeed exist) are expected to have large scale vertical shear compared to the scale of the jets for example, one can then use the method of multiple scales described in

Lindzen (1971) to examine the effect of mean vertical shear on the stationary wave solutions.

The final chapter provides a summary of the main conclusions from the data analysis and the theoretical work, along with a general discussion of the paths which could perhaps be followed in the future to improve our understanding of the EDJ in particular, and of the equatorial deep circulation in general. To prevent possible false expectations, perhaps we should warn the reader that, from either the observational or the theoretical point of view, no ultimate answers will be found in this work. Instead, and perhaps more important, a number of new questions will be raised. Such is the usual reward of the scientific enterprise.

CHAPTER 2
The PEQUOD Observations and General Data Analysis

2.1 Field work and instrumentation

The observational data which will be treated and analysed here consists of 77 vertical profiles of horizontal velocity, pressure, temperature and conductivity (salinity), collected during 3 cruises to the central Pacific which took place on January 1981, February 1982 and April 1982. The profiles were obtained at 17 different sites along and across the equator, as shown in Fig. 2.1. The array spans 15° of longitude and roughly 6° of latitude. It was intended to provide a good observational basis to determine the meridional and zonal scales of the EDJ. Most of the sites were occupied more than once during each cruise. Casts were repeated at all 3 cruises, providing the possibility for looking at the vertical propagation (if any) of the deep jets over relatively long periods, compared with the previous records available. A summary of all the casts made at each site is given in Table 2.1.

The instrument used in collecting the data was the White Horse profiler, a freefall acoustic dropsonde also employed by Luyten and Swallow (1976) and Eriksen (1981) in earlier observations of the deep jets. The instrument is tracked acoustically by means of 3 transponders placed on the ocean floor. These transponders were deployed during the first cruise, and left there for subsequent observations. Their absolute positions were determined by performing an acoustic survey from the surface, as described in O'Neill (1982). The orientation of the transponder network is determined to within ± 5°.

The characteristics of the White Horse profiler and its performance are discussed in detail in a paper by Luyten *et al.* (1982). As the instrument moves up or down the water column at a rate of approximately 1 m/s, it interrogates the transponder network, storing the time intervals between interrogation and reply on a magnetic tape.

13
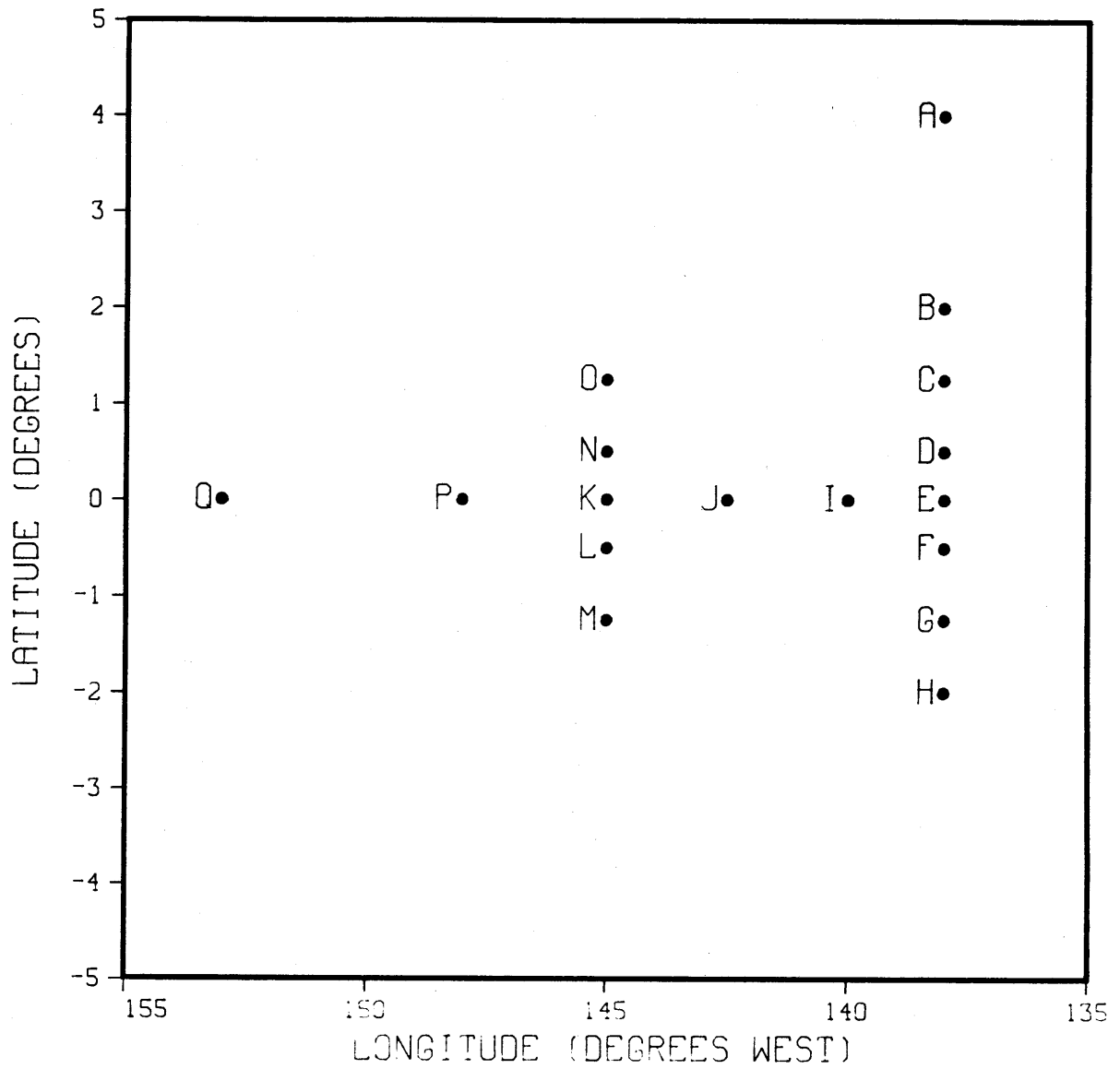
Fig 2.1 Spatial distribution of the 17 sites occupied during PEQUOD.

Table 2.1. Summary of the casts made during the PEQUOD program. Longitude and latitude are given in degrees.

Profile	Longitude	Latitude	Date
A01-03	138.05 W	4.02 N	14/Jan/81; 7/Feb/82; 10/Apr/82
B01-03	138.02 W	2.04 N	15/Jan/81; 7/Feb/82; 11/Apr/82
C01-03	138.02 W	1.23 N	16/Jan/81; 8/Feb/82; 11/Apr/82
D01-03	138.00 W	0.51 N	16/Jan/81; 8/Feb/82; 12/Apr/82
E01-03	137.96 W	0.04 N	17/Jan/81; 9/Feb/82; 12/Apr/82
F01-03	137.95 W	0.45 S	18/Jan/81; 9/Feb/82; 13/Apr/82
G01-03	137.96 W	1.20 S	18/Jan/81; 10/Feb/82; 13/Apr/82
H01-03	138.00 W	1.95 S	19/Jan/81; 10/Feb/82; 13/Apr/82
I01,03,04	140.03 W	0.03 N	20/Jan/81; 11/Feb/82; 14/Apr/82
J01	142.48 W	0.00	20/Jan/81
J02-J05	142.48 W	0.00	12,18/Feb/82; 15,20/Feb/82
K01-K04	145.05 W	0.03 N	22,24,26,28/Jan/81
K05-07	145.05 W	0.03 N	15,20,21/Feb/82
K08-09	145.05 W	0.03 N	16,22/Apr/82
L01,02,04	144.95 W	0.55 S	22,23,28/Jan/81
L05,07	144.95 W	0.55 S	14,20/Feb/82
L08-09	144.95 W	0.55 S	16,21/Apr/82
M01-04	144.96 W	1.3 S	23,27/Jan/81; 14,19/Feb/82
M05-06	144.96 W	1.3 S	16,21/Apr/82
N01-04	144.97 W	0.51 N	25,26,29/Jan/81; 16/Feb/82
N06-07	144.97 W	0.51 N	16,22/Apr/82
O01	145.00 W	1.27 N	25/Jan/81
O02-05	145.00 W	1.27 N	16,21/Feb/82; 17,22/Apr/82
P01,03	148.00 W	0.00	30/Jan/81; 23/Feb/82
P04,07	148.00 W	0.00	18,24/Apr/82
Q01	153.00 W	0.00	24/Feb/82
Q03-09	153.00 W	0.00	26,27/Apr/82

The raw acoustic travel times are then converted to ranges from the profiler to each transponder by using the local sound speed profile, computed from the data collected by the CTD mounted on the instrument. This way, the three dimensional position of the dropsonde is known, and its horizontal deviations as it travels vertically in the water column essentially give the horizontal transport averaged over roughly 15 vertical meters. Velocity measurements can be obtained with an accuracy of $\pm 4\,cm/s$ over 25 m depth intervals. Each White Horse cast provides 2 vertical profiles of velocity (one on its descent, the other on its ascent).

Temperature, pressure and conductivity were sampled every second, with measurement uncertainties of $0.003°$ C, 2 db and 0.005 ppt (parts per thousand) respectively (Voorhis $et\ al.$, 1984). Only CTD data from the down trace was used, since on the up trace the CTD was in the wake of the instrument. This data was used to calculate buoyancy and vertical displacement profiles, as described later in this chapter.

2.2 CTD and velocity data — initial treatement

A – Velocity Data

Conversion of acoustic travel times to horizontal velocity profiles was done by G. Needell at the Woods Hole Oceanographic Institution (WHOI). The two profiles (up and down trace) obtained for each cast were averaged together, and then interpolated at 25 m depth intervals. The averaging cuts down the noise and does not affect any motions with periods long compared to a couple of hours.

Plots of zonal and meridional velocities shown in Figs. 2.2-2.5 immediately reveal some qualitative features of our data set. The Equatorial Undercurrent (EUC) is clearly seen flowing eastward in the upper ocean. The alternating eastward and westward flows below the EUC are generally thought to be the EDJ. These deep flows seem to be coherent over at least 10° of longitude, as observed by Leetmaa and Spain (1981), and very strongly trapped to the equator. For off-equatorial casts, the zonal velocity records are dominated by low baroclinic mode flows, as expected from simple equatorial linear wave theory arguments (i.e., the shorter the vertical scale, the stronger the trapping to the equator).

A rather surprising observation is the apparent stationarity of some of the jets over the duration of the PEQUOD program. In particular, the strong westward flow at roughly 1500 m is not seen to move up or down over the 16 month period from January 1981 to April 1982. The records seem to suggest long time and space scales associated with zonal velocity flows, contrasting with the high variability present in the meridional velocity profiles in general. More quantitative statements about these assertions require the use of conventional spectral techniques and will be left for the next chapters.

B – Calculation of Buoyancy Frequency Profiles

Fig. 2.2. Zonal velocity along a longitudinal section at the equator, taken during the April 1982 cruise. All casts collected at each site were averaged together.

18
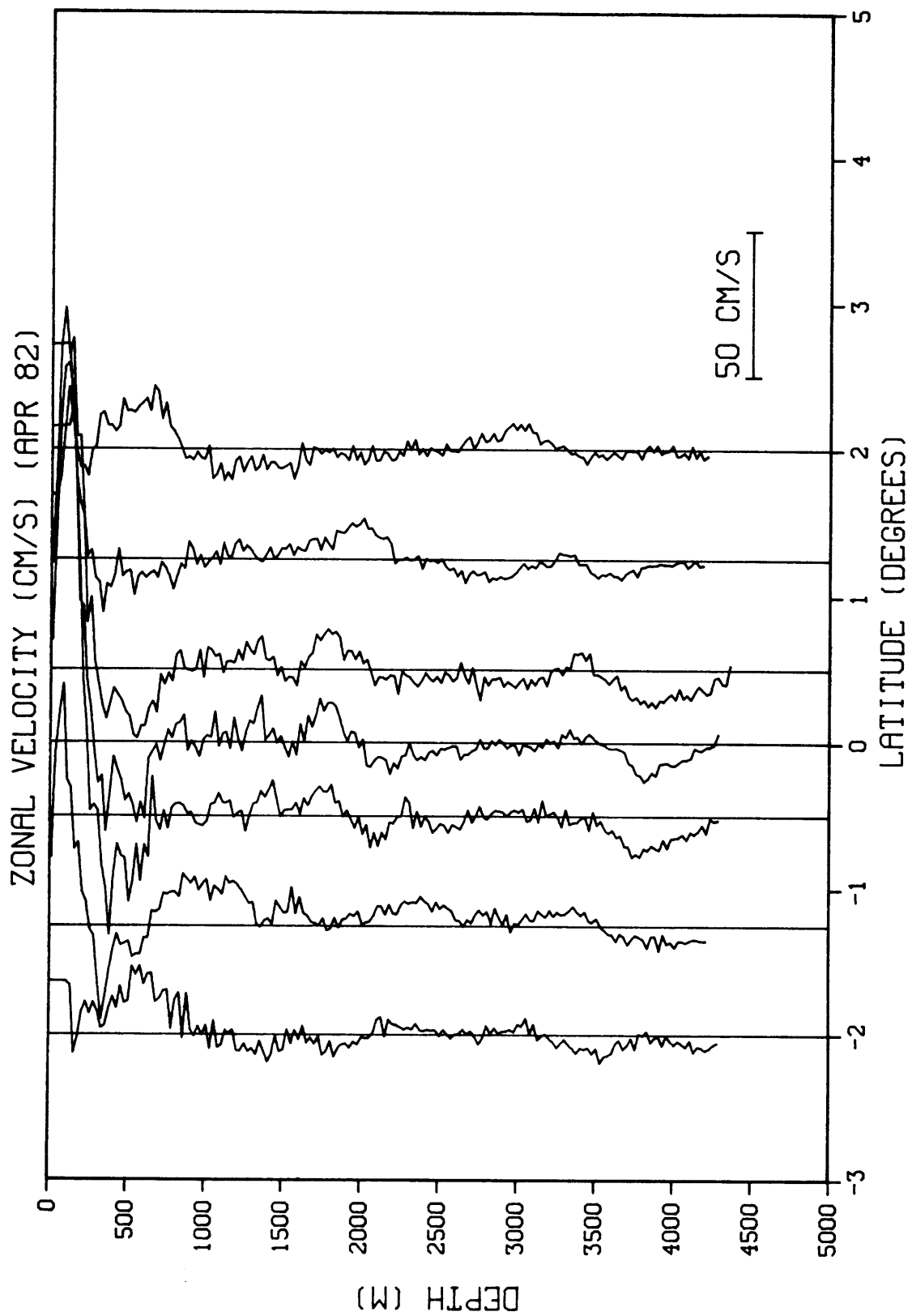
Fig. 2.3. Zonal velocity along a latitudinal section at 138°W, taken during the April 1982 cruise. There was no velocity data from site A at 4°N.
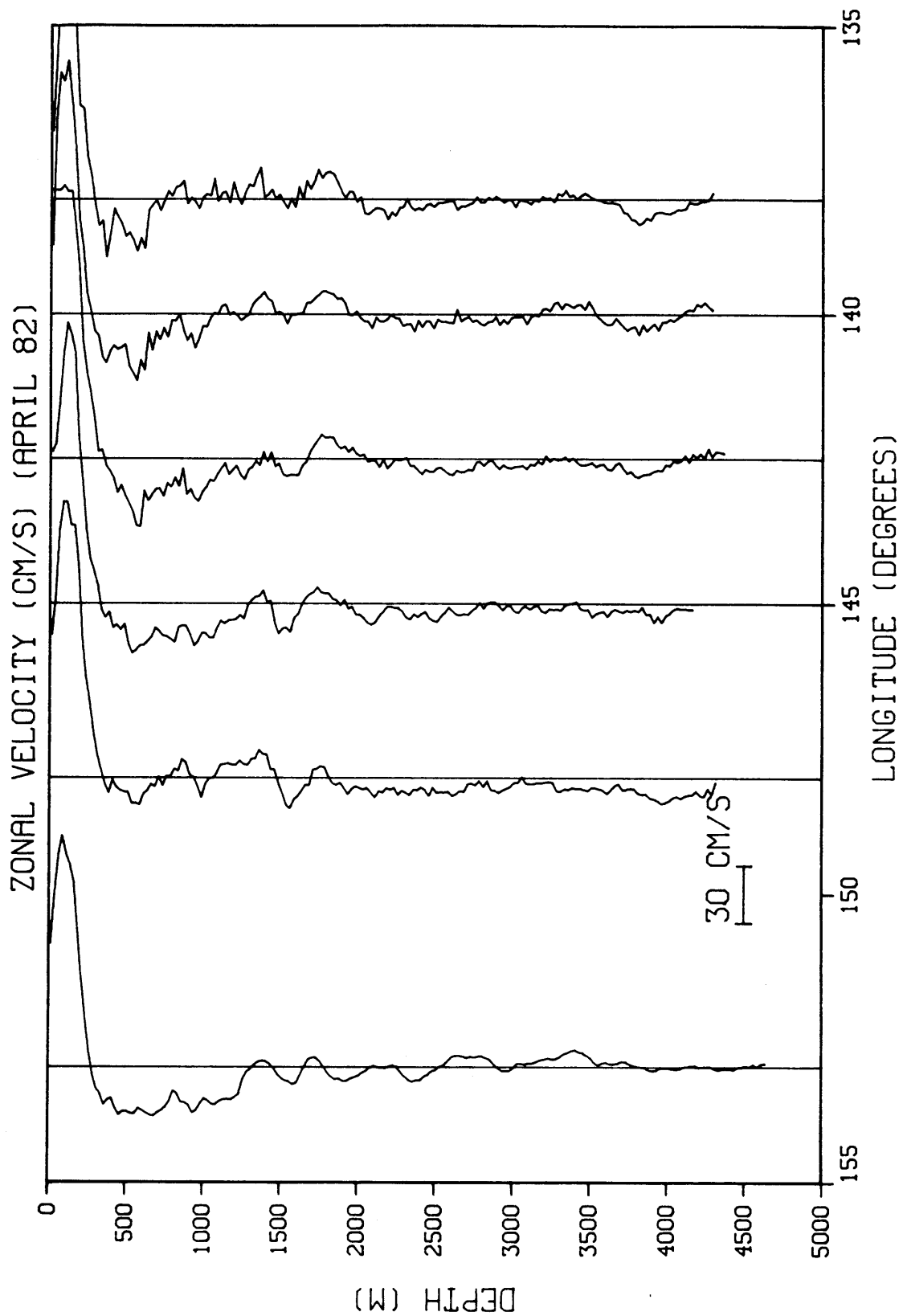
19
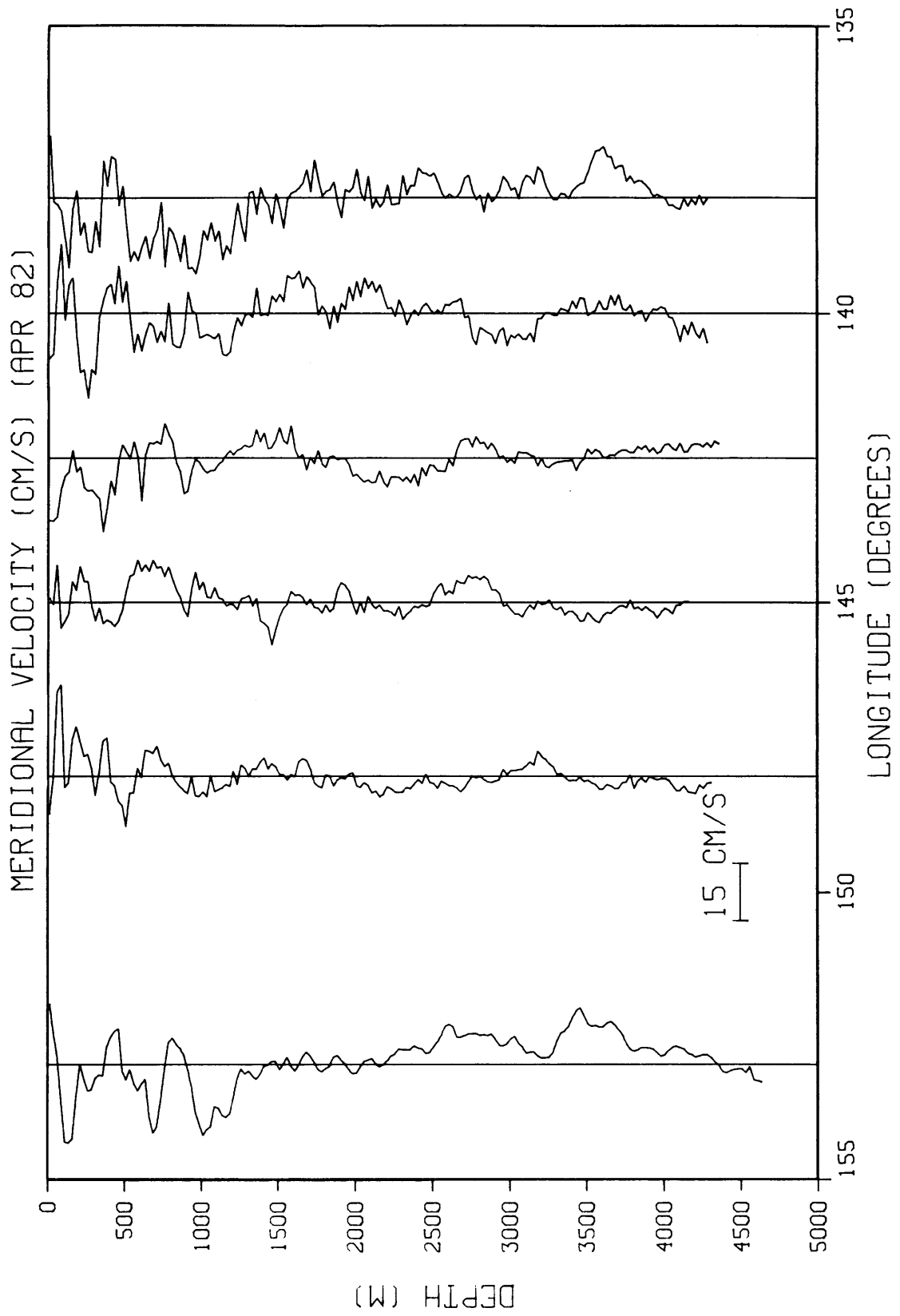
Fig. 2.4. Meridional velocity along a longitudinal section at the equator, taken during the April 1982 cruise. All casts collected at same site were averaged together.
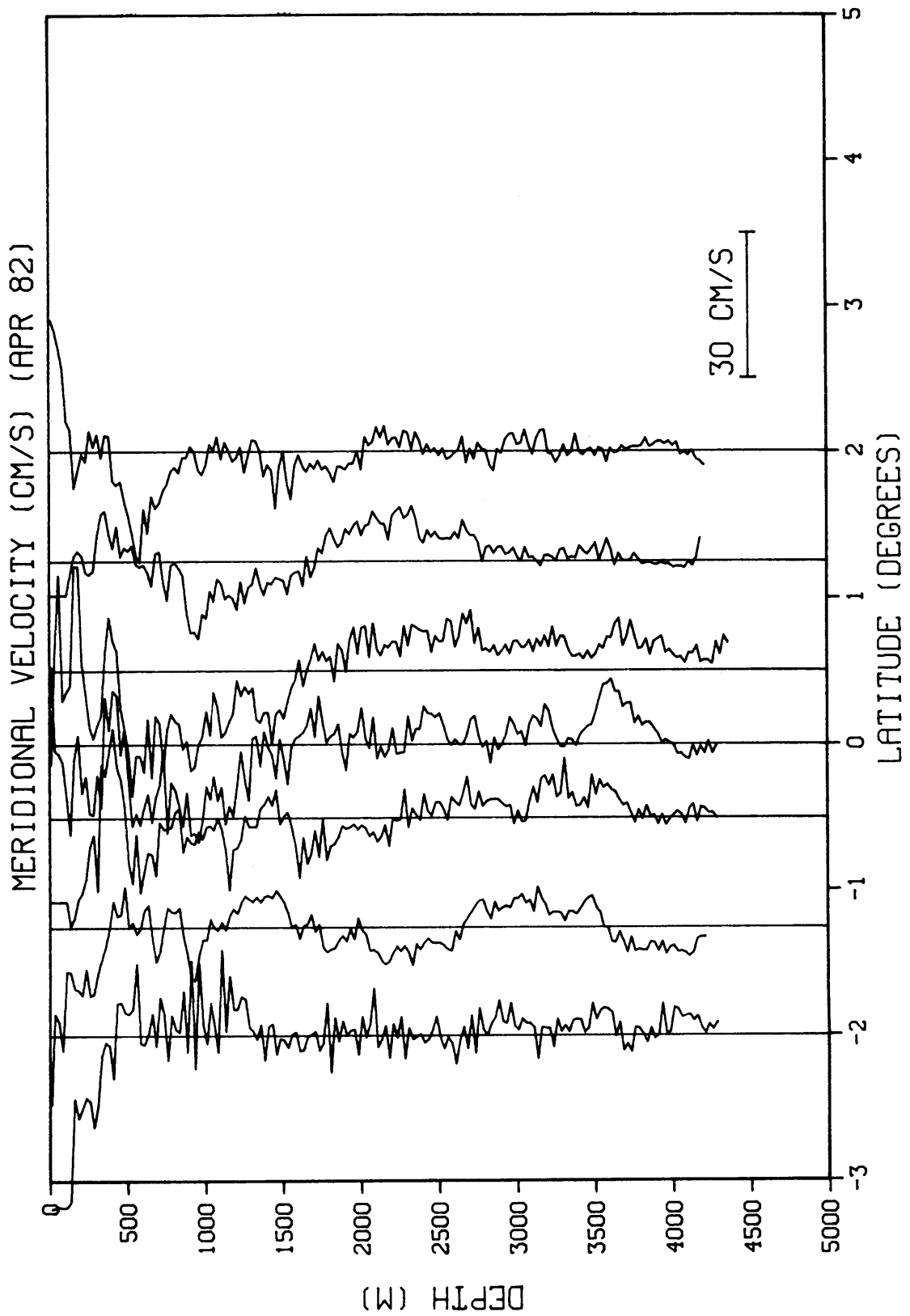
Fig. 2.5. Meridional velocity along a latitudinal section at 138°W, taken during the April 1982 cruise.

The temperature and salinity data was previously interpolated to 2 db pressure intervals by G. Needell. Buoyancy frequency profiles $N(z)$ (expression for $N(z)$ is given in Appendix A) are needed to carry out the spectral analysis of the data, as described below. The following strategy was used in calculating $N(z)$ profiles. For each cast, $N(z)$ was computed using a linear least squares fit of specific volume over 10 db at the top, and 50 db below 1000 db. This choice of pressure bins was more or less arbitrary, but it provided enough vertical averaging to kill the artificially unstable values of $N(z)$ (i.e., $\rho_z > 0$) which are introduced by noise in the temperature and salinity measurements, while keeping the strong and thin pycnocline well resolved. Use of longer pressure bins did not significantly alter the results. We then assumed that any spatial differences between profiles was essentially due to noise, and averaged horizontally over all profiles obtained during each particular cruise. Indeed, each individual $N(z)$ profile did not look much different from the others, so that the procedure was justified. At depth, fewer points were taken in the average because of the different vertical extent of each cast. Plots of the averaged $\bar{N}(z)$ for the January 1981, February 1982 and April 1982 cruises are shown in Fig. 2.6. These were used in the stretching and scaling procedure described in the next section. They are not substantially different, especially below 500 m. Also shown in Fig. 2.6 is the profile obtained by averaging in time over all 3 cruises, which was needed for spectral analysis involving casts from different cruises.

C – Calculation of Vertical Displacement

Profiles of vertical displacement are not directly measured by the White Horse instrument, but can in general be inferred from the CTD data set, as described in detail by O'Neill (1982). Basically, the deviations of the density profile from its temporal mean are assumed to be caused by the vertical advection associated with wave motions, in the presence of a vertical density gradient (see equation $(A.1d)$ in Appendix A). This
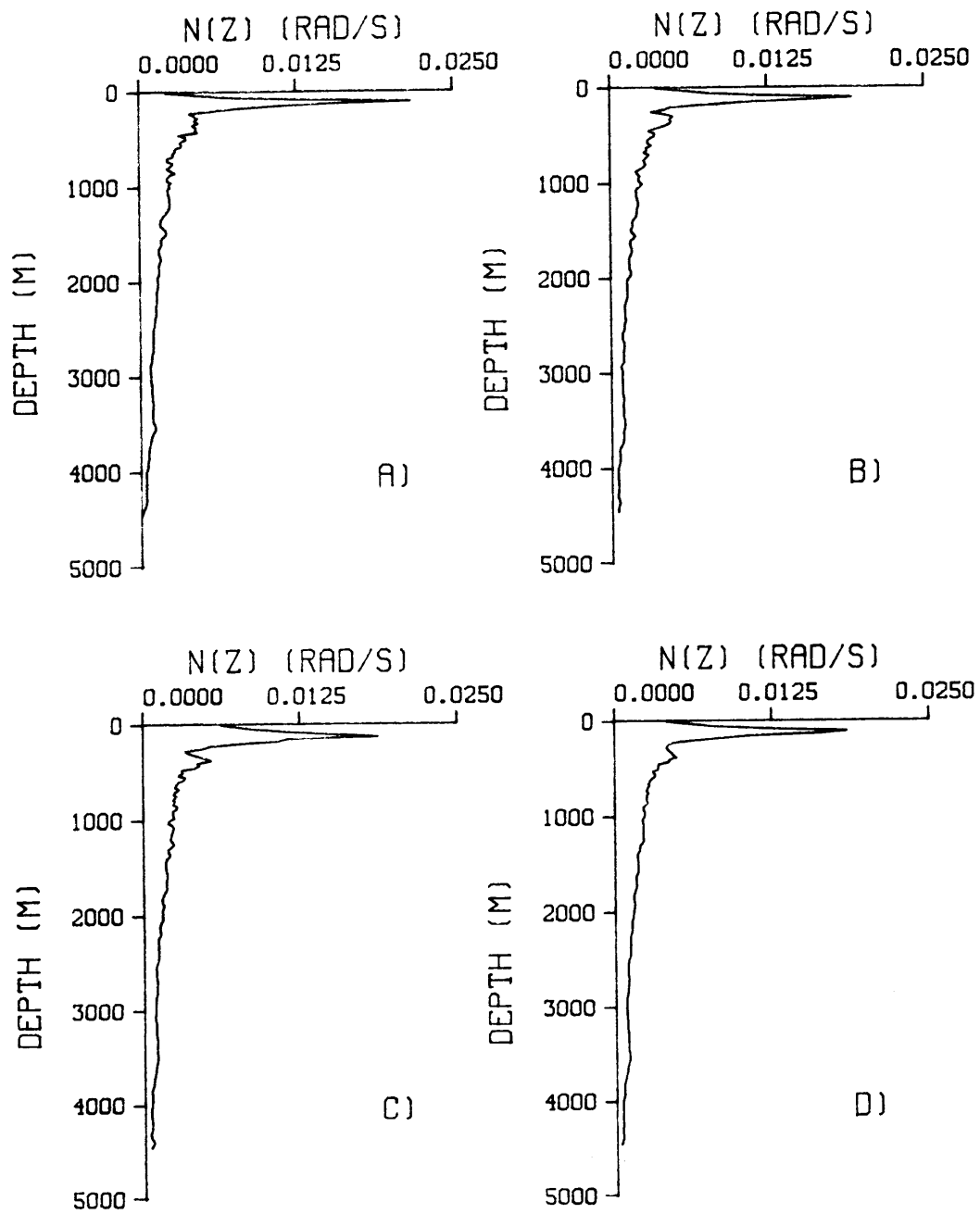
Fig. 2.6. Buoyancy profiles computed for a) January 1981, b) February 1982, c) April 1982 and d) time average of other three profiles.

method is frequently used in internal wave studies. Referring to equation $(A.1d)$, if we integrate in time and use the relation

$$w = \frac{d\varsigma}{dt} \qquad (2.1)$$

where ς is vertical displacement, then we obtain

$$\varsigma = \frac{\rho - \rho'}{\rho_z} \qquad (2.2)$$

Here, ρ' is the observed density value and ρ is the mean which we will define below. In terms of the specific volume $\delta = 1/\rho$, and using the hydrostatic relation to convert δ_z to δ_p, expression (2.2) becomes

$$\varsigma = \frac{\delta^3}{g} \left(\frac{\delta^{-1} - \delta'^{-1}}{\delta_p} \right) \qquad (2.3)$$

Vertical displacement ς has the same sign of the difference $\delta'^{-1} - \delta^{-1}$ as it should (positive ς implies denser fluid from below has been displaced upward and vice-versa).

In calculating vertical displacement using (2.3), we follow a similar route to that used in section 2.2, when computing $N(z)$. The quantities δ', δ and δ_p were calculated as follows:

δ' — linear fit over 10 db pressure bins down to 1000 db, and 50 db below.

δ — average horizontally all the 77 CTD casts.

δ_p — average horizontally all the slopes obtained from linear fit over each bin, for every cast.

Records were interpolated to 25 m depth intervals using cubic splines, and cut to the length of the shortest cast available. How well the mean quantities δ and δ_p are determined from the data is a crucial question here. We took the best realization of the mean by averaging all CTD data, but it is clear that inferences on long time scales from these vertical displacement records may lead to erroneous conclusions. Plots of

some of the ς profiles created this way can be seen in Fig. 2.7. They show in general more variance than the velocity records, with large values occurring sporadically due to the noisy character of the procedure outlined above. As we get deeper in the water column, noise is enhanced because the denominator in (2.3), δ_p, becomes smaller.

2.3 WKBJ approximation — Stretching and scaling procedure

The stretching and scaling procedure (abbreviated as S/S, hereafter) used by Eriksen (1981), O'Neill (1982), and many others, was applied to the velocity and vertical displacement data. The procedure is based on the validity of the WKBJ solutions to the vertical structure equation (A.3) given in the context of the linear equatorial wave theory revisited in Appendix A. Any more complicated equatorial ocean models (e.g., linear waves in mean shear flows) will not in general have separable solutions in y–z. Thus, in using S/S procedure, we implicitly assume that to a first approximation the records consist of linear waves describable by the theory of Appendix A. The method has worked reasonably well in previous studies (e.g., Eriksen,1985).

The WKBJ solutions $G(z)$ to the vertical structure equation (A.3) for variable $N(z)$ are

$$G \sim \left[\frac{c_n}{N(z)}\right]^{1/2} \exp\{i \int \frac{N(z)}{c_n} dz\} \tag{2.4}$$

or by making the substitution $N_0 = c_n m_0$, with N_0 being an arbitrary reference buoyancy frequency,

$$G \sim \left[\frac{N_0}{m_0 N(z)}\right]^{1/2} \exp\{i m_0 \int \frac{N(z)}{N_0} dz\} \tag{2.5}$$

suggesting the vertical coordinate transformation

$$dz^* = \frac{N(z)}{N_0} dz. \tag{2.6}$$

In this stretched coordinate, the phase of the solution will be same as for an ocean with $N = N_0 = $ constant. Furthermore, scaling the amplitude of the solution by the factor
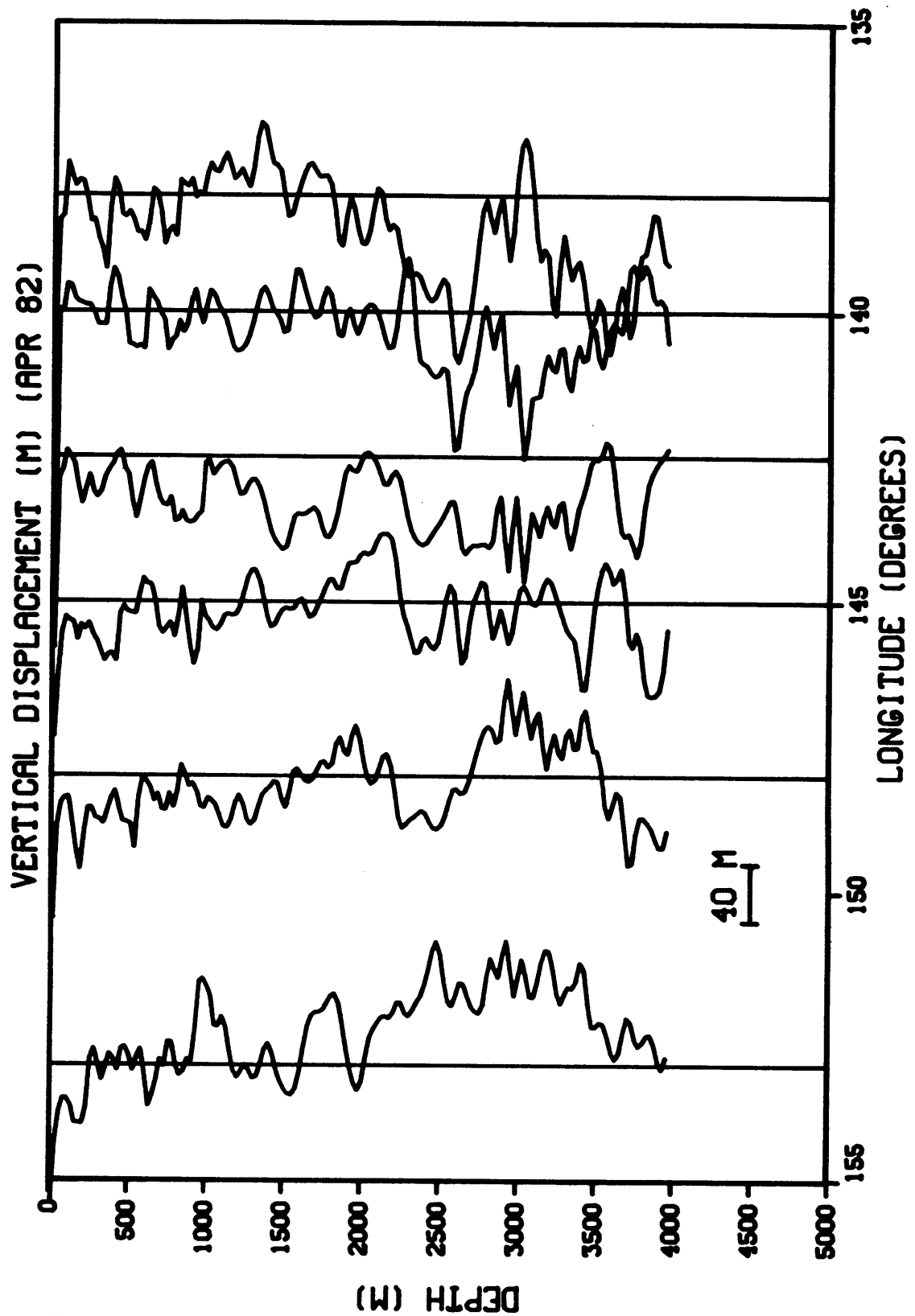
Fig. 2.7. Vertical displacement along a longitudinal section at the equator, taken during the April 1982 cruise. All profiles calculated at each site were averaged together.

$(N(z)/N_0)^{1/2}$ yields solutions which are homogeneous in z. After such transformation, the vertical scales and amplitudes of the motions do not change with depth. Using expressions $(A.2)$, the new scaled variables (denoted by an asterisk) are given by

$$(u^*, v^*) = \left[\frac{N_0}{N(z)}\right]^{1/2} (u, v) \tag{2.7a}$$

$$\varsigma^* = \left[\frac{N(z)}{N_0}\right]^{1/2} \varsigma \tag{2.7b}$$

The condition for the validity of the WKBJ solution to the vertical structure equation is

$$m^{-3/2}\frac{\mathrm{d}^2}{\mathrm{d}z^2}(m^{-1/2}) \ll 1 \tag{2.8}$$

where $m = N(z)/c$ is the local wavenumber (e.g., Gill, 1982). If we take m^{-1} as the vertical scale of the wave, then condition (2.8) simply states that the wave scale has to be much shorter than the scale over which the wave changes, which is the scale of variation of $N(z)$ in our case. This condition is clearly violated at thermocline depths, for relevant vertical wavelengths. Therefore the top few hundred meters of the records are generally not included in the spectral analysis. Before proceeding, we have to choose a value for N_0. In principle, this choice is arbitrary. A unique N_0 was used in order to make possible the comparison between spectral results from different cruises. From the 3 mean $\bar{N}(z)$ profiles shown in Fig. 2.6a,b,c we computed 3 average values of N. We then took the average of those 3 values to come up with a value of $N_0 = 0.1887 \times 10^{-2}s^{-1}$. This choice of N_0 gives a rough correspondence between the total depth of the records in the stretched and unstretched vertical coordinates.

With this value of N_0 and previously computed $\bar{N}(z)$ profiles, expression (2.6) was integrated numerically in z, yielding one mapping $z \longrightarrow z^*$ for each of the buoyancy profiles shown in Fig. 2.6. These mappings are given in Fig. 2.8. As expected, depths at which $\bar{N}(z)$ is large (e.g., in the thermocline) show $\Delta z^* > \Delta z$, while the reverse is true in the deeper waters where $\bar{N}(z) < N_0$. This latter effect of the coordinate

27
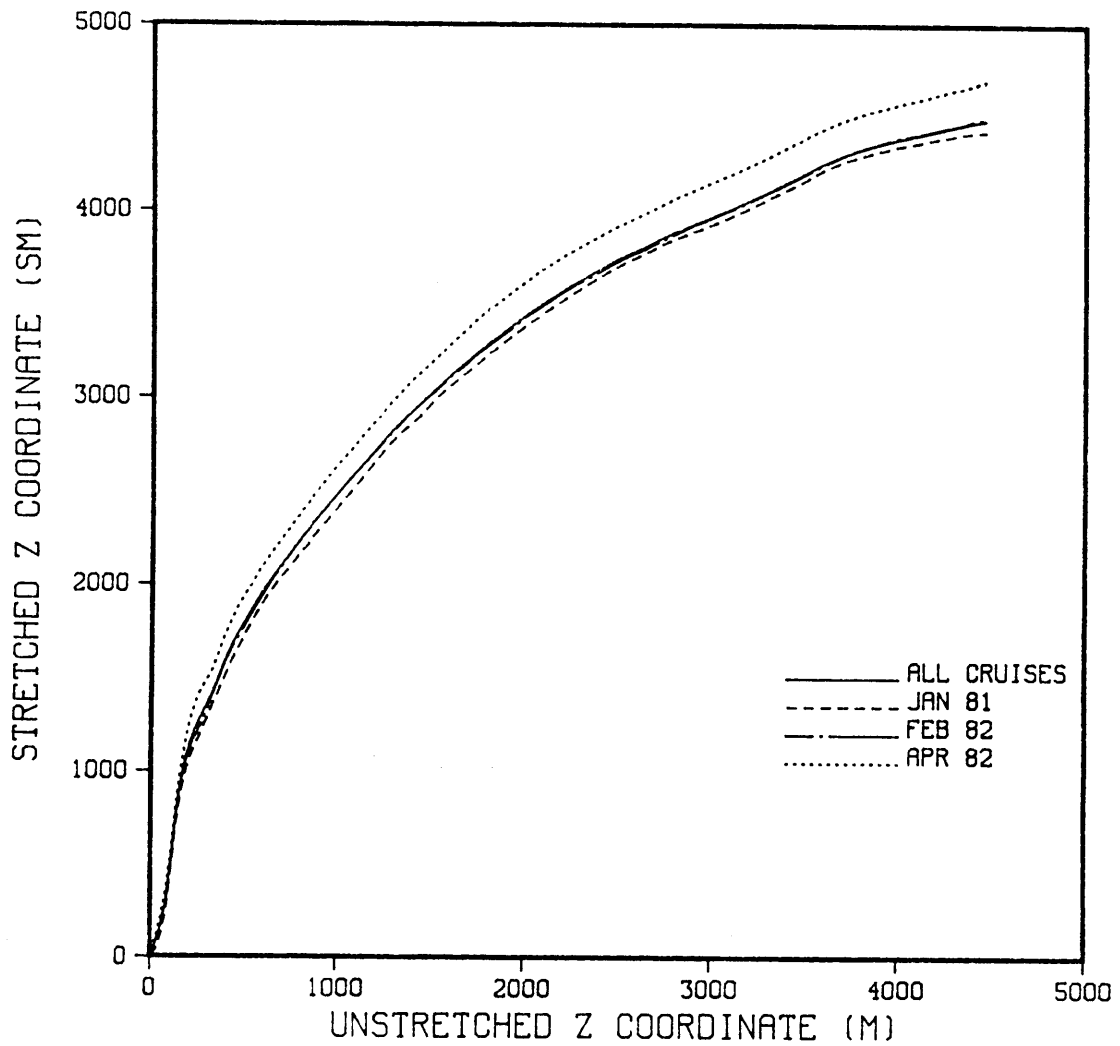
Fig. 2.8. Coordinate mappings $z \longrightarrow z^*$ obtained from the four different $N(z)$ profiles displayed in Fig. 2.6. They are almost indistinguishable, with perhaps the exception of the April 1982 mapping.

transformation creates an enhancement of noise at depth, with 100 m of data being compressed into as little as 20 stretched meters (sm) intervals.

All the vertical displacement and velocity profiles were stretched and scaled, according to (2.6) and (2.7). The use of the stretched coordinate gave records which were not equispaced. Spline interpolation to an equispaced 25 sm grid was performed on the data. Features with wavelengths shorter than twice the largest stretched interval become aliased in the new coordinate system. Results for wavelengths shorter than 80 sm should be taken with suspicion.

Figs. 2.9-2.11 show some S/S records. The strong jets previously seen are still visible in the zonal velocity records. The EUC becomes stretched out over 1000 sm or so, with very large amplitudes. The S/S profiles look more homogeneous in amplitude and vertical scale with depth than the raw profiles of Figs. 2.2-2.5 and 2.7, especially below the EUC. The spectral analysis of this presumably homogeneous data set is pursued next.

2.4 Spectral analysis

Because of the violation of the WKBJ assumption at thermocline depths, before Fourier analysis the records were cut at 1562.5 sm and the top part disregarded. This procedure amounted to neglecting roughly the first 400 m of data, where the strongest gradients in the $\bar{N}(z)$ profiles are observed (Fig. 2.6). The strong Undercurrent is not considered in the analysis. All records were cut to a standard length of 2800 sm, determined by the shortest cast available. Different record lengths of 2600 sm and 3000 sm were also tried by excluding bottom 200 sm or adding another 200 sm at the top. This did not change the spectral results in any significant manner. All analyses presented here are based on the 2800 sm length records.

Fourier decomposition was performed in each profile, after subtracting the mean and tapering 10% of the data at both end points with a 1/2 cosine bell. The Fourier
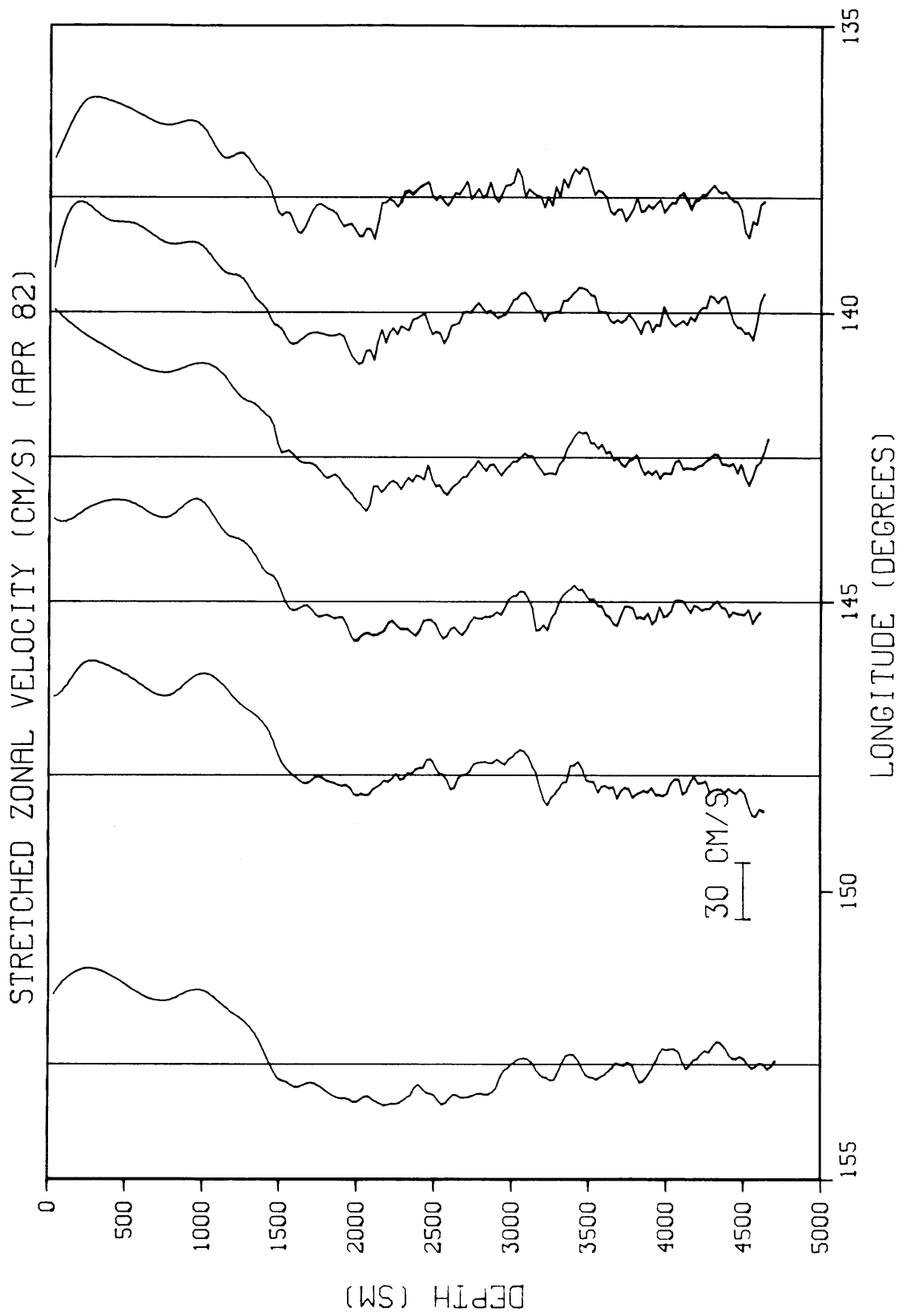
Fig. 2.9. Same velocity profiles of Fig. 2.2 after being stretched and scaled as described in the text.
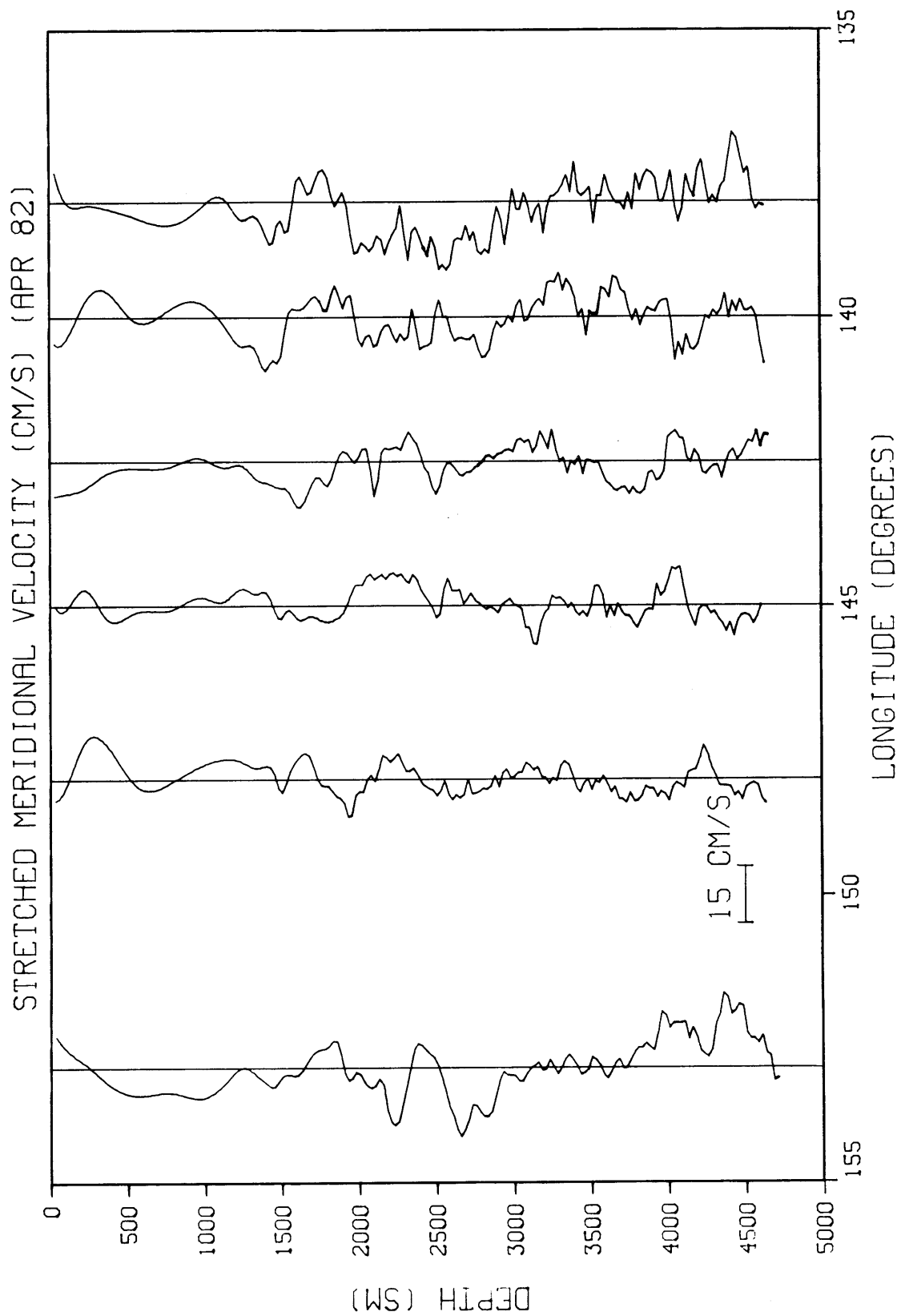
Fig. 2.10. Same velocity profiles of Fig. 2.4 after being stretched and scaled as described in the text.
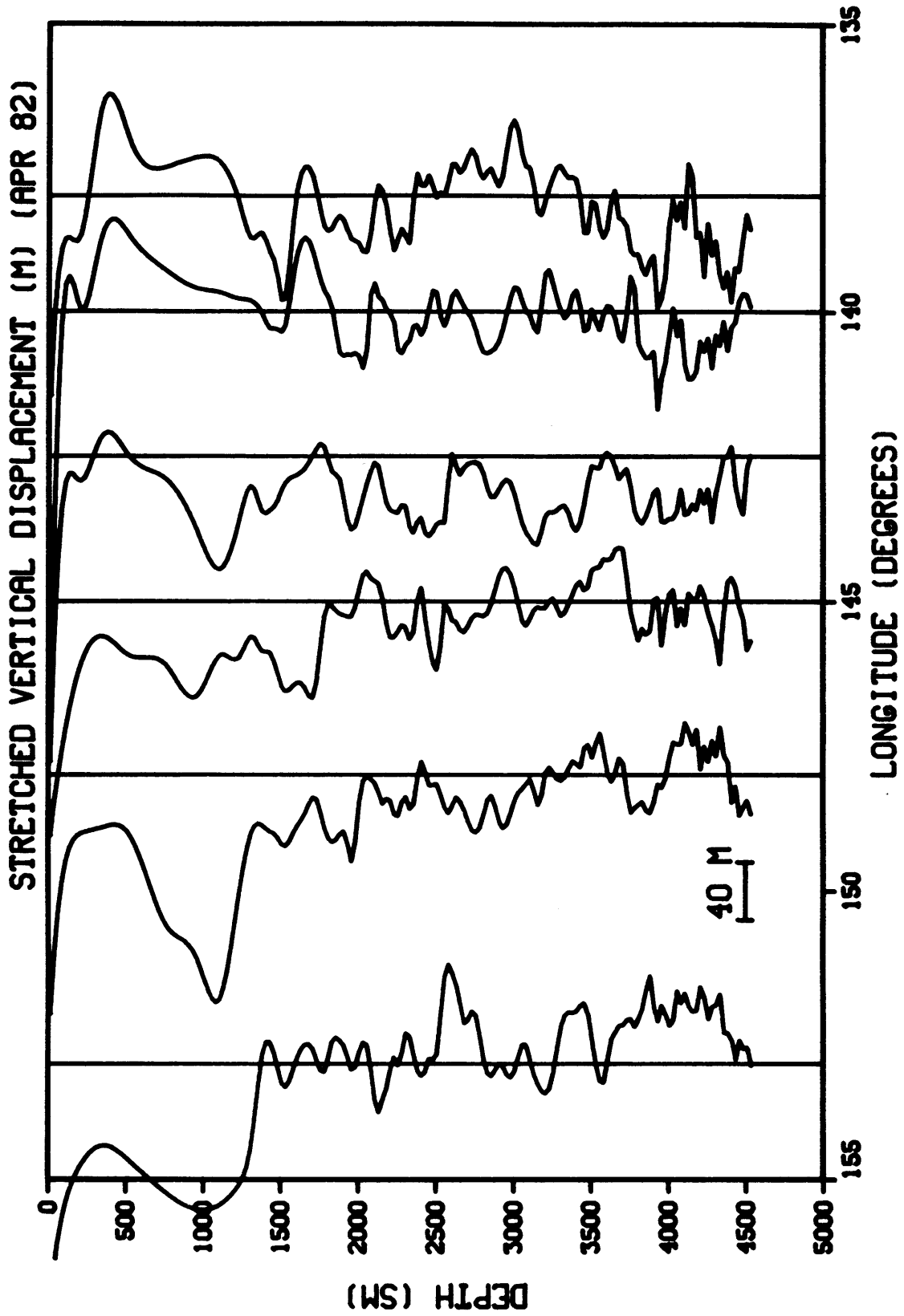
Fig. 2.11. Same vertical displacement profiles of Fig. 2.7 after being stretched and scaled as described in the text.

coefficients were used in power spectra and coherence calculations. In all the spectral computations, we rely heavily on piece-averaging to gain statistical reliability. Because of the long time scales involved, some of our realizations are not rigorously independent. Only robust results are given consideration. Our intention is to have the best possible resolution of the vertical scales present in the data.

To check the validity of the S/S procedure, we cut the records in 2 halves and computed the power density for the top and bottom 1400 sm records separately. The two spectra were generally indistinguishable, except for vertical wavelengths smaller than 80 sm, where the bottom half record showed consistently more power than the top half record. The enhancement of noise introduced by the S/S procedure at depth turned out to be the cause behind this inhomogeneity in the records. The use of a simulated profile composed of a sine wave contaminated by random noise (present throughout the water column) yielded the same discrepancy between top and bottom records, when the S/S procedure was applied to it. Even though an attempt could be made at reducing this effect by applying a filter with a depth varying window to the data (as done by O'Neill (1982)), we chose not to do any filtering, since the effect occurs at wavelengths which are not very well sampled by the White Horse profiler anyway. Furthermore, these vertical scales are aliased in the stretched coordinate system, as explained before, and they will not be considered in this work.

Before diving into more specific analysis, calculations of velocity and vertical displacement power spectra should be useful in revealing, in a quantitative way, the general character of the data. The spectra shown in Fig 2.12 were obtained by piece-averaging all casts made on the equator for the 3 cruises. The 95% confidence level error bars were computed according to Koopmans (1974), treating each profile as one independent realization. Some differences between spectra of u, v and ς are clearly seen in Fig. 2.12. The most striking feature of those plots is the strong peaks appearing in the zonal velocity records, roughly centered at wavelengths of 560 sm and 350 sm. The
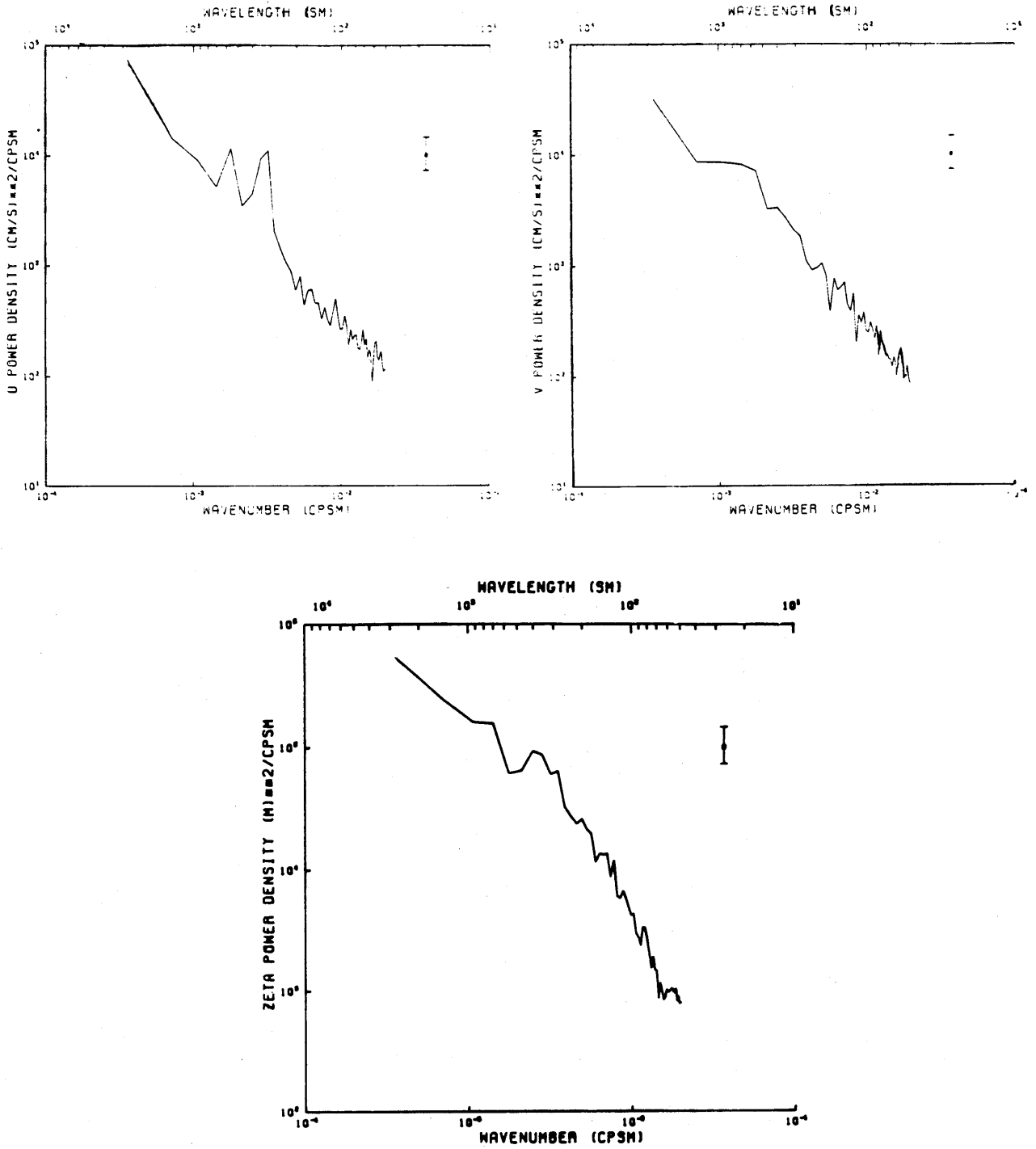
Fig. 2.12. Power spectra of zonal and meridional velocity, and vertical displacement, calculated using all equatorial casts available. Error bars shown were computed at the 95% confidence level.

peak at 560 *sm* was not apparent from a visual inspection of the records, but it is statistically significant in the spectrum. The peak at 350 *sm* rises higher above the background as compared with the other peak. It accounts for roughly 20 % of the total variance in the records, and occurs at vertical scales corresponding to the scales of the conspicuous wiggles present in the u velocity profiles (Figs. 2.2 and 2.9). These have been widely observed before and people have generically called them the equatorial deep jets. Furthermore, analyses in Chapter 3 will show that the amplitude of this peak was also more steady in time than the feature at 560 *sm*. For all these reasons, in the course of this work, we will refer to the peak centered at 350 *sm* as being the EDJ peak. Previous studies (Eriksen, 1981; O'Neill, 1982) were unable to portray the EDJ as a well defined power peak in the zonal velocity spectra, mainly because they had to resort to wavenumber band averaging to gain statistical reliability. The strong signals are absent from either the v or ς records.

These preliminary spectral results set the stage for the more specific analysis pursued in the next two chapters. The signals in the u records are treated separately from what we call the *background* spectra. Their interpretation and modelling constitutes the major effort of this work.

CHAPTER 3
Analysis and Interpretation of Zonal Velocity Signals

We focus our attention in this chapter on the spectral peaks present in the u velocity profiles, concerning ourselves primarily with the determination of the temporal and spatial scales associated with those signals and their possible interpretation in terms of the simple linear wave theory of Appendix A. Although these flows may not be strictly linear given their relatively large amplitudes and apparent long time scales, the linear theory may still provide a good kinematic description of them.

3.1 Power spectra and latitudinal energy scaling

The data set spans roughly 16 months, with each cruise taking place over approximately 1 month. It is therefore necessary to establish the differences and similarities between the records collected so far apart in the time domain, insofar as the signals under consideration here are concerned. Grouping all the data together increases the number of degrees of freedom, hence improving the statistical significance of the results. However, in doing it, we may lose important dissimilarities occurring between data collected on different cruises. Fluctuations in the peak amplitudes from cruise to cruise if found, for example, could be helpful information when trying to interpret the data. Thus, each cruise data set was first treated separately, but only those results which are relevant to this presentation will be documented here.

A look at Fig. 2.3 reveals the general trapped-to-the-equator nature of the high baroclinic mode flows. In particular, the strong variability associated with the jets seems to be gone on profiles taken at C, G, M and O sites located at roughly $1°15'$ from the equator (Fig. 2.1). To confirm this assertion, we calculated the coherence of equatorial with off equatorial u profiles. This was done by averaging casts taken at each site and taking the mean as one realization of u at that site. Profiles at $138°$W and $145°$W were used. Plots of Fig. 3.1 clearly show high coherence at zero phase for
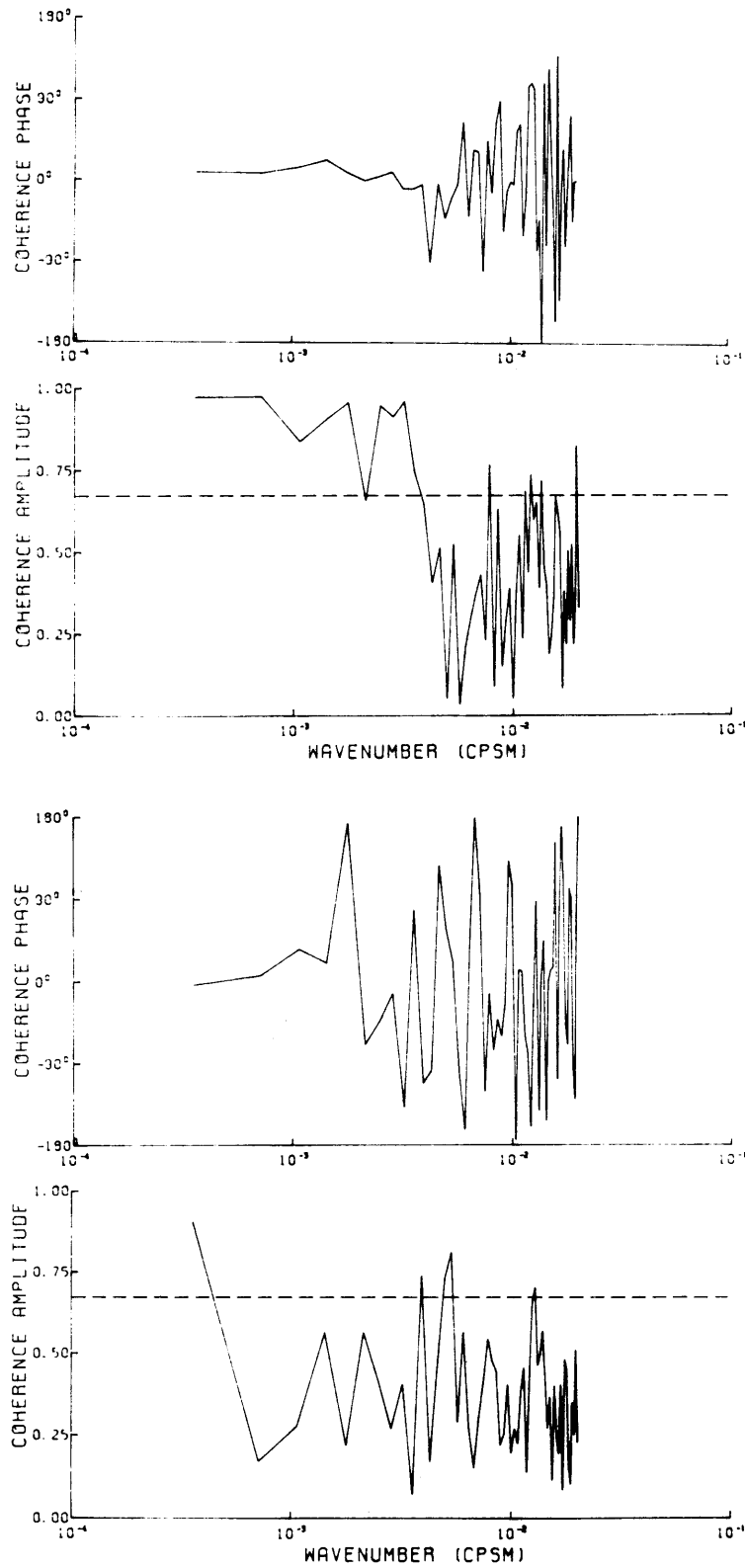
Fig. 3.1. Coherence of zonal velocity u at the equator with u at $0°31'$N (top) and u at $1°16'$N (bottom) using data from all three cruises. A dashed line is drawn at the 95% zero significance level.

the $u(0°)/u(1/2°)$ pair, at the wavenumbers of interest. Coherence amplitudes drop below the 95% zero significance level for the pair $u(0°)/u(1°15')$. The latitudinal scales implied by these calculations are on the order of 100 km.

Linear equatorial wave theory yields a simple relation between the meridional trapping scales and the vertical scales of the waves. The shorter vertical wavelengths are more closely trapped to the equator as seen from expression (A.6) in Appendix A. If our signals are to be explained by this theory, they should satisfy the latitudinal decay scale predicted from the theory itself. In particular, if the strong zonal flows are Kelvin waves, their meridional structure should follow the simple exponential function $\exp -\{\beta y^2/2c\}$, with β and c as defined in Appendix A. The zonal kinetic energy (the power density) should go as the square of the exponential.

To test such an hypothesis, first we need to consider the partition of the flow into equatorially symmetric and anti-symmetric parts. Only the power associated with the symmetric flows should be expected to scale as the exponential, and only if Kelvin waves dominate. All the other waves will have more complicated meridional structures as given by the Hermite functions (A.6), regardless of whether these functions are symmetric or anti-symmetric about the equator.

Only symmetric flows contribute to the power computed from equatorial casts. To obtain symmetric power for other latitudes, we add velocity records from both sides of the equator (e.g., D and F casts or L and N casts). These sites were not at exactly the same and opposite latitude, nor were the different casts collected simultaneously, but for time scales long compared to 1 week, the procedure seems reasonable. At 138°W, there was only one cast per site per cruise. Therefore, only one realization of the symmetric velocity fields per cruise was possible. The situation at 145°W was different and slightly more ambiguous. In general more than one realization per cruise was available and also more than one combination was possible. If, for example, we wanted to compute the symmetric power at a latitude of 1/2° using L and N casts taken during the April

38

cruise (L08, L09, N06 and N07 from Table 2.1), there were four different realizations of the symmetric u field, but only two of them were independent, giving us two possible combinations when computing the spectrum. Generally, every possible realization was taken in the average, even though only the independent pairs were counted in the degrees of freedom. Dependent and independent pieces were weighed properly in the averaging.

Equatorial zonal velocity spectra computed for each cruise separately are given in Fig. 3.2. We should be aware of the changes occurring between the January 1981 and February 1982 cruises, and pertaining to the relative amplitudes of the 560 *sm* and the 350-311 *sm* peaks. Contrasting with the relatively small changes in amplitude for the latter, the power at the 560 *sm* wavelength increased by a factor of two or three during that period, a fact bearing some importance when we later try to interpret our findings.

To shorten this presentation, plots of symmetric and anti-symmetric power spectra for off-equatorial sites are not presented here. In brief, symmetric power spectra at $0°31'$ show the same peaks as at the equator, even though some wavenumber shifting occurs, suggestive of the finite bandwidth nature of these phenomena. The anti-symmetric power spectra have no special structure and contain in general less variance than their counterparts. At $1°16'$, nothing really striking happens in either spectra.

Important results of the calculations just described are summarized in Table 3.1, which provides the comparison between the energy meridional decay scales as computed from the data, and the predicted Kelvin wave exponential decay scales as given by theoretical considerations. Agreement is reasonably good, considering the size of the error bars on the spectral estimates. Results based on data from all 3 cruises are more reliable, yielding a good comparison for the 560, 350 and 311 *sm* wavelengths. At $1°16'$, power estimates for vertical wavelengths smaller than 400 *sm* are at the noise level, therefore only estimates at $0°31'$ for those wavelengths have some real significance.
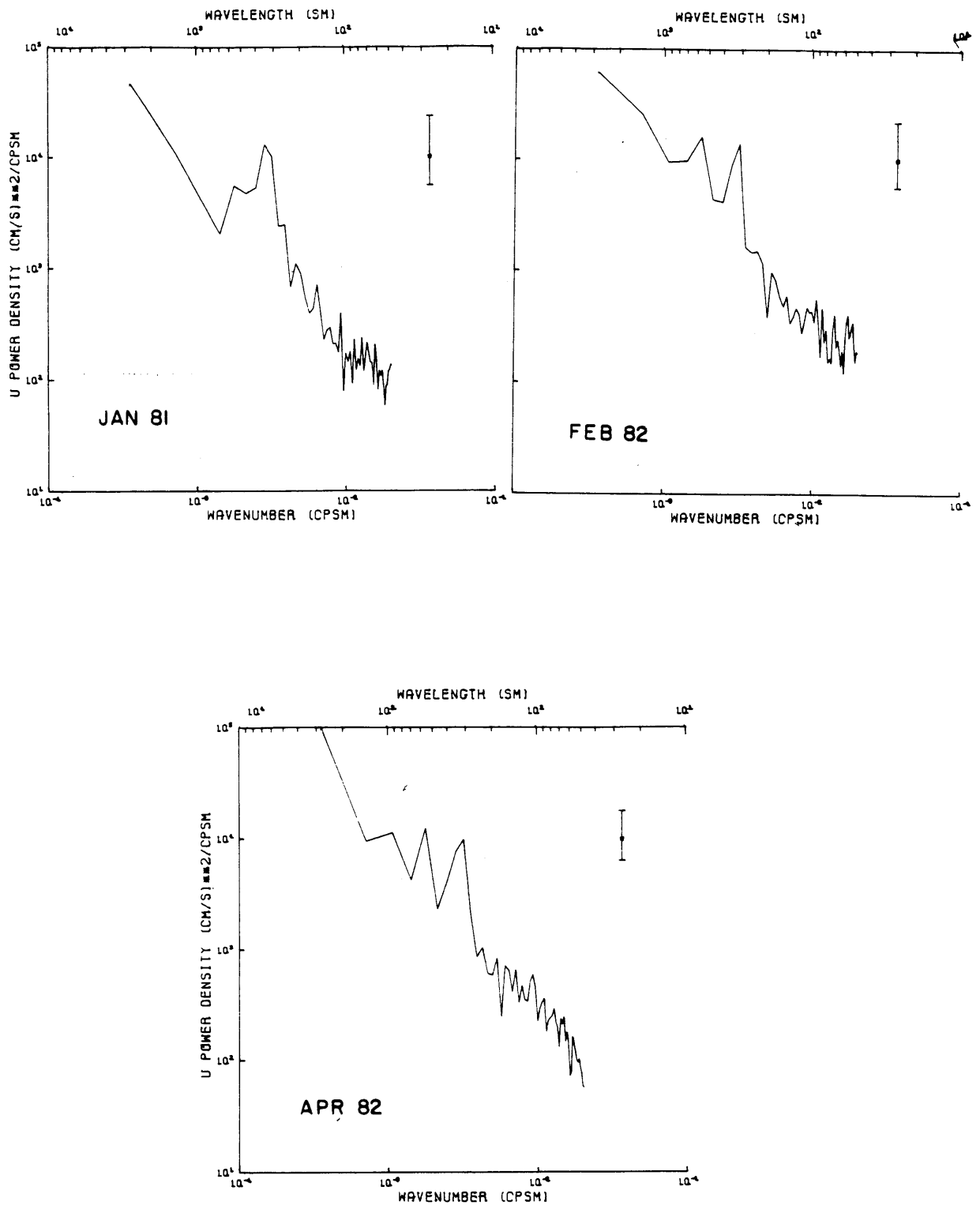
Fig. 3.2. Zonal velocity spectra calculated using only equatorial casts from each cruise.

Table 3.1. Comparison of latitudinal energy scaling for symmetric zonal flows with theoretical scaling based on equatorial Kelvin wave. Here, $\alpha = 2\pi\beta y^2/N_0\vartheta$ with $N_0 = 0.1887 \times 10^{-2}s^{-1}$. Units for values of power density are $cm^2s^{-2}cpsm^{-1}$ (cycles per stretched meter). SYM stands for symmetric power.

a) January 1981

$\vartheta(sm)$	0°	0°31′ SYM	SYM/0°	$e^{-\alpha}$	1°16′ SYM	SYM/0°	$e^{-\alpha}$
700	2027	1755	0.87	0.69	2275	1.12	0.12
560	5504	4060	0.74	0.64	2946	0.54	0.06
467	4698	5223	1.11	0.59	2842	0.60	0.04
400	5288	3737	0.71	0.53	1305	0.25	0.02
350	12864	5698	0.44	0.48	433	0.03	0.01
311	10087	7368	0.73	0.44	445	0.04	0.006

b) February 1982

700	9811	5430	0.55	0.69	1226	0.13	0.12
560	15967	7564	0.47	0.64	1450	0.09	0.06
467	4457	1816	0.41	0.59	1729	0.39	0.04
400	4206	2743	0.65	0.53	2168	0.52	0.02
350	8994	2110	0.23	0.48	490	0.05	0.01
311	13843	8405	0.61	0.44	490	0.04	0.006

c) April 1982

700	4259	1948	0.46	0.69	6611	1.15	0.12
560	12472	10923	0.88	0.64	357	0.03	0.06
467	2325	829	0.36	0.59	2881	1.24	0.04
400	4232	6450	1.52	0.53	721	0.17	0.02
350	7732	3163	0.41	0.48	1746	0.23	0.01
311	9904	3661	0.37	0.44	392	0.04	0.006

d) All 3 cruises

700	5263	2636	0.50	0.69	3508	0.67	0.12
560	11713	7126	0.61	0.64	1414	0.12	0.06
467	3518	3001	0.85	0.59	2439	0.69	0.04
400	4489	4421	0.98	0.53	1409	0.31	0.02
350	9370	4056	0.43	0.48	945	0.10	0.01
311	11058	6363	0.58	0.44	442	0.04	0.006

3.2 Zonal scales and estimate of zonal wavenumbers

The PEQUOD array provided very good longitudinal coverage, extending over roughly 2000 km in the zonal direction. This enabled us to establish zonal decorrelation scales for the signals, as well as to look for any zonal phase tilts from which estimates of zonal wavelengths λ could be extracted.

The strong coherent character of the EDJ was already noticed on the raw u velocity records (Fig. 2.2). To corroborate this finding in a quantitative way, zonally lagged coherences were computed from casts collected at the equator and at near equatorial sites (i.e., D, E, F, I, J, K, L, N, P and Q casts in Table 2.1), where the signals were clearly present. Given the distribution of casts along the equator, several zonal lags were possible. At each zonal lag, usually more than one realization was available, so that generally no band averaging was needed in the coherence calculations. A summary of the zonal lags we used and the various pairs of casts going into the different realizations at each lag is given below:

2.5° lag — E/I, I/J, J/K and K/P

5.25° lag — E/J, I/K, J/P and P/Q

7.25° lag — E/K, D/N, F/L and K/Q

9.75° lag — E/P and J/Q

15° lag — E/Q is the only available pair

Off-equatorial profiles were only used for the 7.25° zonally lagged coherences. The reader might notice that we grouped together pairs which do not have exactly the same zonal lags (e.g., 2° of longitude separate E and I casts, while K and P are separated by 3°, even though both pairs are taken together in the 2.5° lag calculations). Such procedure is justified for flows with long zonal scales, compared with the lags under consideration. This seems to be the case with both the EDJ and the 560 sm signal.

The lag actually assigned to each calculation is the average of the lags from each pair of casts used.

Zonally lagged coherences were computed both treating each cruise as a separate data set, and using all data from the 3 cruises together. Results are summarized in Table 3.2. The individual cruise results suffer from the small number of realizations available at each lag. The 95% zero significance levels are generally high. However, we still find significantly high coherence amplitudes at the EDJ wavenumber bands (350–311 sm), for lags as large as 7.25°, in all 3 cruises. The same is not true at 560 sm, where data from the first 2 cruises suggested very short zonal decorrelation scales, while coherence jumped dramatically during the last cruise (560 sm was coherent for at least 1100 km in April 1982).

The three cruise results confirm the zonal coherent character of the EDJ, especially seen in the 350 sm band, where records 1200 km apart are still significantly correlated. If more realizations at the 15° lag were available, we would probably find the EDJ to be zonally coherent over the whole PEQUOD array. This result contrasts with the findings of Eriksen (1981). His data was collected further to the west, near the Gilbert islands. He found zonal decorrelation scales for the deep jets shorter than 500 km, but the vertical wavenumber band averaging used in the coherence calculations and the proximity of the Gilbert island chain to the site of the measurements may have influenced his results.

Interpretation of the phases in Table 3.2 lead to rough estimates of the zonal wavelengths possibly associated with the signals. While in the EDJ band, we have mostly negative phases, meaning lines of constant phase slope down towards the east, the opposite seems to be true at 560 sm, with positive phases implying a zonal tilt in the other direction. Fig. 3.3 plots phase as a function of zonal lag for the 350 sm wavelength, using the grand average 3 cruise results. Also plotted is the data for the 560 sm wavelength using the April 1982 values. Error bars drawn were computed as

43

Table 3.2. Zonally lagged coherences computed both for each cruise separately and for the 3 cruises together. Positive (negative) phase means eastern casts lead (lag) western casts with depth. No wavenumber averaging was done. Boldface numbers indicate coherence amplitudes bigger than the 95% zero significance values. Symbols ρ and θ denote coherence amplitude and phase respectively.

a) January 1981

LAGS $\vartheta(sm)$	2.5° ρ	θ	5.25° ρ	θ	7.25° ρ	θ	9.75° ρ	θ
700	0.50	159	0.43	-53	0.42	104		
560	**0.84**	-2	0.79	-31	0.75	-53		
467	0.62	-7	0.66	-39	**0.94**	-36		
400	0.69	-12	0.78	-32	0.69	-33		
350	**0.88**	-6	0.79	-10	**0.89**	-15		
311	**0.86**	-10	0.81	-1	**0.95**	3		
280	0.69	1	0.35	62	0.76	53		

b) February 1982

	2.5° ρ	θ	5.25° ρ	θ	7.25° ρ	θ	9.75° ρ	θ
700	0.77	9	0.59	3	0.43	20	0.90	41
560	0.56	26	0.34	22	0.48	41	0.77	124
467	0.43	-38	0.29	-30	0.16	-36	0.83	16
400	0.77	10	0.48	-12	0.72	-31	0.89	-10
350	**0.88**	-4	**0.86**	-15	**0.87**	-11	0.97	-21
311	**0.95**	19	0.74	1	0.69	29	0.59	9
280	0.38	11	0.67	9	0.28	76	0.80	-24

c) April 1982

	2.5° ρ	θ	5.25° ρ	θ	7.25° ρ	θ	9.75° ρ	θ
700	0.78	3	0.68	25	0.71	22	0.51	67
560	**0.98**	7	**0.97**	15	**0.86**	27	**0.99**	31
467	0.53	-30	0.28	88	0.23	30	0.92	-53
400	**0.80**	2	0.75	-40	**0.91**	-40	0.65	-32
350	**0.82**	2	**0.87**	-26	**0.91**	-14	0.83	-48
311	**0.94**	4	**0.88**	-9	**0.83**	-1	0.81	-30
280	**0.90**	31	**0.83**	63	0.59	75	0.92	115

Table 3.2d. Zonally lagged coherences computed for the 3 cruises together (continuation of table from previous page).

d) All 3 cruises

LAGS $\vartheta(sm)$	2.5° ρ	θ	5.25° ρ	θ	7.25° ρ	θ	9.75° ρ	θ	15° ρ	θ
700	0.58	11	0.56	7	0.43	28	0.18	-130	0.70	-107
560	0.76	11	0.68	11	0.61	20	0.54	41	0.72	59
467	0.50	-23	0.30	-26	0.47	-31	0.65	-15	0.94	41
400	0.76	1	0.65	-32	0.78	-37	0.62	-24	0.32	-126
350	0.86	-4	0.82	-15	0.88	-13	0.91	-29	0.93	-24
311	0.89	5	0.79	-2	0.76	14	0.66	-12	0.94	20
280	0.63	18	0.55	41	0.59	64	0.50	62	0.85	-163

described in Koopmans (1974). An estimation of the zonal wavelengths underlying the records was carried out by simply performing a linear regression on those plots. The particular choice of results to be used in the fit was based on the clear linear character of the phase *vs.* zonal lag plots, most evident in them.

Table 3.3 displays our findings. The λ_{min} estimates are computed from the line with greatest possible slope still contained within the phase error brackets. The large uncertainty in the values of λ is clear. Zonal phase tilts can even be reversed for the 560 *sm* vertical wavelength (but not for 350 *sm*). Nevertheless, the goodness of the linear fits reassures us of the basic correcteness of the zonal phase tilts inferred from the coherence phases.
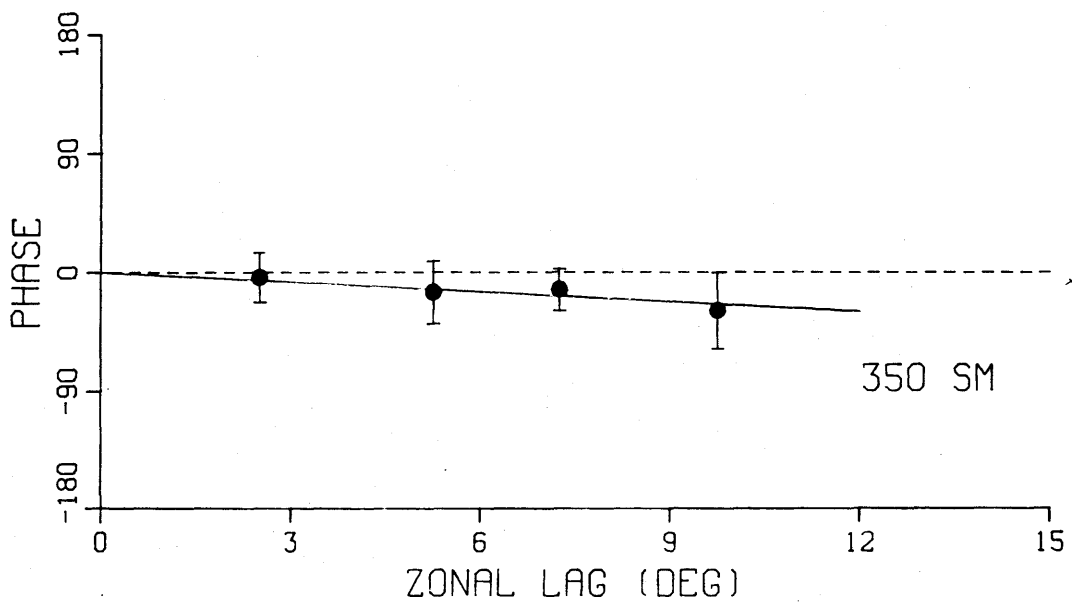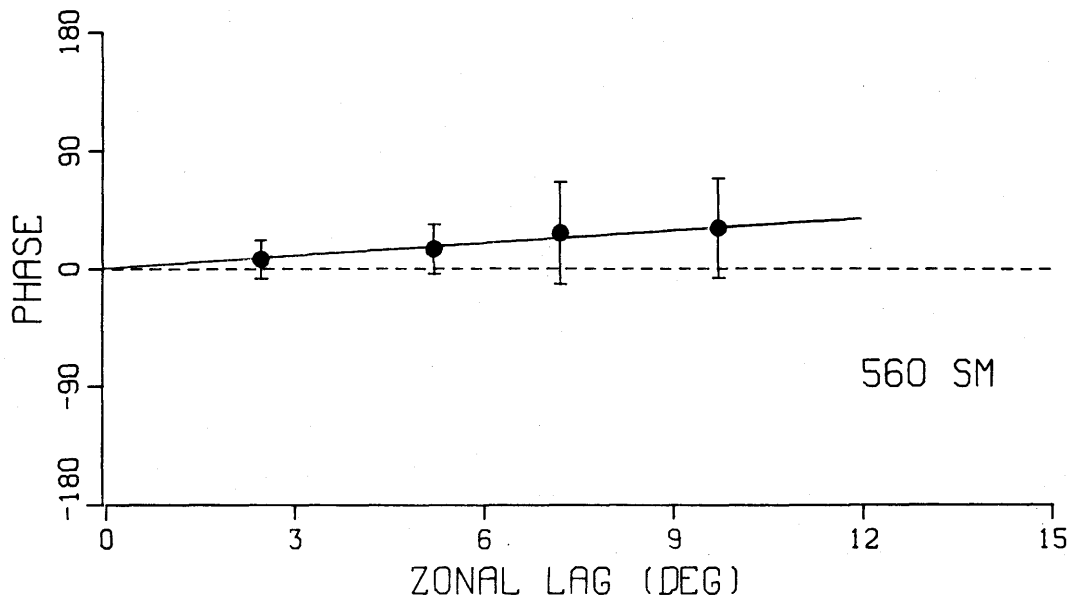
Fig. 3.3. Plots of coherence phase *vs.* zonal lag for 560 *sm* (April 1982 result) and 350 *sm* (3 cruise result). 95% phase error bars are drawn at each point. Straight lines come from a least squares fit to the data.

Table 3.3. Estimates of zonal wavelength λ in kilometers from the zonally lagged calculations, using data plotted in Fig. 3.3. λ_{min} is obtained from lines with greatest possible slope still contained within the phase error bars of Fig. 3.3.

$\vartheta(sm)$	λ	λ_{min}
560	12400	6200
350	15800	10100

3.3 Time scales and vertical propagation

Questions about the characteristic time scales of the EDJ have been unanswered since they were first observed by Luyten and Swallow (1976), mainly because of lack of adequate time coverage in the data sets available prior to the PEQUOD program. Establishing whether or not the deep jets propagate vertically remains crucial to their possible interpretation in terms of equatorially trapped waves, as advanced by some studies (Eriksen, 1981).

Our data set is not, by any means, a time series. Instead, essentially only 3 points in the time domain are provided, if we considered the apparent long scales of the jets. The other two experiments put together as part of the PEQUOD program were much better suited for analysis in the frequency domain [see Eriksen (1985), Firing (1987)]. A qualitative examination of the zonal velocity records revealed, much to our surprise, the apparent stationary character of the alternating deep jets flows. We could not trace any systematic upward or downward motion of the stacked jets, from one cruise to the other, but perhaps we should not expect naturally occurring flows to behave as if a single wavelength was responsible for them. In fact, the velocity spectral peaks are embedded in a broad band energetic background, and only represent a fraction of the total variance in the records. To quantify the statements about the presence or absence

of vertical propagation in the records (at the wavenumbers of interest), we decided to compute time-lagged coherences from the data, and look at resulting phases.

Coherences done between casts from same cruise usually show no phase propagation, for the particular wavenumber bands considered here. We made use of this fact in computing time-lagged coherences between cruises. Basically, all casts collected at one site during the same cruise were averaged. Then, each of the equatorial and near equatorial $(0°31')$ sites provided one realization of the coherence. Piece averaging was again used to insure proper wavenumber resolution. Only three time lags were available, namely at roughly 2, 13 and 15 months, corresponding to coherences done between casts collected during February and April 1982, January 1981 and February 1982, and January 1981 and April 1982, respectively.

When applying the S/S scheme, described in Chapter 2, to the velocity data, we cut all records at 1562.5 sm. This stretched depth corresponded to different depths in the unstretched coordinate, since we used a different $\bar{N}(z)$ profile for each cruise. We had to be careful in order not to introduce any artificial phase propagation merely by having the origin of records from different cruises lie at different real depths. Two approaches were tried to eliminate this problem. Simply cutting the records at different stretched depths to make all the records start at the same real depth was one possible way out. A slightly less awkward procedure involved using a unique $\bar{N}(z)$ profile to stretch and scale all the records. The buoyancy frequency profile employed was shown in Fig 2.6d. Both schemes yielded the same coherence results, within the 95% confidence limits. We shall refer here to results given by the second approach.

Time-lagged coherence plots are presented in Fig. 3.4. Several bands show significant non-zero coherences, but we will concentrate our attention here on the particular wavenumber bands associated with the strong zonal velocity signals, deferring treatment of the others until Chapter 4. Fig. 3.5 is most illuminating in presenting some of

48
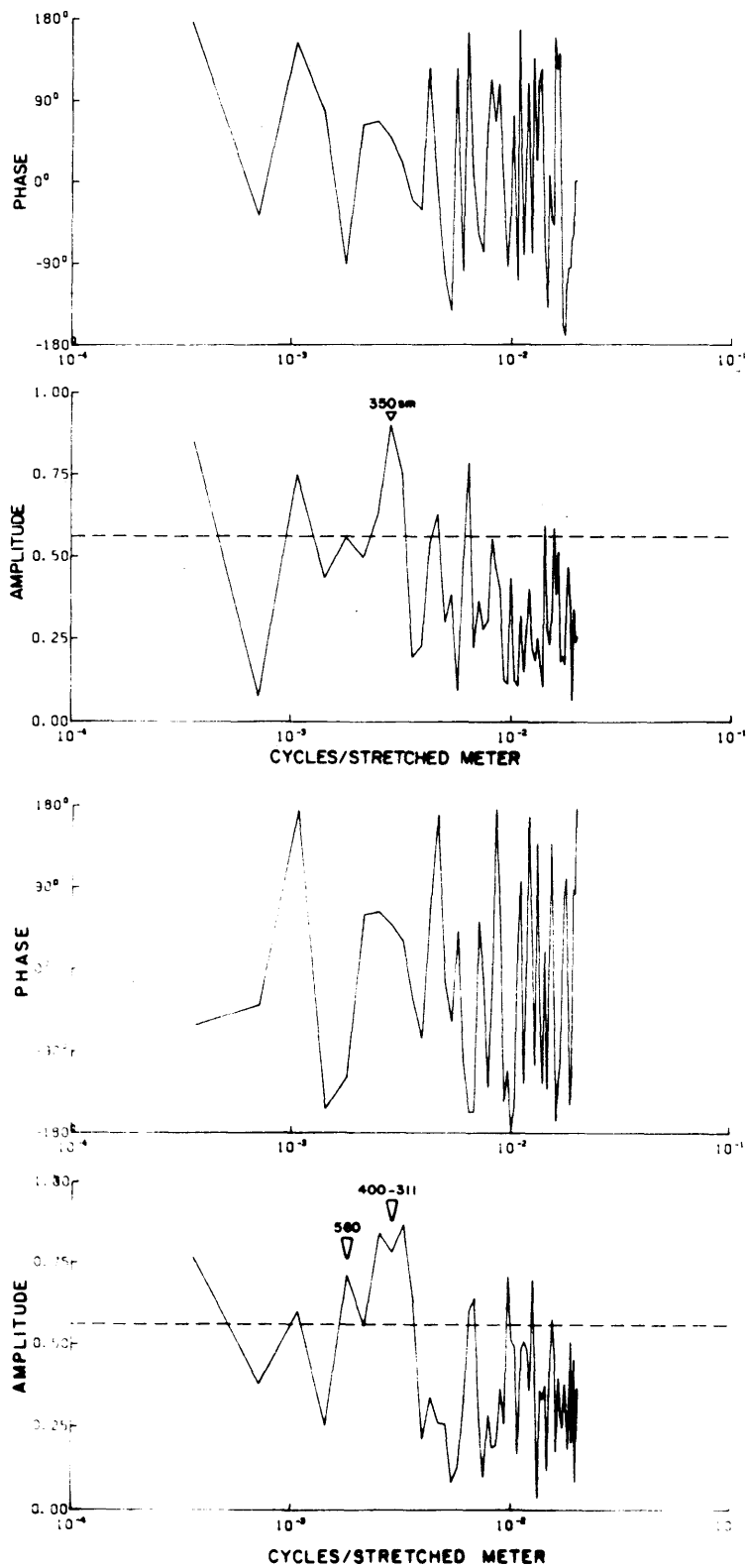
Fig. 3.4. Plots of time-lagged coherence amplitude and phase for 13 month (top panel) and 15 month (bottom panel) lags. Positive (negative) phase means earlier casts lead (lag) later casts with depth.
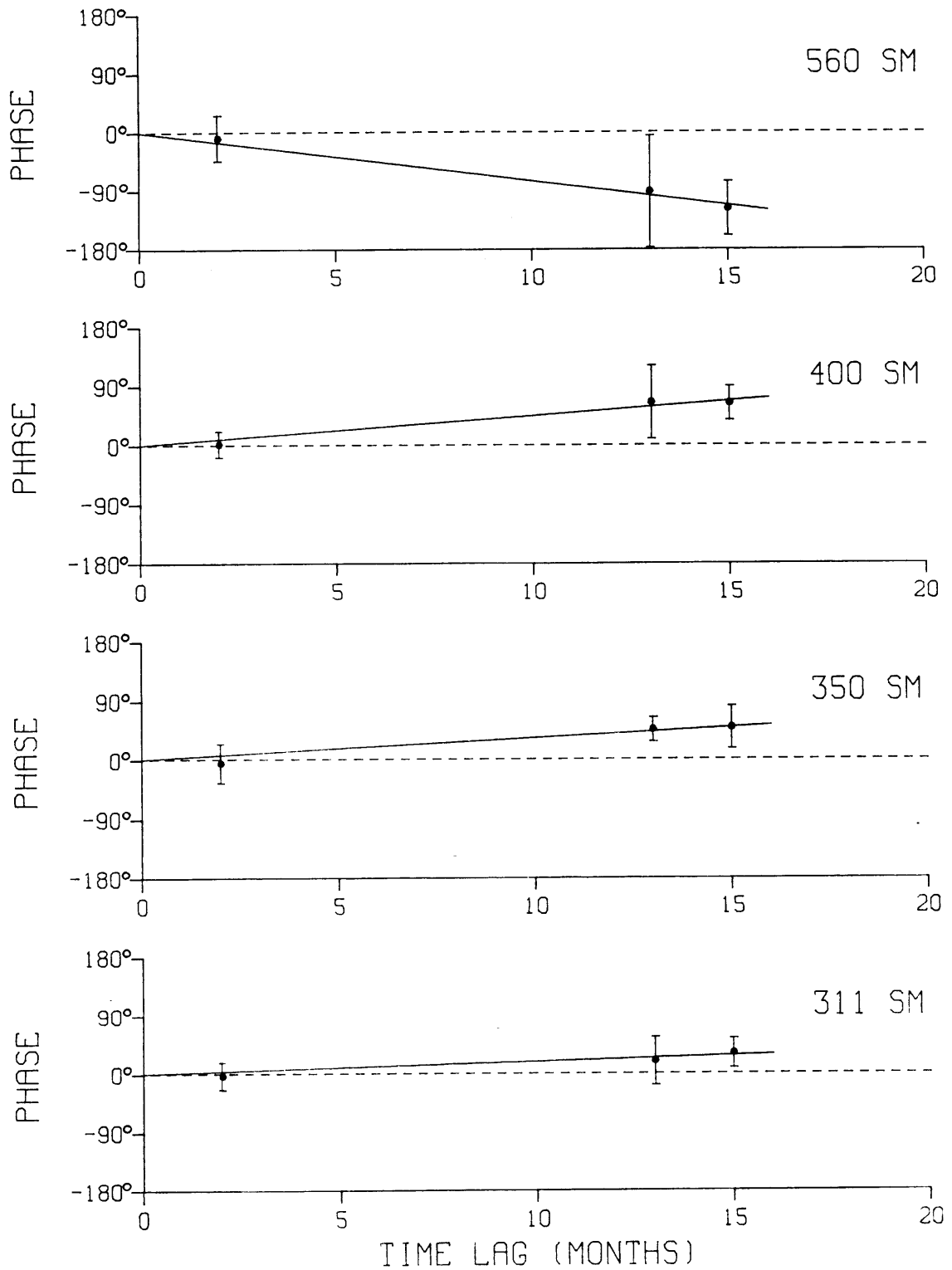
Fig. 3.5. Plots of coherence phase *vs.* time lag for 560 *sm*, 400 *sm*, 350 *sm* and 311 *sm*. 95% phase error bars are drawn at each point. Straight lines are the best linear fit to the data.

our findings. In the most simple interpretation, positive (negative) phase implies downward (upward) propagation of phase in the records. Most striking is the occurrence of apparent downward propagation over the 400–311 *sm* band, and the clear upward propagation of the 560 *sm* signal. Even though the error bars on some of the phase estimates are not small, they do not embrace the zero phase line in general. There is even a slight linear trend in the phase *vs.* time lag plots of Fig. 3.5, especially for the 560 *sm* case. Unfortunately, 3 data points are too few to make any strong statements about this apparent trend. If real, this linear relation between phase and time lag is a clear hint at the possible presence of simple wave motions in the records. An attempt at establishing bounds on the wave periods suggested by the time-lagged coherence phases is deferred until later in this chapter. It suffices to emphasize here the extremely long time scales (on the order of a few years) implied by results of Fig. 3.5.

3.4 Interpreting the 560 sm signal

It is our purpose here to seek the most simple explanation of what we have learned from the spectral analysis of the previous 3 sections. In the easiest conceptual picture, deep equatorial flows are thought to be the manifestation of equatorial trapped waves which propagate their energy from the actively forced upper layers of the ocean, down towards the ocean floor. We will invoke linear equatorial wave theory to interpret the nature and behavior of the 560 *sm* signal seen in the records. Our approach is to see if the spatial and temporal scales, inferred from spectral and coherence calculations for the 560 *sm* band, can be related to a point in the general equatorial wave dispersion curve, given as expression $(A.7)$ of Appendix A. A slightly more complicated scheme consists in having, instead of one single wave mode, a sum of several modes whose superposition reproduces the relevant aspects of the data.

3.4.1 Single wave mode interpretation

The time-lagged coherences of section 3.3 gave substantial weight to the hypothesis of a single frequency being responsible for the vertical propagation observed at 560 *sm*. A linear relation between the phase and time lag, as suggested in the plot of Fig. 3.5, strongly hints at a phenomenon with a simple spectral structure in the frequency domain. If in turn several different time scales were involved, we would expect a more complex relation of coherence phase with time lag. It is clear that, with such small number of data points (only three in fact), we can not make a strong argument in favor of the linear character apparently displayed by the data of Fig. 3.5. However, we do not have any stronger reasons to believe the contrary is true.

Having said this, the obvious thing to do is to estimate a period from fitting a straight line through the phase points in Fig. 3.5. The regression yields a most probable period T equal to four years. Bounds on this estimate may be calculated by drawing lines with greatest and smallest slope possible, given the error bars for each phase data point. This method gave the range

$$2.8 \text{ years} < T < 6 \text{ years} \tag{3.1}$$

for possible values of the period T. The long time scale of the signal is very pronounced in our findings, given the large estimates for T_{min} in (3.1). Forcing mechanisms for these waves and some of the more subtle consequences of their very long periods will be discussed later, but they are certainly a fair possibility in the tropics.

For equatorial waves, upward phase propagation generally implies downward energy propagation and vice-versa. In the case of the 560 *sm* signal, energy is traveling downward, as implied by the time lagged coherence phases. This finding seems reasonable. Atmospheric forcing at the surface injects energy into the ocean. Under general conditions , this energy then propagates away from the forcing region. Assuming that dissipation is strong enough to prevent any significant amount of energy from reaching

52

and reflecting from the ocean bottom, and if no other deep wave energy source is at work (e.g., wave generation could occur if we had strong flows over rough topography), it is plausible to find a downward energy flux.

The sign of phase propagation has another important implication, when coupled together with the zonal phase tilt found in section 3.2 for the 560 *sm* band. With lines of constant phase sloping down towards the west, an upward phase velocity signifies the presence of westward phase propagation in the records, since lines of constant phase are perpendicular to the phase velocity vector. This places a powerful restriction on the types of waves which can be held responsible for the observational results. Kelvin waves have eastward zonal phase speeds (i.e., $c_x > 0$) and can be quickly excluded. The long periods of the flow make it highly unlikely for gravity waves to play any major role. In addition, since mixed Rossby-gravity waves have no zonal flows at the equator, as implied by expression (A.8) in Appendix A, we are left with long Rossby waves as the only possible candidates to explain the data.

The dispersion relation for long Rossby waves takes the simple form

$$\sigma = -\frac{s}{2j+1} \qquad j = 1, 2, 3, \ldots \ldots \tag{3.2}$$

in the nondimensional units defined in Appendix A (expression (A.4)). In terms of dimensional period $T = 2\pi/\omega$, zonal wavelength λ, and vertical wavelength ϑ, we have

$$T = 2\pi \left(\frac{2j+1}{N_0} \right) \frac{\lambda}{\vartheta} \tag{3.3}$$

where we have dropped the minus sign. If the signal is to be interpreted in terms of a long Rossby wave, its time and space scales should be consistent with relation (3.3). Putting it in a slightly different way, the range of periods defined from the time-lagged coherence calculations and given in (3.1), should overlap with the range of periods computed with the help of dispersion relation (3.3) from the estimates of λ, given in Table 3.3. These latter estimates are presented in Table 3.4, for several values

53

Table 3.4. Estimates of T and T_{min}, calculated from using the estimates of λ provided in Table 3.3 for $\vartheta = 560$ sm together with dispersion relation (3.3), for first odd 3 meridional Rossby modes. Periods are given in years.

	$j = 1$	$j = 3$	$j = 5$
T	7	11.7	16
T_{min}	3.5	5.8	8

of j. Only odd meridional modes (i.e., $j = 1, 3, 5, ...$) are relevant here. Even Rossby wave modes have a node in zonal velocity at the equator, and only contribute to the meridional velocity records there (see Rossby wave functions $(A.8)$ in Appendix A).

The values of T_{min} in Table 3.4 do indeed fall within the range of values obtained from the time-lagged coherences for the first meridional mode (just barely for the third mode). In principle, only the $j = 1$ and $j = 3$ modes could be responsible for the 560 sm feature, from what we have said up to now. To corroborate this evidence, we use what we know about the latitudinal structure of the flow.

Rossby waves have a more complex structure in latitude than the simple exponential function which is characteristic of Kelvin waves. The Hermite functions describing their y dependence exhibit an oscillatory character up to a certain turning latitude and decay afterwards. The zonal velocity wave functions $(A.8b)$ for a period of four years and a vertical wavelength of 560 sm are plotted in Fig. 3.6, for the first few odd meridional modes. The latitudes of PEQUOD sites are also marked in the figure. The first mode has a node beyond near-equatorial sites D, F, L and N, but for $j = 3$ and $j = 5$, the node occurs between the equator and those sites. If we were observing any of these two latter modes, we would expect a phase reversal of 180° between records taken at the equator and at sites 1/2° off the equator. This was not seen in the data, as Fig. 3.1 illustrates. Therefore, it is reasonable to conclude that we are most likely in the presence of a long first meridional Rossby wave mode. We did not consider modes any
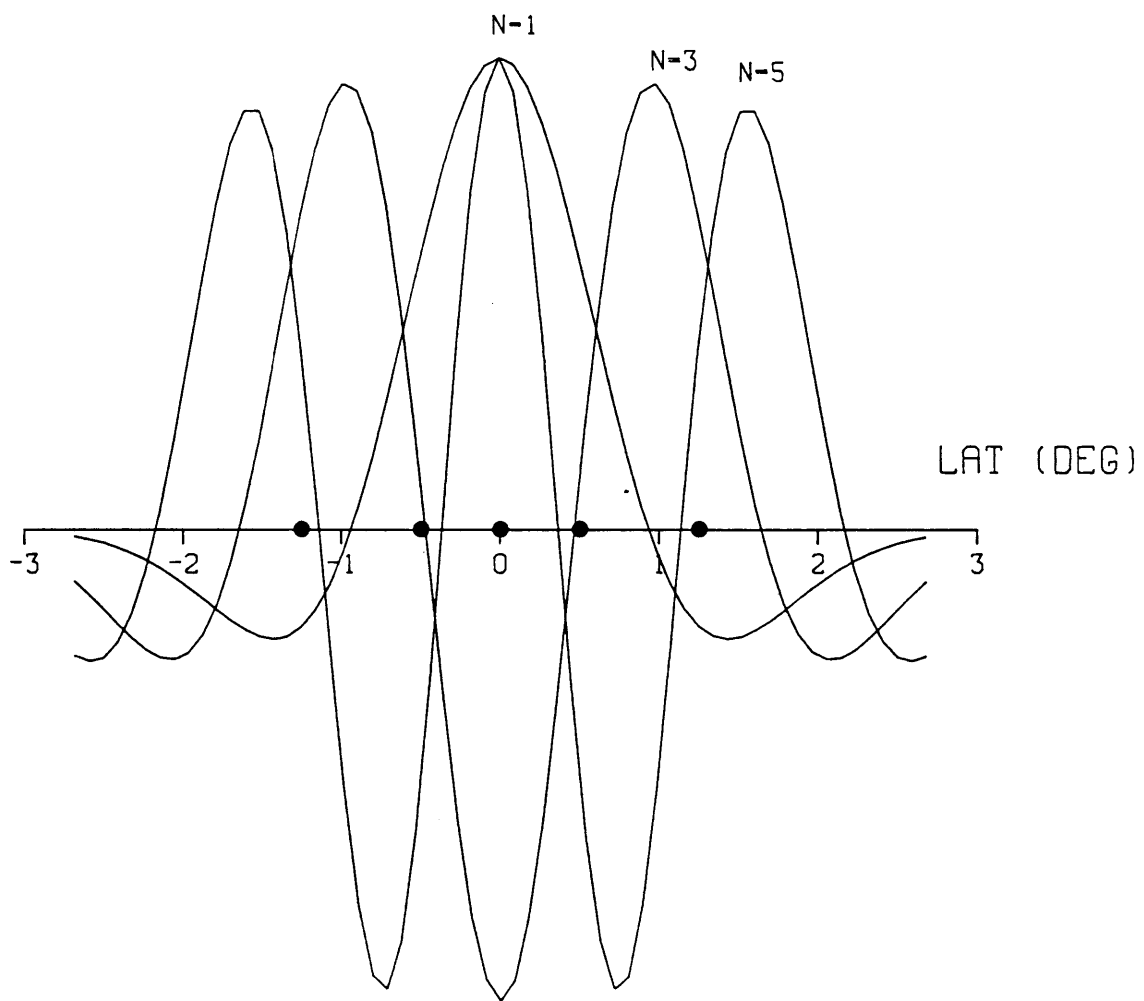
Fig. 3.6. Plots of the $j = 1$, $j = 3$ and $j = 5$ meridional functions for waves of a period $T = 4$ years and vertical wavelength $\vartheta = 560$ sm. Amplitudes at equator are normalized to 1. Black dots are latitudes of PEQUOD sites.

higher than $j = 5$, since from the dispersion relation (3.3), these would imply values of T_{min} in Table 3.4 not in agreement with ranges expressed in (3.1).

A final check of the Rossby wave hypothesis is provided by comparing the latitudinal energy scaling of the data with the theoretical predictions for the particular case of the $j = 1$ Rossby mode. Expression $(A.8b)$ in Appendix A for the meridional structure of zonal velocity field can be rewritten as

$$U_j(\eta) = \frac{sV_j'(\eta) - \sigma\eta V_j(\eta)}{\sigma^2 - s^2} \tag{3.4}$$

where the prime denotes differentiation with respect to η. Using the recursion relation for Hermite polynomials

$$H_j' = 2jH_{j-1} \tag{3.5}$$

and expression $(A.8a)$ for V_j, we obtain

$$U_j(\eta) = \frac{e^{-\eta^2/2}}{\sigma^2 - s^2}(2sjH_{j-1} - s\eta H_j - \sigma\eta H_j) \tag{3.6}$$

With the help of relations

$$H_0 = 1, \qquad H_1 = 2\eta \tag{3.7}$$

for the case $j = 1$, expression (3.6) reduces to

$$U_1(\eta) = \frac{e^{-\eta^2/2}}{\sigma^2 - s^2}(2s - 2s\eta^2 - 2\sigma\eta^2) \tag{3.8}$$

The analytical expression for the ratio between the zonal velocity at some latitude $\eta = \eta_0$ and the equator (i.e., $\eta = 0$) is simply

$$\frac{U_1(\eta_0)}{U_1(0)} = e^{-\eta_0^2/2}\left(1 - \eta_0^2 + \frac{1}{3}\eta_0^2\right) \tag{3.9}$$

where the 1/3 factor comes from using the dispersion relation (3.2) with $j = 1$, to substitute in for σ/s. Squaring (3.9) to get the kinetic energy ratio KER, and using dimensional variables, yields

$$KER = \left[\frac{U_1(\eta_0)}{U_1(0)}\right]^2 = e^{-\beta y_0^2/c}\left(1 - \frac{2\beta}{3c}y_0^2\right)^2 \tag{3.10}$$

56

A latitude of $0°31'$ corresponds to roughly 57 km. At this latitude, KER attains a value of 0.31. This is smaller than the values of 0.88 and 0.61 obtained from the April 1982 and all 3 cruise observations, respectively. The marked discrepancy seems to contradict all the previous indications leading towards the single Rossby wave mode hypothesis. In trying to work our way around this road block, we will eventually refine our interpretation of the data, to make it comply with the totality of the observations.

3.4.2 Adding zonal modulation to the signal

The gap between analytical and observational KER values can be reduced by the following considerations. Data used in power spectra calculations at off-equatorial latitudes come from two longitudes only ($138°W$ and $145°W$), while equatorial estimates include casts collected at seven or eight different longitudes (see Fig. 2.1). A zonal modulation of the signal amplitude could produce deficient estimates of KER. This would be the case for a wave packet containing a number of several different zonal wavenumbers. The modulation is a manifestation of the particular bandwidth and distribution of energy among the various spectral components making up the wave packet. Another interesting situation leading to similar effects concerns transient forcing. In this case, we would be seeing the time modulations imposed by the forcing, as the wave carries energy westward and downward from the generation region. However, for waves with time scales of a few years, it is hard to relate any time changes occurring over one year with transient forcing mechanisns.

There is a suggestion of zonal inhomogeneity in the records. In particular, spectra computed at Q sites ($153°W$) for April 1982 show values of power markedly lower (by a factor of 3) than at all the other sites to the west. If data from Q casts is excluded from power calculations at the equator, experimental values of the KER for $0°31'$ latitude decrease to 0.62 for April 1982, and to 0.54 for the three cruise case, as compared with 0.88 and 0.61 previously mentioned (see Table 3.1). Furthermore, if we take the

limiting values, as implied by the 95% confidence error bars, we can make the KER experimental values consistent with the analytical value of 0.31 for the first meridional Rossby wave modes with vertical wavelength of 560 sm.

Long Rossby waves have westward phase and group velocities. Because they carry energy towards the west, any zonal modulation in amplitude will propagate in that direction. The fact that a significant lower value in power amplitude is observed at the westernmost PEQUOD site Q may be suggesting that the most energetic part of the signal had not reached that longitude in April 1982. Site Q is separated from the nearest equatorial site P by 5° or roughly 600 km. It is conceivable that, over such distance, the flow amplitudes would be sufficiently modulated to generate the apparent trend in the records.

If we are indeed in presence of a situation as the one we have just outlined, a number of interesting questions could be raised at this point. One of the most pertinent is whether there is any indication of energy propagation at $\vartheta = 560$ sm into the PEQUOD region, between cruises. After all, the observations were taken in two consecutive years, and values for the group velocity of long Rossby waves with periods and zonal wavelengths under consideration here, are on the order of 150 $km/month$. Energy propagating at these speeds can sweep in or out of the PEQUOD observational array over time intervals of one year or so.

To answer the question just posed, we have to look at zonal velocity power spectra computed for different cruises. Fig. 3.2 is revisited here as Fig. 3.7, where we have included straight lines in each power density plot to mimic the background spectrum levels. The lines are more or less arbitrary and drawn by visual inspection. Use of spectra calculated by averaging over wavenumber bands also helped in defining background levels, but because smoothing of the signal was inevitable in those cases, they did not serve our purposes any better than the selected spectra. Fig. 3.7 illustrates the following important point. The power amplitudes for February and April 1982 are
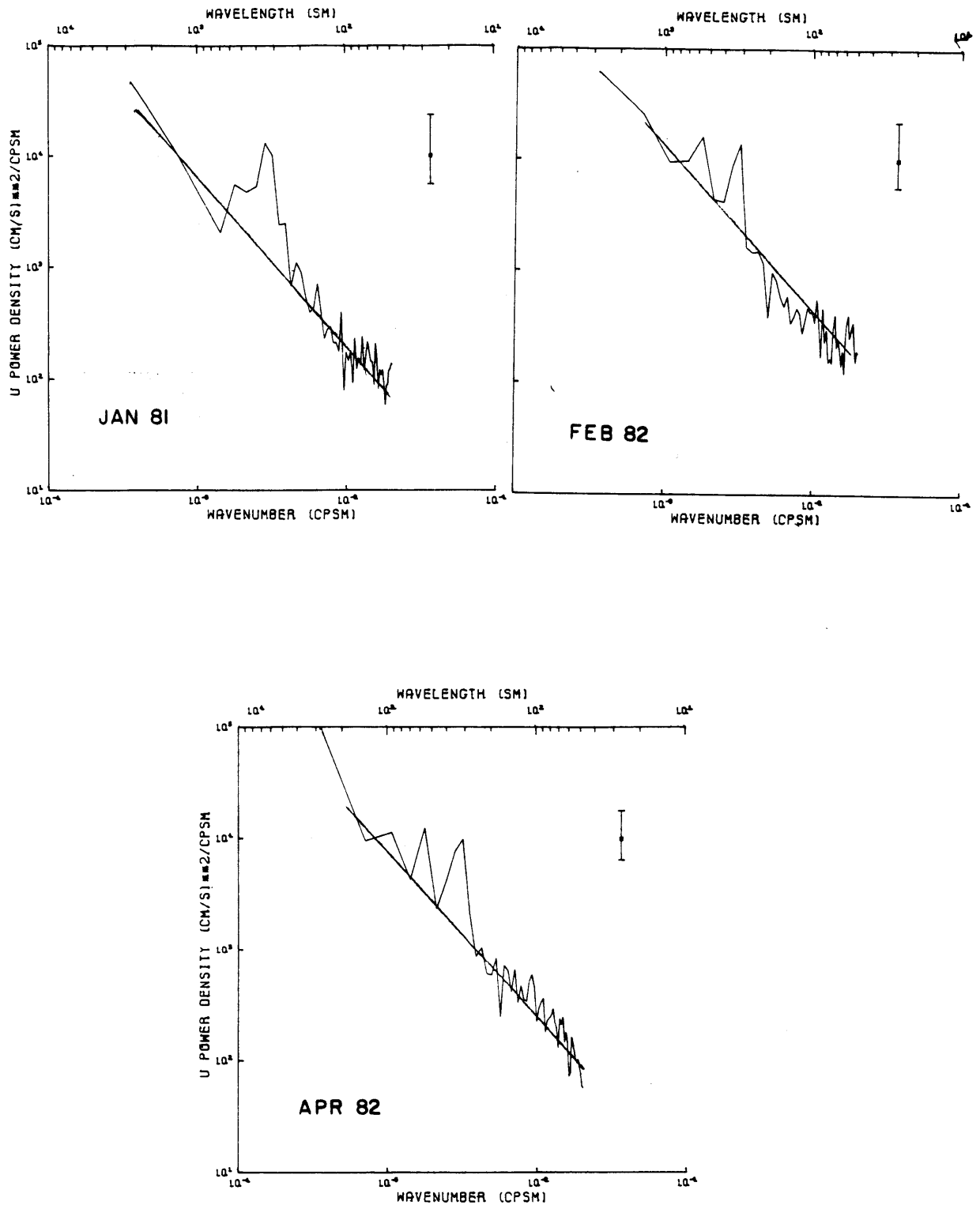
Fig. 3.7. Same as Fig. 3.2, but here we have drawn straight lines on each plot to represent background power levels. These were chosen more or less arbitrarely from a visual inspection of the spectra.

59

bigger by roughly a factor of 2 or 3 than for January 1981, in contrast, for example, with the much more regular amplitudes evident for the deep jets peak. This indeed strongly confirms the energy propagation idea previously inferred just from the zonal structure of kinetic energy for the April 1982 cruise. The more energetic signal is able to travel from the east into the PEQUOD array, during the time elapsed between the first and last two cruises, but does not seem to make it to the westernmost Q site. It would be most interesting to see whether Firing's (1987) data, collected at 159°W between March 1982 and June 1983, exhibits any behavior corroborating our findings. An increase in power amplitudes at relevant vertical scales should be observed at some time during Firing's measurements. No such analysis has been performed on that data set as far as I know.

At this point, it is important to establish the possibility of having a sufficiently wide band spectrum in zonal wavenumbers to produce the modulations seen in the power spectra, without disrupting at the same time the previous analysis. In particular, if we want to maintain the assumption of having an extreme narrow band process in the frequency domain, the range of values of λ is then constrained by the dispersion relation (3.3). The spectral results at 560 sm represent an average over the approximate band 630–510 sm, centered at that wavenumber. It is plausible that we are in presence of a finite narrow band phenomenon in vertical wavenumber, rather than having a single ϑ component in the records.

If we require the signal to be made of a single frequency, then from the dispersion relation (3.3), we have

$$T \sim \frac{\lambda_l}{\vartheta_l} \sim \frac{\lambda_u}{\vartheta_u} \tag{3.11}$$

where subscripts l and u refer to the upper and lower values of λ and ϑ which define the bands $\Delta\lambda$ and $\Delta\vartheta$. Assuming rough values of $\vartheta_l = 510$ sm and $\vartheta_u = 630$ sm, we arrive at

$$\lambda_l \sim 0.8 \quad \lambda_u \tag{3.12}$$

60

Our purpose is to try to determine whether constraint (3.12) permits modulations at zonal scales seen in the data, for reasonable values of λ_l. It is clear that the data set is not suited for extracting any particular distribution of energy over the band of zonal wavelengths $\Delta\lambda$. Even selecting values for λ_l or λ_u is a more or less arbitrary process. Nevertheless, a simple example calculation will illuminate the point.

The classical case of wave modulation, presented in many textbooks on the subject, consists of having 2 waves of *slightly different* frequencies or wavenumbers interfering with each other (see, e.g., Lighthill (1978)). In that case, the amplitude varying factor modulates the field at scales much longer than the dominant period or wavelength. In the records, we seem to have modulation at scales comparable with the zonal wavelengths present. That imediately calls for some wide $\Delta\lambda$ if we want to be successful in reproducing qualitatively the results. In our example, we assume that only two zonal wavelengths make up the records. The value $\lambda_l = 7000\,km$ seems a reasonable choice for the shortest wavelength, in light of results given in Table 3.3. From relation (3.12), we choose $\lambda_u = 9000\,km$. The sum of 2 sinusoidal wave with zonal wavenumbers k_l and k_u can be expressed mathematically as

$$u(x) = 2\cos\left[\left(\frac{k_u - k_l}{2}\right)x\right]\cos\left[\left(\frac{k_u + k_l}{2}\right)x\right]$$
$$= A(x)\cos\left[\left(\frac{k_u + k_l}{2}\right)x\right] \tag{3.13}$$

where $A(x)$ is the modulation factor. For the chosen values of λ_l and λ_u, the zonal wavelength of the modulation is

$$\lambda_M = \frac{4\pi}{k_u - k_l} \sim 64000\,km \tag{3.14}$$

With these wavelengths, if we look at a region roughly $3000\,km$ away from a node, we can double the power over zonal distances as short as $1000\,km$. The closer we get to the node in energy, the shorter the distance necessary to double the power. The scales

over which modulations occur get larger for choices of λ_l bigger than 7000 km, as taken here. This seems to point to values of λ at the lower range of Table 3.3, if we want to succeed in interpreting the data with the help of these ideas.

This simplified example serves to illustrate the possibility of explaining the apparent zonal changes in signal amplitude in the observations, by allowing for a zonal wavenumber spectrum with a finite bandwidth Δk. It is not an attempt at defining the exact shape and composition of that same spectrum. A completely different data set would be required to pursue that goal.

A final word should be said about the implications of introducing a finite bandwidth Δk on the results inferred previously in subsection 3.4.1. Estimates of zonal wavelength based on linear fits of coherence phase $vs.$ zonal lag plots, as done in Fig. 3.3, will necessarily yield an averaged value of the wavelengths present in the data. In that sense, the results displayed in Table 3.3 are still valid, if interpreted accordingly.

3.4.3 Concluding remarks

The discussion of the previous subsections leaves us with the following scenario concerning the 560 sm signal. The energy at that band is associated primarily with first meridional mode long Rossby waves of periods on the order of 4 years. The bandwidth Δk allows for gradual zonal modulation of the amplitudes to occur. The more energetic part of the signal travels into the PEQUOD observational array from the east, between January 1981 and February 1982, accounting for the observed increase in power. This does not mean that no signal was present at the time of the first cruise. Significant phase propagation detected between data collected on January 1981 and on the other cruises attest to this fact. The signal was observed on all three cruises, although it was weaker during the first visit made to the PEQUOD sites.

The lack of zonal coherence found in February (as compared with April cruise), an issue we have left out of the discussion until now, can not be justified in terms

of zonal propagation of energy, because it occurs only two months before the strong April coherence results (see Table 3.2). Time scales involved are not fast enough to account for this observation. Instead, we resort to signal to noise ratio arguments to explain it. Fig. 3.7 displays a clear rise in the background power levels in February as compared with the other two months. The best signal to noise ratio happens in April 1982, where the highest coherence amplitudes were found. Even though the amplitudes of the power peaks at $\vartheta = 560\, sm$ are pretty much the same for February and April, the higher background levels in February have the effect of reducing the signal to noise ratio for that particular cruise. I believe this increase in noise levels is responsible for the discrepancy in coherence results between two last cruises.

The higher background levels are present at the largest vertical scales and the cause behind them remain ambiguous, to say the least. The event seems confined to the February cruise. It is possible that, at that time, some energetic event was taking place at the site of the measurements, but we would expect to see it two months later, unless the event consisted of a packet of energy which quickly traveled in and out of the observational region. Kelvin waves are the natural candidates here, since they are the fastest carriers of energy in the equatorial regions. Drastic changes in the state of the upper ocean occur in 1982, as part of the very strong 82/83 El Niño (Voorhis *et al.*, 1984). These changes can provide the forcing mechanisns necessary to generate the hypothesized event.

We may wonder why the signal is strong enough to give significant time-lagged coherence results, while failing to yield equal results for zonally lagged coherences, for all three cruises. That may be a manifestation of the character of the noise fields. It is reasonable to assume that other equatorial waves make up the rest of the energy seen in the spectra, as some studies have advanced (Eriksen, 1980; Eriksen, 1981). The zonal decorrelation scales of these "noise" waves tend in general to be roughly of the same magnitude as the zonal distances separating PEQUOD sites. On the other hand,

their time decorrelation scales may be assumed to be shorter than one year. It is thus plausible that zonal coherences are more sensible to noise levels.

The simplest possible interpretation of the records in terms of linear equatorial waves has been offered here. We could certainly have tried some variations in the explanation of the 560 sm signal advanced here. The first that comes to mind is probably to allow for time (instead of zonal) modulation in the records, by relaxing the extremely narrow band assumption in the frequency domain. Even though this is a fair hypothesis, we found it conceptually more pleasant to work on the single frequency idea because of the evidence for zonal inhomogeneities in the power spectra calculations.

We will defer any discussion on how these flows are possibly forced until a later section, since this issue also has to do with the interpretation of the other strong zonal velocity spectral peak which we now pursue.

3.5 Interpreting the deep jets signal

The dynamical nature of the EDJ flows and the basic reason for their existence has recently been the topic of general debate among physical oceanographers. A preliminary look at data collected during all three branches of the PEQUOD program revealed an apparent lack of vertical propagation. This prompted some modelers to abandon the previous belief that the EDJ were basically describable in terms of linear equatorial waves. Our approach is to explore (and if possible to exhaust) all the simple linear wave ideas, before looking for other more complicated explanations of the jets.

3.5.1 Does the signal show downward phase propagation?

One of the surprising revelations of section 3.3, displayed most clearly in Fig. 3.5, were the positive time-lagged coherence phases obtained for the deep jets band ($\sim$ 400– 311 sm). If we take those results literally, they immediately imply upward energy propagation at those wavenumbers, with phase propagating in the opposite direction.

Table 3.5. Estimates of T, T_{max} and T_{min} (in years), calculated from time-lagged coherence phases plotted in Fig. 3.4.

$\vartheta(sm)$	T_{min}	T	T_{max}
400	5	6.7	12
350	6	9.1	14
311	8.5	17	56

Even though we are reluctant to accept that such an event could be happening, on the grounds of the brief considerations previously made on this issue, we can not disregard it as totally impossible. We shall continue to examine this possibility, and see if it will lead us to some consistent overall picture of the deep jets.

As it was the case with the 560 sm signal, the zonal tilt of lines of constant phase inferred from zonally lagged coherence calculations, together with the sign of the vertical phase speed c_z, determine whether the zonal phase speed c_x is eastward or westward. In our case, with phase lines tilting downward towards the east and $c_z < 0$, we have phase propagating westward. Following the same line of reasoning as we did when interpreting the 560 sm signal, long Rossby waves seem the sole candidate to explain the observations.

We can extract values for the periods from the coherence phase $vs.$ time lag plots of Fig. 3.5, by fitting a straight line through the phase points. The 95% confidence error bars provide for estimates of maximum and mininum periods, T_{max} and T_{min}, suggested by the coherence phase results. The values obtained by this method are featured in Table 3.5. We again emphasize the uncertainty involved in the above procedure, when only essentially two data points are available to do the calculations. The large size of the error bars do not help the cause either. As we will soon discuss, interpreting phase plots as the ones in Fig. 3.5 can be a very treacherous and ambiguous task.

An interesting aspect of the periods displayed in Table 3.5 is their increase with decreasing vertical wavelength. If we consider that, by expressing the frequency as $\omega = c_z m$ where m is the vertical wavenumber, the vertical group velocity c_{g_z} (i.e., $\partial_m \omega$) can be written as

$$c_{g_z} = c_z + m\frac{\partial c_z}{\partial m}$$

one can then estimate its value from the results of Table 3.5. The inverse relation between period and wavelength implies that $\partial_m c_z > 0$ and in fact, a rough finite difference estimate of this slope evaluated at the middle wavelength yields positive values for c_{g_z}, a result which curiously points again towards upward propagation of energy.

From the results displayed in Table 3.5, it is clear that to be able to maintain our simple and perhaps naive interpretation of the time lagged coherence phases, we will have to deal with waves of almost absurd time scales. Estimates of T_{min} are all larger than 5 years. We might be willing to accept waves with periods around 4 or 5 years, invoking for example El Niño type forcing as the mechanism behind them, but we ought to question the existence of wave motions at periods longer than 5 years on the grounds of dissipation, absence of strong forcing (at least known to us) at these frequencies, and possibly strong nonlinearities. Periods larger than 5 or 6 years are suspicious, to say the least.

We can also use the dispersion relation (3.3) for long Rossby waves and the estimates for zonal wavelength λ given in Table 3.3 to calculate the period T, for the 350 sm band. For a zonal wavelength $\lambda = 15800\,km$, we obtain $T = 14$ years (for the first meridional mode). Taking the lowest value $\lambda_{min} = 10100\,km$, yields a value of $T_{min} = 9$ years. We again get very large estimates for the period T associated with the deep jets wavenumber band. They would get even larger if we considered higher meridional mode numbers.

Another difficulty arises when we compare the latitudinal energy scaling observed at 350–311 sm with the theoretical predictions based on expression (3.10) for long Rossby waves. The values attained by KER, for $y_0 = 57\,km$, are 0.14 and 0.10 for $\vartheta = 350\,sm$ and $\vartheta = 311\,sm$, respectively, as compared with the observational values of 0.43 and 0.58, in fact much more consistent with Kelvin wave scaling (see Table 3.1). If the analytical values were realized, we would probably not see any peak in power spectra computed from casts D, F, L or N, since at those sites the power amplitudes would be only 10% of what they were at the equator, and indeed already at the noise level. This is not what we observed in the PEQUOD data.

The prospects for the long Rossby wave hypothesis advanced in this section are certainly bleak, after the above considerations. The only reason suggesting Rossby waves as an explanation of the signal, was the apparent downward phase propagation extracted from the most simple interpretation of the time-lagged coherence phases. However, other slightly more involved ways of rationalizing the coherence phases may lead to a completely different scenario, as far as interpreting the EDJ is concerned. Thus, we abandon the Rossby wave hypothesis as unplausible on the grounds of the results found on this section, and proceed to explore other possible paths still available to us.

3.5.2 Other interpretations of the time-lagged coherence phases

Let us assume that the EDJ signal is composed of waves propagating energy downward. If only one wave was responsible for the records, we would certainly expect to see clear upward propagation of phase from the time-lagged coherence calculations. That will not in general be the case, if we allow a number of waves, each of a different frequency, to coexist in the records. Depending on the particular spectral composition, the coherence phase will have a more complicated behavior as a function of time. The simple linear character of the relation between phase and time is certainly lost.

Assuming that we primarily have waves with upward propagating phase in the signal, the tilting of east–west phase lines down towards the east implies $c_x > 0$ (i.e., eastward). Our choice in this case is restricted to the Kelvin wave, since the mixed Rossby–gravity wave has no zonal velocity signal at the equator. Furthermore, the meridional scaling of the EDJ compares very well with the prediction based on Kelvin wave arguments, as shown in Table 3.1. It is thus only natural that we assume the basic Kelvin wave signature of the jets. Eriksen (1981) had already advanced the same hypothesis, based only on latitudinal energy scaling arguments and on computations of coherence between zonal velocity and vertical displacement. However, in his spectral approach, he included only waves with periods shorter than one year. I believe much longer time scales are needed to be consistent with the very large λ suggested in results of Table 3.3. The dispersion relation for Kelvin waves, given as expression $(A.11)$ in Appendix A, can be written in dimensional form as

$$T = \left(\frac{2\pi}{N_0}\right)\frac{\lambda}{\vartheta} \tag{3.15}$$

Using the estimates of λ and λ_{min} given in Table 3.3 for $\vartheta = 350\, sm$, (3.15) yields values of $T = 4.7$ years and $T_{min} = 3$ years.

At this point, the obvious question to ask is whether we can make up a simple sum of linear Kelvin waves, of different periods and zonal wavelengths defined within reasonable bandwidths, all with $c_z > 0$, and capable of explaining the time-lagged coherence phases. The definition of the frequency bandwidth $\Delta\omega$ associated with the jets is crucial in determining the behavior of the phase function with time. It is clear that if we allow high enough frequencies to be present in the records, then aliasing can occur and the apparent downward propagation suggested by the positive phases of Fig. 3.5 could actually be due to the upward propagation of the fast waves, over roughly one year. Periods comparable with time lags available (13 or 15 months) would be needed, if this effect were to be observed. However, for waves of time scales close to 1

year, significant phase propagation should show up in the time-lagged coherences done between the February and April 82 data sets. Such is not the case, as can be seen in Fig. 3.5.

Using the previous estimates of T_{min} inferred from the dispersion relation (3.15), together with the above considerations, we assume as a working hypothesis that only waves with periods between 3 and 5 years are present in the records. It is not obvious, beforehand, that a linear sum of upward propagating Kelvin waves of such bandwidth $\Delta\omega$ will be capable of reproducing the positive phases shown in Fig. 3.5. The upper value of 5 years is more or less arbitrary, but seems to be a reasonable choice. It will not be of any importance in this case, anyway. The values of T_{max} and T_{min} imply a range of zonal wavelengths from 10000 km to 16000 km, roughly as obtained from the zonally lagged coherence calculations.

In general, the distribution of energy among the different spectral components can be very complex. However, we can not resolve from the data set the particular frequencies which may be present in the records at the vertical wavenumbers associated with the EDJ (nor for that matter can we attempt to assign spectral energy levels to each frequency). To illustrate how a sum of upward propagating waves can give rise to downward phase propagation over some periods of time, we consider the simplest situation where only two frequency components are present in the records. We should stress that the example given here is not intended to be a model of the observations, but rather to show that the behavior of the time-lagged coherence phases can be rationalized in terms of simple sums of upward propagating Kelvin waves of reasonable periods. Suppose we have two linear waves of equal amplitude, propagating both in the same direction, with periods $T_1 = 3$ years and $T_2 = 4$ years. The situation can best be depicted as a sum of two vectors (or phasors to use the electrical engineering terminology) whose lengths are proportional to the amplitude of each wave and whose relative angles reflect the phase differences between each wave component. Fig. 3.8

69

T=1 YR
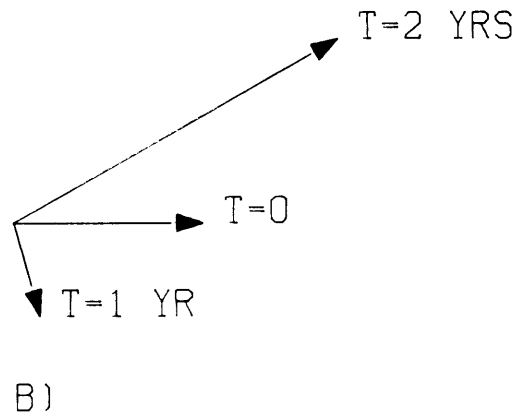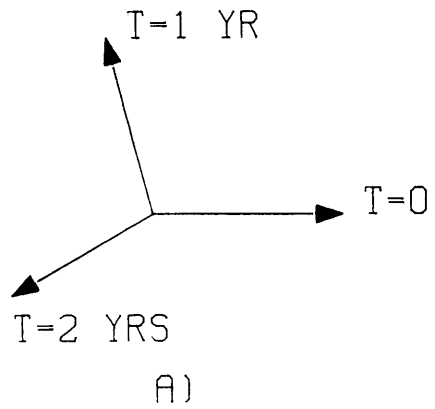
T=0

T=2 YRS

A)

T=2 YRS

T=0

T=1 YR

B)

Fig. 3.8. Phasor diagrams for the case of two waves of equal amplitudes and periods $T_1 = 3$ years and $T_2 = 4$ years, rotating both counterclockwise. Only the resultant phasor is shown. In a) the two components are in phase at the initial time $t = 0$, while in b) the wave with period T_1 leads the other by 160°.

displays the phasor diagrams relevant to this example. Both wave components rotate counterclockwise with time. Only the phasor resulting from the sum of the two waves is shown. We are interested on the behavior of the phase function $\theta_T(t)$. If at an arbitrary time t_0, the two waves are in phase, then the resultant phasor will rotate with time in the same direction of the phasor components, at least for a number of years (Fig. 3.8a). In this case, the sense of propagation inferred from the records would correspond to the actual direction of propagation of each individual wave. However, if at t_0 the two components are not in phase, it may happen that the rotation of the resultant phasor will be in the opposite sense of the component phasors. Fig. 3.8b shows the case where initially the 3 year period wave leads the other by 160°. After 1 year, the resultant phasor has rotated clockwise, even though the two components both rotate counterclockwise. Thus, a naive interpretation of these presumed records could lead to very faulty conclusions about the implied direction of phase propagation. This deceiving behavior of the phase function with time is obviously sporadic. Also displayed in Fig. 3.8b is the resultant phasor after 2 years, showing again counterclockwise rotation with time, as it is the case in the most general situations.

However simple this example may be, it serves to illustrate two important points. It is evident that only for certain initial phase differences between components will the phase function $\theta_T(t)$ behave as in the diagram of Fig. 3.8b. If we have a continuous spectrum of *randomly* phased waves, all propagating in the same direction, the phase function $\theta_T(t)$ will not display on the average any erratic behavior, as can easily be derived mathematically. On the other hand, if the different waves are phase-locked, there is a higher probability of finding the sort of behavior illustrated in Fig. 3.8b. The suggestion is that, if the interpretation given here is valid, the deep jets signal may consist of a packet of phase-locked (rather than randomly phased) upward propagating Kelvin waves, with the different frequencies becoming out of phase as the packet evolved in time.

The second interesting point about the example given is related to the fluctuations in the amplitude of the resultant phasor observed in Fig. 3.8. It is not surprising that significant changes in power levels should be observed due to the time modulation factors occurring whenever two or more frequencies are at work. In fact, for the case of Fig. 3.8, the waves will come in or out of phase every 12 years. This time interval would increase if T_1 and T_2 were closer (i.e., if the frequency bandwidth $\Delta\omega$ were smaller). The more frequencies are included in the linear sum of waves, the more complicated is the structure of the time modulation factor (and also the phase function $\theta_T(t)$). The observations do not show any major differences in the power densities recorded between cruises, but it is not difficult to accommodate for changes by factors of 3 or 4, given the size of the 95% confidence error bars on the power estimates.

3.5.3 Concluding remarks

The following picture has emerged from the discussion offered in the last sections, concerning the possible interpretation of the EDJ within the linear equatorial wave theoretical framework. The observations are *not* inconsistent with the presence of a packet of Kelvin waves with upward phase propagation. A rough measure of the allowed range of periods yields 3 and 5 years for the values of T_{min} and T_{max}, respectively. Corresponding values for zonal wavelengths λ are 10000 km and 16000 km. Allowing for a finite bandwidth $\Delta\omega$ is crucial in rationalizing the time-lagged coherence results. The jets are best defined as a finite narrow band process in vertical wavenumber, spanning the 350 and 311 sm bands (and possibly the 400 sm band also).

It is unfortunate that only essentially three data points in time are available to check for phase propagation. A more extensive time coverage would certainly be more conclusive, as far as the propagation issue is concerned. There are other available profiler data, collected roughly in the same region (Leetmaa and Spain, 1981; Firing, 1987), which could be used to extend our records in time. But, on the grounds of what

has been said about the issue of measuring phase propagation, only a carefully done overall Fourier analysis of all data sets would give reliable results.

Firing (1987) explicitly compares his data with the profile collected by Leetmaa and Spain at 159°W in 1980, and he finds a good match between them, if the profile obtained by averaging all his equatorial data is shifted upward by 130 m or downward by 220 m. If these depth changes were caused by vertical propagation, they would imply either a 6.5 year period wave propagating downward or a 4.1 year wave propagating upward. He then goes on to argue that the expected vertical displacement of the jets (65 m down or 110 m up) are not apparent from a visual inspection of his raw velocity records, thus concluding that "...the jets did not propagate steadily from 1980 to 1983." At the same time, he also notes that many of the jets are shallower by roughly 50 m at the end of his 16 month records. I think the only conclusive statement we can draw from his analysis is that the jets do indeed seem to shift vertically over long enough periods of time. The fact that the jets are a narrow band phenomenon imbedded on a broad band energetic background and their apparent long time scales, make it virtually impossible to say anything about vertical propagation from a visual inspection of the records. Since equatorial waves have vertical phase and group speeds which are opposite in direction, it is doubtful that the eye can differentiate between energy and phase propagation effects. Furthermore, if a finite bandwidth $\Delta\omega$ is involved, perhaps we should not put too much faith in observing nice linear relations of phase with time, as we have extensively argued before. These are in fact two of the major consequences of assuming the jets to be a finite narrow band process in vertical wavenumber and frequency, rather than being composed of a single wave mode.

As a final comment, it is fair to say that without settling the propagation issue (and that will require a time series lasting several years), both wave and steady models, or wave-mean flow models, remain potentially important in the quest to understand the basic dynamics governing the deep jets.

3.6 Discussion

The prospects for the existence of very long period waves in the equatorial Pacific raise many important questions. Are these waves generated at the surface by wind or thermal forcing? Or can they be related instead to some instability mechanism? How is the phase and energy propagation affected by friction? Are there important nonlinear effects?

The tropical Pacific is a region of strong interannual variability, with El Niño events occurring every four years or so. It is very tempting to relate the apparent long time scales of the waves of sections 3.4 and 3.5 to this variability. The presence of a peak in the atmospheric forcing spectra at appropriate frequency and zonal wavenumber bands, would provide an easy explanation for the appearance of a particular dominant short vertical scale in the oceanic response. Unfortunately, knowledge of the atmospheric input functions at the low frequency end of the spectrum is virtually nonexistent (not to speak of information on the zonal wavenumber spectral structure). The longest surface wind data sets analyzed to date (Goldenberg and O'Brien, 1981; Luther and Harrison, 1984) are still inadequate to resolve the spectral character at low ω.

The details of how the atmospheric energy input is transmitted to the ocean are also very poorly known. Since the upper ocean response to surface forcing is strongly nonlinear (Philander and Pacanowski, 1984), we should not expect any simple relation between the atmospheric forcing functions (i.e., wind stress, heat flux) and what is really happening in the ocean interior. For the deep ocean, it is probably more reasonable to assume some kind of parameterization of the forcing, distributed over a broad oceanic upper layer, thus neglecting all the poorly known details about how energy is initially transferred to the ocean. For instance, fluctuations in the heat content of the upper layers of the ocean may act as forcing mechanisms for waves of periods on the order of 3 or 4 years. Such fluctuations could very well have some energy at these low frequencies, as some models of El Niño seem to imply (Cane and Zebiak, 1985).

74

The issue of how energy propagates vertically in the tropics is itself an open one. For a realistic mean stratification, it has been suggested (Gent and Luyten, 1985) that most of the energy generated by atmospheric forcing at the ocean surface becomes trapped in the upper layers, due to reflections off the sharp thermocline. This effect is strong for long vertical wavelengths, but for the jet scales they predict roughly 60% of the incident energy would be able to reach the ocean bottom, if friction and reflections off the oceanic lateral boundaries are not considered. The inclusion of these latter effects would most probably decrease the given estimate. In addition, the upper ocean mean circulation provides the possibility for critical layers to play a role in the absorption of energy associated with higher baroclinic modes. These processes have actually been simulated in a study by McPhaden *et al.* (1986). Thus, it seems problematic to maintain that the waves associated with the EDJ are actually forced at the surface.

In the search for alternative forcing mechanisms, the thermocline region gains some relevance. It is not unreasonable that the vertical displacements of the thermocline can be thought of as inducing a pattern of vertical velocities at the base of the strongly stratified region, and in that way, inject energy into the deep ocean. Convergence or divergence associated with the Undercurrent can also induce vertical velocities (Wunsch's (1977) model ocean is forced in a similar way). These driving mechanisms would avoid the problem of energy reflections or critical layer absorptions occurring at the upper ocean. But still, some problems remain on the horizon. By virtue of the very long time scales of the Kelvin and Rossby waves advanced in the interpretation of the zonal velocity signals, energy travels along rays which make very small angles with the surface. For example, in a constant $N = 2 \times 10^{-2} s^{-1}$ ocean, the energy associated with a Kelvin wave of period equal to four years, generated at the surface in the western Pacific, travels along a ray that only reaches roughly 400 m depth, before striking the eastern boundary. For long Rossby waves of the same period, forced in the eastern Pacific, energy rays will strike the western wall at depths of approximately 1000 m.

Unless other effects come into the picture, these waves (especially the Kelvin wave) would need several side reflections before they could reach significant depths. Furthermore, several years would be needed for the energy to propagate 1000 meters or so into the ocean interior (basically, for equatorial waves with vertical group and phase speeds equal and opposite, energy travels a distance of one vertical wavelength over one period). Thus, friction is expected to play a significant role over such long time scales. It remains to be seen whether the kind of waves invoked in sections 3.4 and 3.5 will be able to survive possible frictional losses over several years.

In addition to peaks in atmospheric forcing spectra, instability processes may also give rise to energetic motions at particular scales for which maximum growth rates occur. In some cases the most unstable wave may occur at a given frequency and zonal wavenumber, thereby setting the vertical wavelength of the flow, while in other cases the instability may directly favor a given vertical wavenumber. Present knowledge of equatorial instabilities is by no means satisfactory, but the few available studies on the subject provide us with an opportunity to check whether the predicted fastest growing scales correspond to the ones apparently observed in the PEQUOD records. For example, Philander (1976, 1978) used a two-layer model to look at instabilities associated with realistic meridional profiles of surface currents and found the most unstable waves at periods of about one month and zonal wavelengths on the order of 1000 km. More recently, Hayashi and Young (1987) analysed the instability of a zero potential vorticity basic state, associated with a one-layer zonal current bounded by two fronts at which the layer depth vanished. For parameter values which lead to a mean flow qualitatively resembling equatorial surface flows, the most unstable waves occur at similar zonal and time scales as found by Philander. These are too small to explain the signals observed in the PEQUOD records. Perhaps a more promising result was that found by Boyd and Christidis (1982, 1983) for a stratified ocean with a mean zonal flow varying in latitude only (no baroclinic instabilities present). In this

study, growth rates increased with vertical wavenumber, but for realistic values of mean meridional shear, the zonal and vertical scales of the observed signals do not correspond to any peak in growth rates computed in Boyd and Christidis (1983). It thus remains to be seen whether the existence of deep energetic zonal currents found in the records is somehow related to instabilities of the equatorial ocean basic state.

The interpretation of the zonal velocity signals in terms of linear equatorial waves, offered in the previous sections, is perhaps indicative of their basic linear character. Given the values for the periods ($T \sim 4$ years) and zonal wavelengths ($\lambda \sim 12000 \ km$) obtained from the wave analysis, we can estimate the degree of nonlinearity by comparing the magnitude of the terms uu_x and u_t in the zonal momentum equation. For that, we also need a velocity scale U. Choosing a value for this scale is a little ambiguous, since it depends on whether a single or several vertical wavelengths are considered (i.e., although a single wave may have small enough amplitude to be linear in character, the sum of a number of such waves may be nonlinear since the resulting velocity field may become large enough, at least locally). If we take the amplitudes observed for individual vertical wavenumbers, then $U \sim 5 \ cm/s$, yielding a value of the ratio $uu_x/u_t \sim 0.5$. On the other hand, the actual amplitudes of some of the jet-like flows exceed 10 cm/s (e.g., see Fig. 2.2), implying this ratio to be of order one or larger. Thus, although the individual waves invoked here to explain the basic character of the signals may be reasonably linear in character, their superposition may be nonlinear. A study carried out by Boyd (1980) showed that in general one of the effects of nonlinearity is to decrease the wave phase speeds (at least for zonal phase speed). It is not clear how strong this effect could be for the waves under consideration.

We hope to shed some light on the issues raised in this section, in the theoretical work of Chapter 5.

CHAPTER 4
The Background Spectra — Analysis and Interpretation

4.1 Introduction

Our previous efforts have focused primarily on the interpretation of the strong signals observed in the equatorial zonal velocity records. This chapter will be devoted to the analysis of the velocity and vertical displacement data in a more general context.

It is widely believed that deep flows in the tropical oceans are the manifestation of equatorially trapped waves which have been able to propagate their energy into the oceanic interior. Eriksen (1980, 1981) has had some success in trying to model current observations as a spectral sum of various equatorial wave modes. Although his approach is purely statistical (i.e., spectral results are due to the combined action of a large number of randomly phased modes), it is also possible to have a small number of waves dominate the records, thus contributing almost solely to the spectral analysis results. In fact, such is the situation with our zonal velocity records, for the vertical wavenumber bands containing the deep jets, although in that case we have a powerful peak in the spectrum, lying roughly 10 db above the background energy levels. But this is not necessarily the case, i.e., the presence of a small number of wave modes can still occur without involving energetic spectral peaks. Regardless of the particular details, we shall adopt the wave conceptual framework in the quest to understand the general structure and characteristics of the observations. Our goals are to determine if in fact the data supports the equatorial wave hypothesis, and if possible, to define the modal spectral composition and isolate any particular modes present in the PEQUOD data.

The existence of equatorial waves in the records can be checked in several different ways. Among other things, we should expect energy to be trapped to the equator and significant correlations to occur between the dynamical variables u, v and ς. Periodicity in the records along with significant zonal correlations may also show up for

some vertical wavenumber bands, depending on the frequency and zonal wavenumber bandwidths under consideration. In general two different situations may occur. If at some vertical wavenumber, the mixture of modes can be described as a narrow band process in frequency and zonal wavenumber, then we have the best chance of finding significant coherence amplitudes (for either time or zonally lagged coherence calculations). If, on the other hand, the modal composition is of a wide band nature in k and ω, time and space (zonal coordinate) decorrelation scales will be short, affecting coherence results accordingly. Zonal and time lagged coherences will dictate whether the underlying wave spectrum at each particular vertical scale has a wide or narrow band character.

Before presenting any results, we should perhaps outline the general strategy we will follow to look for hints of wave motions in the records. Our data set was taken in three different cruises and spans roughly fifteen degrees of longitude. It is not obvious that data taken over such different places and times will be homogeneous, i.e., the modal composition may vary from place to place or from cruise to cruise. In this sense, using all the data together when computing cross-spectra or time and space lagged coherences may not be justified. However, to get any statistical reliability in the analysis without losing resolution of vertical scales, we are forced to combine all the available records. Thus, we only expect to resolve any wave features which are consistently present throughout the whole PEQUOD array, during the three cruises. At some point, separate treatment was tried for a particular cruise, if the coherence results suggested the presence of a distinguished feature which was not apparent in the other cruises. But, in general, the lack of sufficient realizations when taking each cruise individually was difficult to overcome, and results from these individual cruise calculations were not conclusive. Also, none of these features showed a sufficiently wide band character in vertical wavenumber to justify band averaging in improving statistical reliability. Therefore most of the results presented here will come from analysis done

combining the whole data set. In interpreting the results, we will look for consistent patterns in the different analysis (e.g., significant coherences between u, v and ς at the same vertical wavenumber where phase propagation is seen between cruises). Only sound results will be given consideration.

4.2 Spectral and cross-spectral analysis

A simple prediction of the equatorial wave theory reviewed in Appendix A states that the energy meridional decay scales should decrease with vertical wavelength (i.e., the shorter the vertical scale, the stronger the latitudinal trapping). This relation is independent of the time and zonal scales involved and provides for a very simple test of the wave hypothesis. The exponential factor in the Hermite functions of $(A.6)$, written in dimensional form, becomes $\exp -\{2\pi\beta y^2/2N_0\vartheta\}$. If Kelvin waves dominate the records at all vertical scales, then we should expect the meridional decay scales to decrease as $\vartheta^{1/2}$. In general, such is not the case, but the trapping of energy to the equator should still be more or less apparent in the records, if the spectra are to be described in terms of equatorial waves.

To check for the latitudinal energy scaling in the data, we have plotted in Fig. 4.1 power density estimates for u, v and ς as a function of latitude and vertical wavenumber. The spectral estimates were computed using both piece averaging over all available realizations and band averaging over four adjacent wavenumbers, to increase their statistical significance. The trapping of energy to the equator is clear for all three variables u, v and ς, but most evident for the velocity records. This result was expected because of the inherently noisy procedure used to compute ς profiles from the CTD data. In most cases, the decay scale for vertical displacement and zonal velocity records are much broader than the Kelvin wave exponential scale would predict, suggesting the existence of other modes in the records. Perhaps the only exception to this rule occurs
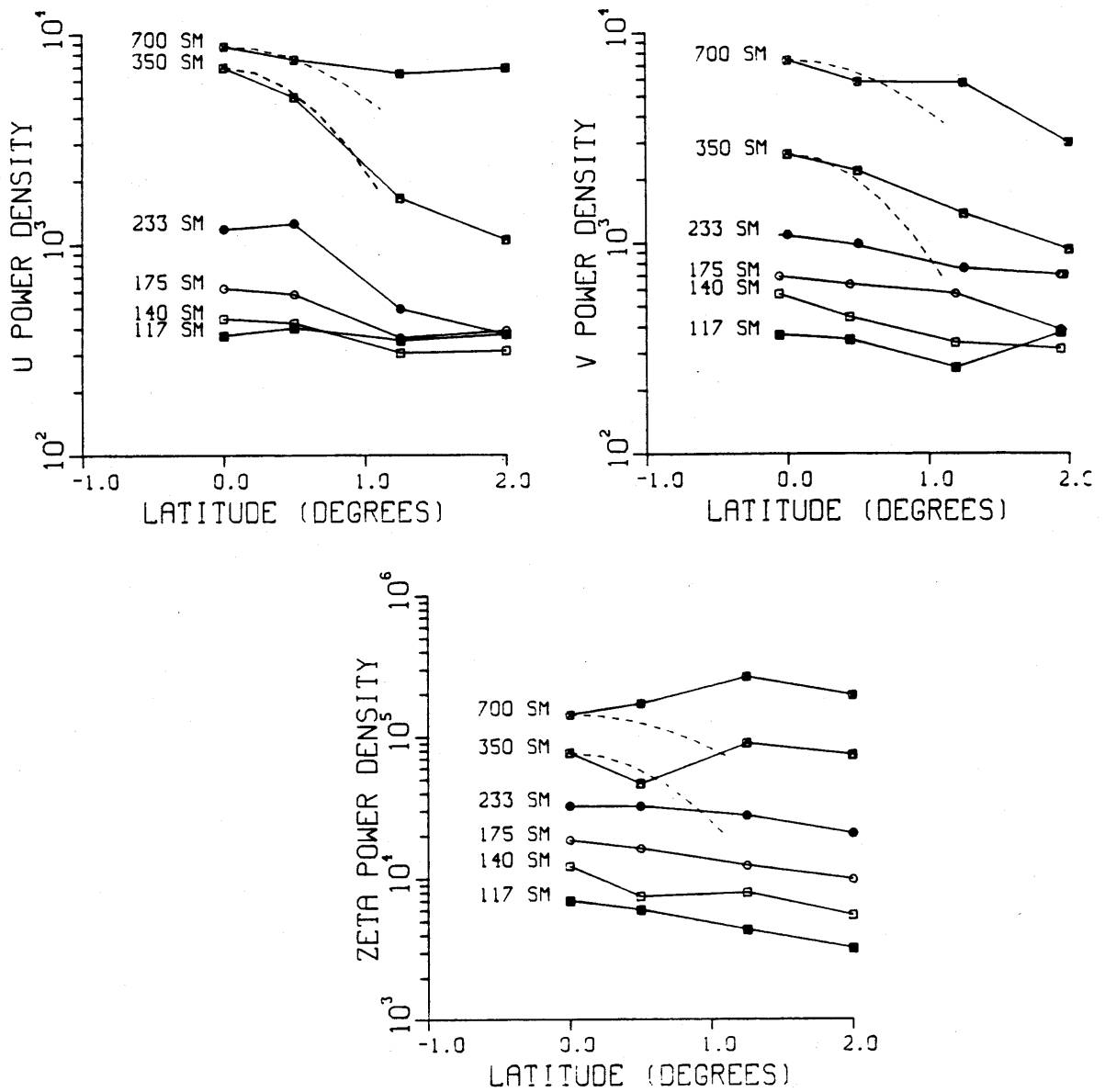
Fig. 4.1. Plots of power spectra estimates as function of latitude for u, v and ς. The dashed lines are the theoretical curves $\exp -\{2\pi\beta y^2/2N_0\vartheta\}$. They are only drawn for the two largest vertical wavelengths, because the others quickly exceed the coordinate range of the plots.

81

for the 350 and 233 sm bands in the u plots. Meridional velocity records show the same broad energy decay away from the equator.

Probably the best way to look for the presence of waves in the records consists in computing cross-spectra between u, v and ς. These variables should be correlated in some manner depending on the specific type of equatorial wave mode making up the records (the distinct correlation patterns will be discussed in the following section, when interpreting the results). To carry out this analysis, we basically took every cast collected at the same latitude and computed coherence between the pairs uv, $u\varsigma$ and $v\varsigma$. Since for equatorial waves, the zonal velocity and vertical displacement fields have the same symmetry about the equator, we combined both south and north profiles for the $u\varsigma$ pair calculations. For the other two cases, the variables involved have opposite symmetry, therefore we kept south and north casts separated. Computations were done both without wavenumber averaging to retain high resolution of vertical scales, and with averaging over two adjacent bands, but only the first results will be presented here. We do not consider wavelengths shorter than roughly 100 sm in the discussion.

Table 4.1 summarizes the relevant coherence pairs found from the cross-spectral analysis performed on the data. The interpretation of the given coherence phases is very ambiguous. The existence of single modes in the data would imply phases of $\pm 90°$, $\pm 180°$ or $0°$ between variables, depending on the particular waves present, as it will be discussed in the next section. However, even a very simple mixture of modes would allow the phases to take on any values. Here, we chose to interpret all the significant phases in terms of the most simple picture (i.e., the single mode hypothesis). In almost all the cases, the 95% error bars encompassed the values of either 0, $\pm\pi/2$ or $\pm\pi$. Entries in Table 4.1 were determined using these error brackets, hence they do not necessarily correspond to the exact observed phase values. The frequency of coherent pairs decreases markedly as we move away from the equator and it is mostly associated with the $u\varsigma$ pair in general. Only results for latitudes of $0°$, $0.5°$ and $1.25°$

Table 4.1. Results from cross-spectral analysis of the PEQUOD data. Entries are the significant coherences obtained from computing coherence for uv, $v\varsigma$ and $u\varsigma$ pairs. The word 'leads' means that the first variable leads the second variable by 90° with depth. In phase or out of phase relations are indicated by '(ip)' and '(op)', respectively. Two different phase relations are entered whenever the 95% error bars encompassed more than one phase value. Entries for $u\varsigma$ pair are the same for north and south casts, for reasons explained in the text.

$\vartheta(sm)$	1.25°S	0.5°S	0°	0.5°N	1.25°N
1400	u leads ς				u leads ς
933		u leads ς	u leads ς v,ς (op)	u leads ς v leads ς (op)	
700	u leads ς(op)		v leads ς u leads v(op)		u leads ς(op) v leads ς(op)
560			u,v (ip)	u,v (ip)	
467				v,ς (op)	
400	v leads u	ς leads u (ip)	ς leads u	ς leads u (ip)	v leads u (op)
350			ς leads u ς leads v		
311			ς leads u v leads u (ip)		u leads v (op)
280		ς leads u	ς leads v	ς leads u	
255	ς leads v	ς leads u	ς leads u v leads u (ip)	ς leads u v leads ς	
233		ς leads v	v leads u		
215			ς leads u	v leads u (op)	
200			ς leads u ς leads v		v,ς (ip)
187			ς leads u v leads ς		
175		ς leads u (ip) ς leads v	ς leads u v leads u (op)	ς leads u (ip)	

Table 4.1. (continuation)

$\vartheta(sm)$	1.25°S	0.5°S	0°	0.5°N	1.25°N
165			ς leads u v leads u		
156			ς leads u v leads u		ς leads v
147	ς, u (ip)		ς leads u v leads ς (ip)		ς, u (ip) v leads ς v leads u (op)
140		ς leads u	ς leads u	ς leads u	
133			ς, v (ip)	u, v (op)	
127			ς leads u	u, v (op)	u, v (op)
117		ς, v (ip)	ς leads u	v leads ς	
112	ς leads v				

are shown. The appearance of some consistent coherent pairs at some particular bands and latitudes is suggestive of the presence of equatorial waves in the records. These particular patterns revealed by the cross-spectral calculations will be interpreted in the following sections.

Besides looking at meridional energy scaling in comparison with theoretical predictions and cross-spectra phase relations between u, v and ς, time and zonally lagged coherences were also employed to reveal any long zonal decorrelation scales or any periodicity in time which might be hidden in the records. Unfortunately, the temporal coverage of our data set is deficient, as we have stressed before, and only very few time lags were available to carry out the coherence analysis. Also the most densely surveyed region was along the equator (almost half of the collected profiles). Thus, the calculations will rely heavily on equatorial or near equatorial casts. Since wave energy decays

84

away towards higher latitudes anyway, this is not a handicap but rather an advantage in our efforts.

If we consider for a moment what happens at (or very close to) the equator, each of the theoretical wave modes (Kelvin, Rossby and mixed Rossby-gravity) has its strongest signature in a different dynamical variable. Kelvin waves do not have any meridional velocity signal (at least in the most simple case of linear waves in a motionless basic state), and should only appear in the zonal velocity and vertical displacement records. Long Rossby waves also have strong zonal currents associated with them at the equator, but in contrast with Kelvin waves, they lack a significant vertical displacement signal at those latitudes. On the other hand, mixed Rossby-gravity waves have their energy mainly associated with meridional currents. Short Rossby and high frequency gravity modes are not important in our interpretation, on the basis of scales and dissipation arguments. From the above considerations, we might expect that analysis of meridional velocity records will most likely reveal any mixed Rossby-gravity possibly present in the PEQUOD data, while analysis of u and ς records will probably yield information on the occurrence of Kelvin and long Rossby modes.

Zonally lagged coherence results, obtained using the procedure previously outlined in section 3.2 and combining all data from the 3 cruises together, are presented in Table 4.2 for u, v and ς. Only significant coherence phases are shown, together with their 95% confidence error bars. Since Table 3.2 already contains the results for zonal velocity over the $700 - 280sm$ band, they are omitted here. A look at Table 4.2 reveals no consistent patterns of coherence over several zonal lags, in contrast with what was observed for the zonal velocity signal wavenumber bands. Most results seem to be sporadic, with some significant coherences occurring at large lags, but not at smaller lags. From statistical considerations only, we expect 5% of the coherence points to stand above the 95% zero confidence level anyway. Therefore, some of the entries in Table 4.2 are probably not

Table 4.2. Zonally lagged coherence phases, significant at the 95% confidence level, obtained as explained in the text. Positive (negative) phase means east casts lead (lag) west casts with depth.

a) Zonal velocity

LAGS	2.5°	5.25°	7.25°	9.75°
2800	9 ± 29		13 ± 48	
1400	-11 ± 74			22 ± 83
933	19 ± 33		-23 ± 53	
255	-22 ± 64			-42 ± 59
233		5 ± 33		25 ± 82
215		-14 ± 59		
175				-5 ± 86
156				-36 ± 28
140			102 ± 48	
117	-128 ± 62			

b) Meridional velocity

LAGS	2.5°	5.25°	7.25°	9.75°
700		156 ± 79	-148 ± 30	
467	40 ± 53			
255		-163 ± 69	151 ± 64	
133			98 ± 58	
117	130 ± 46			

c) Vertical displacement

LAGS	2.5°	5.25°	7.25°	9.75°
2800	-4 ± 40		25 ± 44	
700				-90 ± 74
467			-86 ± 55	
400	29 ± 44			
350	28 ± 56			
311	-4 ± 52			
280	-12 ± 43		-101 ± 55	
156			56 ± 79	
140		144 ± 85	97 ± 44	
133				49 ± 48

statistically significant. Our findings here also seem to underline the basic wide band nature of the wave spectra, perhaps more apparent for the meridional velocity case.

The search for periodic motions in time was pursued by computing time lagged coherences, in the same fashion used in section 3.3. The lags available within each cruise did not allow us to look at propagation on time scales of a few weeks. Time intervals between collection of casts at each site during the same cruise were invariably 5 or 6 days, providing essentially one time lag value. Here, we simply looked for phase propagation over scales of 1 year or so in both zonal and meridional velocities. Our findings are summarized in Table 4.3, where again we have omitted the results for vertical wavenumber bands already analysed in Chapter 3. We do not obtain any clear phase propagation consistently appearing for all the 3 lags available, except perhaps for the 933 sm vertical wavelength, in the zonal velocity records. In general, the time decorrelation scales seem to be short compared with a few months, especially for meridional velocity.

The results given here, concerning the latitudinal energy scaling of u, v and ς, their cross-spectral relations, and the respective time and zonal decorrelation scales, will be combined together in the next section, where we will look at each wavenumber band individually and attempt to trace any consistent pattern in the data.

Table 4.3. Significant time lagged coherence phases and their respective 95% error bars, obtained using the procedure explained in section 3.3. Time lags shown are 2 months (Feb 82/ April 82), 13 months (Jan 81/ Feb 82), and 15 months (Jan 81/ April 82). Positive (negative) phase means earlier casts lead (lag) later casts with depth.

a) Zonal velocity

$\vartheta(sm)$	LAGS		
	2	13	15
2800	139 ± 55	176 ± 23	-63 ± 34
1400	-26 ± 28		
933	49 ± 73	153 ± 37	175 ± 64
280			-33 ± 56
215		-8 ± 56	
156		163 ± 33	-157 ± 64
147			-157 ± 54

b) Meridional velocity

$\vartheta(sm)$	LAGS		
	2	13	15
1400	5 ± 43		
700		126 ± 51	
467			-56 ± 73
350	19 ± 50		
311			-85 ± 36
280	8 ± 65		
122			-98 ± 72

4.3 Evidence for equatorial waves in the PEQUOD records

The cross-spectral relations between u, v and ς summarized in Table 4.1 reveal some interesting results. If we take , for example, the 933 sm band, we find u leading ς by $\pi/2$ for casts taken at the equator and at 1/2 degrees off the equator. The reverse situation occurs for a significantly large number of vertical wavelengths ranging from 400 to 100 sm, with ς leading u by $\pi/2$ with depth. Before interpreting these findings in terms of linear equatorial waves, we first have to determine the predicted phase relations between the dynamical variables u, v and ς, for each of the different equatorial modes (Kelvin, Rossby and mixed Rossby-gravity).

4.3.1 Theoretical phase relations between u, v and ς

The linear theory reviewed in Appendix A, provides us with the polarization relations $(A.2)$ for u, v, p and w. A similar expression for the vertical displacement ς is trivially obtained by using (2.1) and $(A.1c, d)$. For the variables of interest here, we have

$$
\begin{bmatrix} u \\ v \\ \varsigma \end{bmatrix} = A_j e^{i(kx - \omega t)} \begin{bmatrix} U_j(\eta)G'(z) \\ iV_j(\eta)G'(z) \\ c_n^{-1}P_j(\eta)G(z) \end{bmatrix} \tag{4.1}
$$

where the notation is defined in Appendix A. It is easy (but sometimes a little confusing) to establish what the phase differences in depth are between each pair of variables, by inserting the appropriate functions U_j, V_j, P_j and G in (4.1), depending on whether we want to consider Kelvin, Rossby or mixed Rossby-gravity waves, either propagating or standing in the vertical.

As an example, let us look at the simplest case of the Kelvin wave, for which $j = -1$. Since $v = 0$, the only possible observable correlation is between u and ς. The meridional structure functions U_{-1} and P_{-1} are equal and take the form of a simple

exponential, as shown in Appendix A. If we consider the vertically propagating case (i.e., $G \sim e^{imz}$), then taking the real part in (4.1) yields

$$u \sim -m \sin mz, \quad \varsigma \sim c^{-1} \cos mz \tag{4.2}$$

with c being always positive for the Kelvin wave. The vertical structure of u and ς given by (4.2) implies that, independent of the sign of m, ς leads u by $\pi/2$ with depth. In other words, a vertical profile of ς has to be shifted downwards by one quarter of a wavelength to become in phase with a vertical profile of u. For the case of a standing mode in z (i.e., $G \sim \sin mz$), taking again the real part in (4.1) gives

$$u \sim m \cos mz, \quad \varsigma \sim c^{-1} \sin mz \tag{4.3}$$

implying the same relation between u and ς as for the propagating case. We thus can conclude that, regardless of whether we consider standing or propagating Kelvin waves, they will always show vertical displacement leading zonal velocity by $\pi/2$ with depth.

The corresponding phase relations between u, v and ς for the Rossby and mixed waves can be found in a similar fashion. They are in general more complicated than for the Kelvin wave, because all 3 variables attain non-zero values. Furthermore, the meridional functions U_j, V_j and P_j will not necessarily be equal, implying some sort of dependence of the phase relations on latitude. Table 4.4 tries to summarize all the theoretically predicted relations for each of the 3 wave modes mentioned. Only the pairs $u\varsigma$ and uv are presented, since information on the pair $v\varsigma$ can be trivially deduced from them.

Generally, the phase between u and ς only depends on the sign of c and is independent of whether we have vertically propagating or standing modes. The picture gets a little more fuzzy for the uv pair, where upward and downward propagation imply different phases between the two variables, and standing modes differ from propagating ones for the mixed wave. The meridional dependence of the phase relations is much

Table 4.4. Theoretical phase relations between u and ς, and u and v, for each of the equatorial waves [Kelvin (KW), Rossby (RW) and mixed Rossby-gravity (MRGW)]. VP and VS stand for vertically propagating and vertically standing waves, respectively. Other symbols used follow conventional notation, with c_z standing for vertical phase speed.

MODES	u/ς
KW	ς leads u by $\pi/2$ (VP, VS)
MRGW	ς leads u by $\pi/2$ for $c > 0$ (VP, VS) u leads ς by $\pi/2$ for $c < 0$ (VP, VS)
RW	u leads ς by $\pi/2$ for $c < 0$ (VP, VS) for $-y_c < y < y_c$, where y_c is first zero crossing

MODES	u/v
MRGW	u leads v by $\pi/2$ for $y > 0$, $c_z < 0$ (VP) u leads v by $\pi/2$ for $y < 0$, $c_z > 0$ (VP) v leads u by $\pi/2$ for $y > 0$, $c_z > 0$ (VP) v leads u by $\pi/2$ for $y < 0$, $c_z < 0$ (VP) u/v in or out of phase, depending on latitude and value of the phase factor $kx - \omega t$ (VS)
RW	u leads or lags v by $\pi/2$, depending on sign of $U_j V_j$ and c_z (VP) u leads or lags v by $\pi/2$, depending on sign of $U_j V_j$ and value of the phase factor $kx - \omega t$ (VS)

more complex, varying with the sign of the product $U_j V_j$. Since U_j and V_j have opposite symmetry (see Appendix A), phase relations are reversed across the equator. The phase factor $kx - \omega t$ also becomes important in determining the phase between u and v for standing modes. From what has been said, it is clear that $u\varsigma$ cross-spectral results are much less prone to ambiguous interpretation than the remaining pairs.

As Eriksen (1982) pointed out, a major conclusion which can be extracted from Table 4.4 is the strong implication of the sign of the phase between u and ς, on the direction of zonal propagation of energy, at the equator. If we exclude short Rossby waves from any major role in equatorial energy propagation, and recall that the mixed wave has a node in u and ς at $\eta = 0$, then for Kelvin waves propagating energy to the east, ς leads u by $\pi/2$ with depth, while for the long non-dispersive Rossby waves propagating energy to the west, u leads ς by $\pi/2$.

4.3.2 Interpreting each wavenumber band results

Although the search for evidence of equatorial waves in the records, based on the analysis performed in the previous section, may seem relatively easy, it closely resembles the task of solving a puzzle made up of imperfectly shaped pieces. It is, in that respect, a tricky and sometimes frustating job, but we shall proceed anyway, only considering those wavenumber bands which look more promising.

933 sm — Cross-spectral results depicted in Table 4.1 show that for the casts collected at the equator and 1/2 degrees off the equator, zonal velocity leads vertical displacement by $\pi/2$. As we have discussed before, this particular phase relation suggests the presence of long Rossby waves in the records, and westward energy propagation (see Table 4.4). This result does not exclude other wave types from being present at these wavenumbers,

but reveals the dominant contribution of Rossby waves to the zonal velocity and vertical displacement records.

Time lagged coherence calculations yielded significant amplitudes for the 933 sm wavelength at all three time lags available (Table 4.3). Interpretation of observed phases is at most ambiguous, as clearly depicted in Fig. 4.2. Either the existence of standing modes or downward phase propagating waves is consistent with the data. We may be tempted to estimate the period T, using the methods of Chapter 3, which would give

$$2 \text{ years} < T < 3.4 \text{ years} \tag{4.4}$$

However, we should emphasize the very questionable character of bounds given in (4.4). As we explained when discussing the deep jet signal, allowing for a finite bandwidth $\Delta\omega$ makes the interpretation of the time lagged coherence phases very uncertain. In this particular case, we have the additional possibility of aliasing, because of the relatively large phase error bars on the estimate at two months lag (Fig. 4.2). Therefore, the procedure of simply extracting a value of T by fitting a straight line through the three data points available, is hardly justifiable.

A look at zonally lagged coherence phases in Table 4.2, for the two bands under scrutiny, does not lead to any clear idea on the underlying east-west characteristic scales. Only zonal velocity results are relevant here. The hope of extracting any reasonable estimate of zonal wavelength from the coherence phases is not realized, because there is no consistent pattern over several zonal lags, at this wavenumber band. In addition, error bars are generally large. Therefore, the information revealed by zonally lagged coherence phases is basically useless in restricting our choice of temporal and spatial scales for the hypothetical Rossby waves present in the records.

Since equatorial flows are coherent at zero phase with flows observed 1/2 degrees away from the equator (see Fig. 3.1), it is probably true that the first meridional Rossby wave modes contribute strongly to the spectra. Without knowing T and k, the
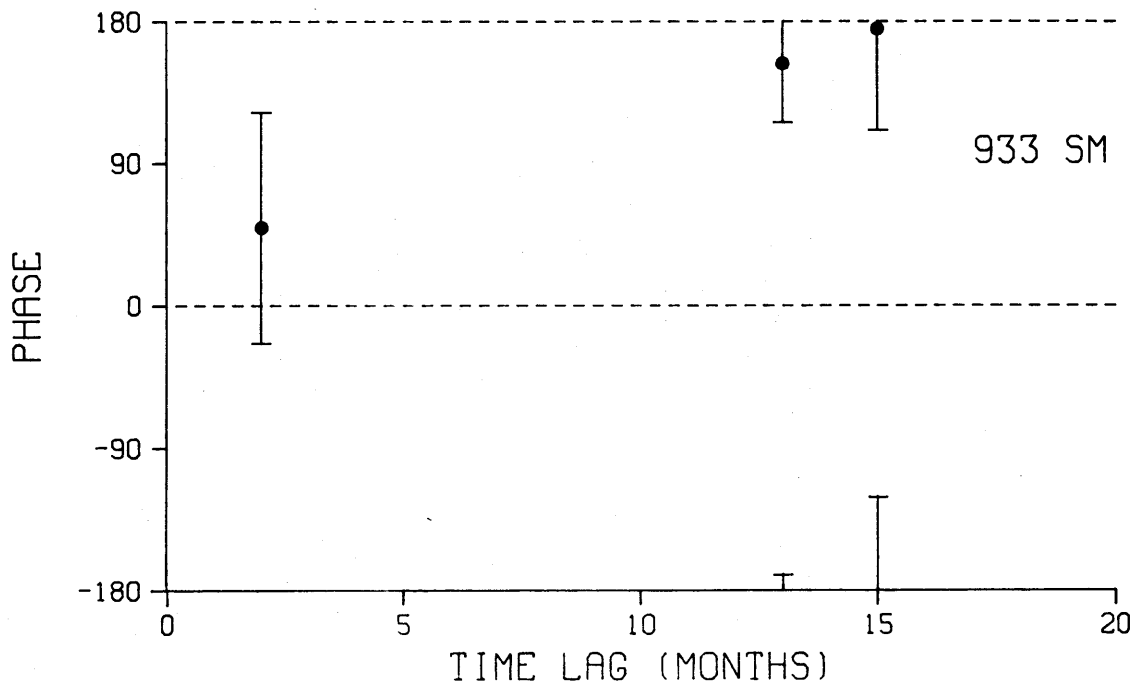
Fig. 4.2. Plot of coherence *vs.* time lag for vertical wavelength $\vartheta = 933sm$. 95% phase error bars are drawn at each point.

first zero crossing for a meridional mode can not be determined, nor for that matter can we define the latitudinal structure of the zonal kinetic energy associated with that mode. It suffices here to mention the general trapped nature of the energy in the 933 *sm* band, consistent with equatorial wave arguments.

Summarizing the findings for this band, Rossby waves seem to dominate the zonal velocity records, propagating energy to the west. Both vertically standing or propagating modes are possible. Time and space scales are not resolved from the data. No significant coherence between u and v occurs at off equatorial sites to corroborate Rossby wave hypothesis. A word of caution should be said concerning the validity of the WKBJ approximation at the low wavenumber range of the spectra. The vertical scales considered here are not necessarily small, compared with the scale of variation of buoyancy frequency, thus some level of suspicion should be kept about the soundness of the stretching and scaling procedure described in Chapter 2, for these larger wavelengths.

400-140 sm — Throughout this band, cross-spectral calculations show ς leading u by $\pi/2$ with depth, at the equator. Some wavenumbers show the same relation for casts 1/2 degrees off the equator. According to Table 4.4, this implies that Kelvin waves dominate the u and ς records, over this broad range of wavenumbers.

The bands considered here include the ones corresponding to the prominent deep jets. We may therefore ask whether the particular u and ς phase relations observed at 400–311 *sm* are primarily a manifestation of the Kelvin wave signature of the deep jets signal, or rather a reflection of the composition of the background spectra. I believe the latter is most likely the case, for several reasons. The calculation of vertical displacement profiles depends critically on how well the mean quantities δ and δ_p are known (see section 2.2). Due to the apparent long time scales of the jets compared with the time duration of the PEQUOD experiment, we do not expect their associated vertical

displacement fields, essentially given by $(\delta'^{-1} - \delta^{-1})/\delta_p$, to be well represented in the calculated profiles, simply because the data used to obtain δ and δ_p was not extensive enough in time to resolve those mean quantities. In addition to this fact (or perhaps as a consequence of it), ς power spectra do not exhibit the strong energetic peaks at 350–311 sm as observed in u power spectra, and zonally lagged coherence calculations for vertical displacement, shown in Table 4.2, imply much shorter decorrelation zonal scales then the ones found in the zonal velocity records. The rather broad band character of the Kelvin wave signature appearing in the cross-spectral calculations, together with the above considerations, lends some confidence to the assertion that the deep jets are not the major factor behind cross-spectral results at 400–311 sm wavelengths.

With a very few exceptions, which we will briefly examine below, time and zonally lagged coherence calculation show no relevant features (i.e., no time or zonal periodicity) over these bands. The underlying wave processes are most probably of a wide band nature (large $\Delta\omega$ and Δk).

Latitudinal energy scaling of zonal velocity and vertical displacement records, shown in Fig. 4.1, does not follow the predicted Kelvin wave scaling in general, except for the 350 sm wavelength where the deep jets are expected to play a major role in the calculations. The presence of Rossby waves in the records may be responsible for this broadening effect, even though Kelvin waves are still the strongest contributor to the zonal kinetic and potential energy, close to the equator. Calculations of symmetric and anti-symmetric zonal velocity power spectra for D, F, L and N casts, as discussed in section 3.1, showed equal symmetric and anti-symmetric power levels for $\vartheta < 280sm$, which in fact suggests the presence of Rossby waves of even meridional mode number in the records.

280 sm — A brief separate discussion is given for this wavelength, because besides the Kelvin wave signature implied by the phase relation between u and ς, this band

also shows significant coherences over $7°$ of longitude (Table 3.2). Lines of constant phase in the x-z plane slope downward toward the west, which for the case of Kelvin waves with eastward phase speeds, implies upward energy propagation. A very rough estimate of the zonal wavelength, based on zonally lagged coherences results, yields a value of $\lambda = 4000\,km$ ($\lambda_{min} \sim 2800\,km$). Time lagged coherences are not significant, but from estimate of k and Kelvin wave dispersion relation, we arrive at time scales of about 1 year. Despite the relatively long zonal decorrelation scales, we can not explain all the results at this band in terms of a single Kelvin wave mode. Several modes may be present, although Δk is probably narrower than at other adjacent wavenumbers.

The particular bands just discussed above gave the most clear hints for the presence of particular equatorial wave modes in the records. We could perhaps claim the occurrence of 3 coherent uv pairs over the band $133 - 127sm$ at $0.5°$N and $1.25°$N, as a manifestation of the existence of mixed Rossby-gravity waves (u and v are out of phase) at these vertical scales. There is also the case at $147\ sm$ where we find three coherent pairs ($u\varsigma$, $v\varsigma$ and uv) at the same place ($1.25°$N), with the internally consistent phase relations between u, v and ς suggestive of the presence of mixed Rossby-gravity waves. But the evidence supporting these arguments is certainly weak.

4.3.3 The occurrence of uv and $v\varsigma$ coherences at the equator

In the context of meridional modes used until now, only pairs of variables with the same meridional symmetry should show any coherence at the equator (e.g., U_j and P_j are symmetric, therefore they both attain non-zero values at $\eta = 0$; in contrast, U_j and V_j have opposite symmetries, hence one of them has a zero at the equator). The observations seem to contradict these inferences. Table 4.1 contains several uv and $v\varsigma$ coherent pairs found at the equator. The relatively large number of these pairs seems to rule out the possibility of attributing them to purely statistical effects (i.e., the pairs

amount to roughly 14% of the total number of possible coherent points, which is more than the 5% expected on statistical grounds).

Correlations between uv or $v\varsigma$ are generally related to meridional energy fluxes, associated with these wave fields. The normal meridional mode solutions to the wave equations, given in Appendix A, are not appropriate to look at energy propagation across the equator, simply because they imply standing modes in latitude. To rationalize the appearance of significant coherences between uv or $v\varsigma$ at the equator, it is better to try a different approach at solving the linear equatorial β-plane wave equations of Appendix A, as done by Blandford (1966) [see also Gill (1982)]. Instead of solving the system $(A.1)$ in terms of the usual Hermite functions, we assume the following form for the meridional structure of the solutions

$$V \sim A(y)e^{ily} \tag{4.5}$$

with $A' << lA$. This condition requires the phase of the wave to change much more rapidly in latitude than the amplitude modulation factor $A(y)$ of the wave packet. From $(A.1)$, the following expressions for U and P at $\eta = 0$, in terms of V, are easily obtained

$$U = -i\left(\frac{k\omega}{\omega^2 - c^2k^2}\right)V_y \tag{4.6a}$$

$$P = -i\left(\frac{\omega}{\omega^2 - c^2k^2}\right)V_y \tag{4.6b}$$

Given the relation

$$p_z \sim N^2\varsigma \tag{4.7}$$

between pressure and vertical displacement, we may use form (4.5) in expressions (4.6) to arrive at

$$U \sim \left(\frac{kl\omega}{\omega^2 - c^2 k^2} \right) V \qquad (4.8a)$$

$$\varsigma \sim i \left(\frac{m\omega}{\omega^2 - c^2 k^2} \right) V \qquad (4.8b)$$

These expressions imply that zonal and meridional velocities can be in or out of phase, depending on the sign of the factor $kl/(\omega^2 - c^2 k^2)$ in (4.8a), while meridional velocity can lead or lag vertical displacement by $\pi/2$, depending on the sign of the factor $m/(\omega^2 - c^2 k^2)$ in (4.8b).

The solutions derived above clearly bring out the possibility of having coherences occur between the pairs uv and $v\varsigma$ at the equator. A slightly more heuristic argument using several phase-locked meridional modes, can be given to justify the occurrence of phase relations differing from those implied by expressions (4.8). In this situation, we can imagine several coupled meridional modes giving rise to total nonzero u, v and ς fields at the equator, even though each individual mode would have a node for either u and ς or v at $\eta = 0$. Then, depending on their relative phases in z, we could have at the equator coherence between uv or $v\varsigma$ at *any* phase.

The coherent pairs found in Table 4.1 for uv and ςv, at the equator, do not show any particular pattern. If we interpret them in the broadest sense, they may be an indication of the general complex modal structure underlying the observations. They may also be the manifestation of cross equatorial energy fluxes, occurring as sporadic events over certain longitudes, which then translate into high coherence points appearing in the cross-spectral results of Table 4.1, calculated using all the data.

There is certainly a distinct event happening in April 82 at the Q site (see Fig. 2.1). Cross-spectra computed using only the casts collected at that site reveal significant coherences over a broad range of wavenumbers for both uv and $v\varsigma$ pairs, as shown in Fig. 4.3. In fact, if Q casts are not included in the cross-spectral calculations leading to Table
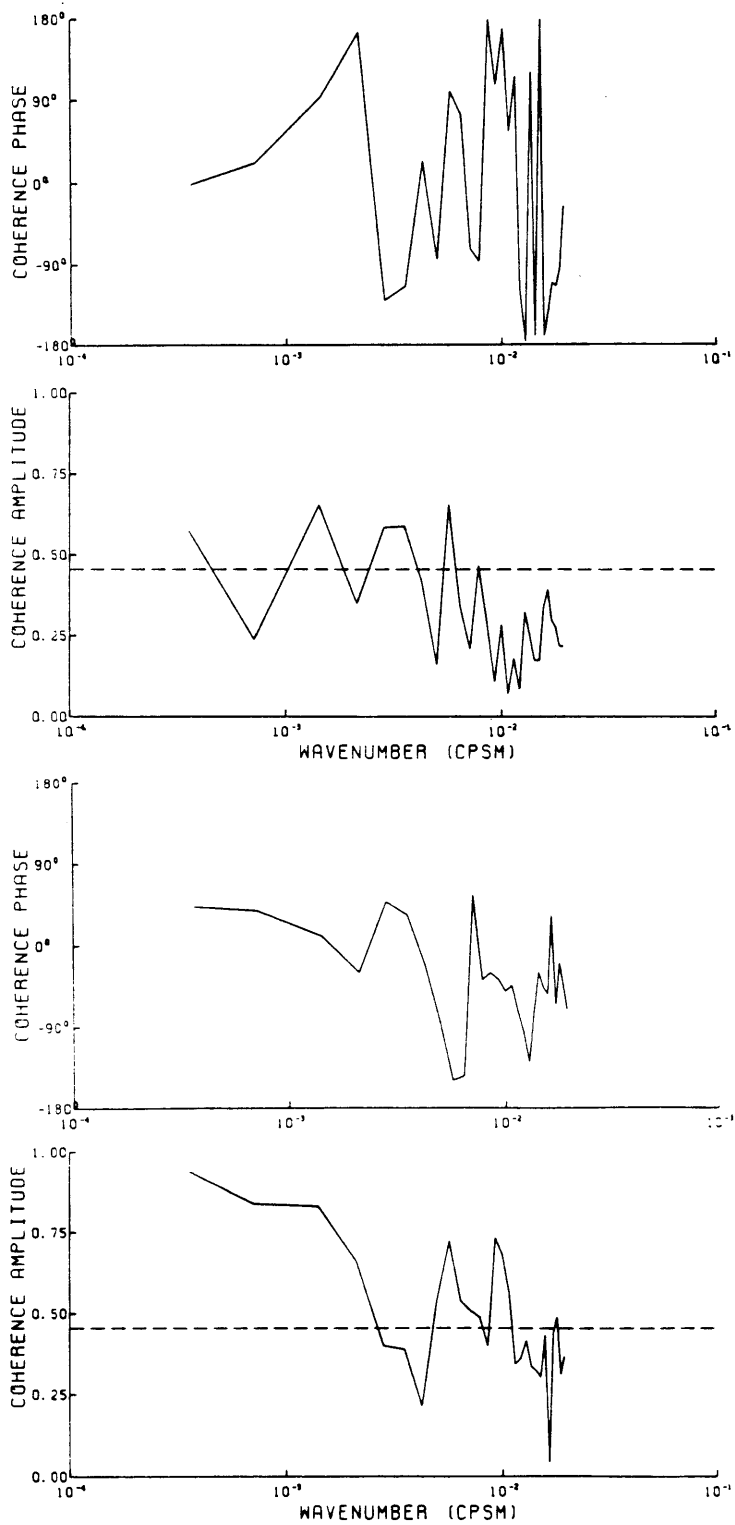
Fig. 4.3. Coherence amplitude and phase for the pairs $v\zeta$ (top panel) and uv (bottom panel), computed using all seven Q casts collected during the April 1982 cruise. Averaging over two adjacent wavenumber bands was done.

4.1, all of the coherent $v\varsigma$ pairs previously obtained disappear. Some of the uv pairs also go away. There are perhaps several different processes going on at this particular Q site, depending on the vertical scales considered. At long wavelengths $(\vartheta > 467\,sm)$, u and v are roughly in phase, while v leads ς by $\pi/2$. This may be the signature of some large vertical scale deep flow crossing the equator at these longitudes. In the remaining bands, the significant coherences seen for $v\varsigma$ calculations at 350–280 sm do not have a counterpart in the uv case, with the reverse situation happening for the band centered at 100 sm. The only other wavelength where both uv and $v\varsigma$ show significant coherence is 175 sm, with u and v roughly out of phase and v leading ς by 90°. At these vertical scales, we may have a wave packet propagating across the equator as discussed before.

Events such as the one happening at the Q site during April 82 may not be rare, but since they are rather localized in time and space, it is difficult to document them with the kind of data available to us here.

4.4 Comparison of our data with Eriksen's (1981) western Pacific data

Eriksen (1981) describes results obtained from the analysis of a data set very similar to ours. His observations consist of a series of vertical profiles of horizontal current and density, made within 5° of latitude of the equator at the 168° and 178°E meridians (western Pacific), and collected during May and June of 1978. Even though the spatial and temporal coverage of his records is much sparser than in the PEQUOD case, a comparison of the major findings in the two studies is probably worthwhile. Since the resolution of vertical scales in Eriksen's calculations was hampered by the necessary wavenumber band averaging done to improve the statistical reliability of his results, he was not able to isolate the deep jets as a powerful peak in his zonal velocity spectra, although they seem to be a prominent feature in his raw zonal velocity vertical profiles. Therefore, the scope of this comparison is not so much the deep jets and the zonal velocity signals which we were able to observe in the PEQUOD records, but rather has to do with the general structure of the current and vertical displacement fields in the deep equatorial Pacific, as inferred from the power levels, spectral shapes or cross-spectral characteristics of those fields.

In comparing power levels and spectral shapes between the two data sets, we have used spectra computed by both piece averaging all casts from the three cruises and band averaging over four adjacent wavenumbers, in order to decrease size of the error bars and better mimic Eriksen's calculations (he used band averaging over five adjacent wavenumbers). There is a slight difference between the values of N_0 used in stretching and scaling both records (in our case $N_0 = 0.1887 \times 10^{-2}s^{-1}$, while Eriksen has $N_0 = 0.175 \times 10^{-2}s^{-1}$), but we will not worry about its effect on this rough comparison, since it is a very small difference anyway.

Energy levels in both observations are generally similar, especially for zonal and meridional velocities. There is a slight tendency for higher levels in the PEQUOD records at short wavelengths ($\vartheta < 100\,sm$), but these vertical scales are suspect, on

the basis of what has been said in section 2.3. Vertical displacement power densities are consistently higher in the PEQUOD records by a factor of two or three, but any possible significance of this fact is downplayed by the amount of variance introduced in the inherently noisy calculation of ς profiles from the density data. In general both records show equatorial intensification for u and v, but less so for ς, especially at low vertical wavenumbers.

Spectra computed by Eriksen have a rough wavenumber dependence of the form m^{-2} or $m^{-2.5}$ (m is vertical wavenumber), with the steeper slopes more appropriate to the equatorial data. The PEQUOD velocity spectra tend in general to be a little less steep ($m^{-1.5}$ or m^{-2}), with the vertical displacement spectral shapes closer to a $m^{-2.5}$ or m^{-3} slope. In fact, ς spectra show steeper slopes than u and v spectra in both records.

Perhaps the most striking similarity between the two data sets is the strong evidence for the presence of Kelvin waves over the same wavenumber bands, as inferred from the cross-spectra of u and ς. Both studies find ς leading u by $\pi/2$ with depth, for a significant range of wavelengths ($\sim 400 - 100\,sm$ in our case, $\sim 800 - 100\,sm$ in Eriksen's data). Considering the fact that the two experiments took place four years apart and were carried out at locations separated by approximately 2000 km, our finding seems to confirm the idea that the Kelvin wave signature at these bands is an ubiquitous feature of the deep equatorial Pacific flows. In terms of the other cross-spectral results, Eriksen did not find any evidence for Rossby waves at long wavelengths, as we did here. The only other coherent pair he found was between u and v, suggestive of the presence of Rossby waves at 3°N. This and the remaining entries in Table 4.1 are not relevant here, since they may denote isolated events, rather than average oceanic conditions.

In his paper, Eriksen modeled the observations in terms of a spectral sum of various equatorial wave modes. He assumed that every meridional mode available for a

103

particular frequency and vertical wavenumber was equally forced. This was a sensible guess, given the virtually complete lack of information about the forcing functions generating the observed wave fields, not to mention the possible effects of topographic scattering and nonlinear interactions in exchanging energy among different wave modes. Although Eriksen's spectral approach is probably the most adequate way of modelling our records, we will refrain from attempting this. The amount of data we have is not enough to restrict the choice of the modal amplitudes more than Eriksen could by fitting the most robust observational results. We have seen how the PEQUOD records are qualitatively consistent with linear equatorial waves, thus there is no need to attempt a quantitative (but non-unique) spectral model, unless we were to believe that we could come up with an universal statistical description of the deep equatorial u, v and ς fields, as Garrett and Munk (1979) have done for internal waves at mid-latitudes. Although the crude comparison between Eriksen's data and the PEQUOD data revealed no major differences and even some unexpected similarities like the Kelvin wave signature over several wavenumber bands discussed before, the universality hypothesis is hardly a motivation for doing a spectral model if we do not have enough data, as it is the case here.

CHAPTER 5
Modelling Deep Equatorial Zonal Currents

The most important feature of the PEQUOD records analyzed in the previous chapters is the presence of strong deep zonal currents of short vertical scales. This chapter is a modest attempt at providing answers to some of the questions motivated by those findings. The idea is to try to explore the basic linear wave signature revealed by the data analysis, and see whether starting from this simple dynamical framework we can explain, for example, what is the mechanism responsible for setting the observed dominant vertical scales or what are the energy sources for these flows. These have been the outstanding issues since the discovery of deep equatorial jets, for which no definite answers have been given.

This chapter deals with two somewhat different modelling efforts. In Part I, we examine the general character of the response of a linear equatorial ocean to forcing associated with hypothetical deep energy sources located at eastern or western boundaries. Part II is dedicated in turn to investigate the influence of mean flows on linear Kelvin waves presumably forced at the base of the thermocline, below the equatorial Undercurrent. The reasons for pursuing such studies will be motivated as we go along. The two parts can be read separately without loss of continuity.

PART I. Response of an equatorial ocean to forcing at lateral boundaries

5.1 Introduction

The interpretation of EDJ in terms of linear equatorial waves has been advocated in the past (e.g., Wunsch, 1977; McCreary, 1984). Wunsch's model jets consist of long Rossby waves forced at the annual period by a surface vertical velocity pattern of a particular zonal wavenumber and unbounded in x. As pointed out later by McCreary (1984), for reasonably long time scales, equatorial waves propagate energy into the deep ocean at very shallow angles to the surface. Wunsch's ability to generate currents in the deep ocean was related to the infinite zonal extent of his forcing function. McCreary (1984) was able to inject considerable energy into the ocean's interior with a wind patch of finite zonal extent, by considering reflections at oceanic boundaries. However, the frictional losses which would probably occur during these processes and the need for several reflections before energy can reach the ocean bottom, make this energy transfer mechanism very inefficient. The nature of our observational results, presented in a previous chapter, attest for the extremely long time scales (longer than 1 year) associated with the EDJ. If these jets are really the manifestation of equatorial linear waves at such long periods, it seems then rather implausible that they have propagated down from the actively forced surface layers, as implied by these models.

As an alternative approach to this problem, we consider the hypothesis of having a *deep* energy source exciting the equatorial wave guide. In a recent development, Kawase (1987) used a shallow water model to study the linear response of the deep ocean to an off-equatorial mass source, located at the western boundary and mimicking deep water formation processes. His steady, moderately damped solutions exhibit strong equatorial zonal flows. Spin-up calculations illustrate how these flows are set up by equatorial Kelvin waves which connect to the coastal Kelvin waves carrying the signal

from the source to the equator, along the western boundary. More recent work by Kawase (private communication) using a modified version of Philander's numerical model corroborates his earlier findings. Some indication that these processes could be at work is found in the equatorial Atlantic tracer fields, especially in freons (Weiss *et al.*, 1985). The existence of deep western boundary currents has been documented (e.g., Warren, 1981) and although observations are scarce, these currents almost certainly fluctuate at interannual time scales, reflecting changes occurring at the source. These fluctuations would in turn drive a response in the equatorial region. It is the character of this response which we wish to model in very simple terms, in the next sections.

5.2 The model and its mathematical treatment

Consider a constant N, equatorial β-plane, flat bottom ocean, bounded by one meridional wall placed at $x = 0$ and extending to infinity to the west or east of this boundary, depending on whether we want to study the ocean response to eastern or western boundary forcing, respectively. We force our model ocean at the meridional wall with a time dependent zonal jet, confined to a certain depth and centered at the equator. In doing so, we choose not to address the details on how the forcing jet came to existence, but rather to concentrate our effort in learning about the character of the forced solutions.

We pick our boundary condition to be a half cosine in the vertical and exponentially decaying in latitude. In mathematical terms, expressing the time dependence as a Fourier transform, we have

$$u = \frac{1}{2\pi} \int_{-\infty}^{+\infty} \hat{U}_0(\omega) e^{i\omega t} d\omega \, \cos(m_0 z) e^{-\mu y^2} \qquad |z| \leq \frac{l}{2}$$

$$u = 0 \qquad |z| > \frac{l}{2} \tag{5.1}$$

with

$$m_0 = \frac{\pi}{l}$$

where $\hat{U}_0(\omega)$ is the Fourier transform, μ gives the latitudinal decay scale of the jet and l gives its vertical extent. Other simple forms could have been chosen, but this particular vertical structure was the most convenient when finding analytical solutions below. The forcing jet is centered at $z = 0$ (exactly at mid-depth) in our ocean with top and bottom boundaries at $z = \pm H/2$.

Forcing at lateral boundaries is significantly different than the more usual surface forcing, in which the zonal wavenumber spectrum is specified and the ocean picks the vertical scales accordingly. Wunsch (1977) was able to select a dominant vertical scale in his solutions by choosing a forcing function of a particular period and zonal wavelength. In our case, the forcing function is confined to a certain depth and has a well defined vertical wavenumber spectrum. It is thus not possible to fix the vertical scale of the response in a similar manner. Instead, the vertical extent l of the boundary jet will play a more significant role in selecting a basic scale for the response.

Before presenting the mathematical treatment of our model, we might also remark that the assumption of a zonal jet as the forcing seems the most reasonable, if we want to obtain solutions having strong zonal flows at the equator. A meridional jet would not be as effective in producing zonal motions in the equatorial band, which are primarily associated with Kelvin and long Rossby waves, although it might still excite short Rossby and Yanai waves.

5.2.1 Solutions for western boundary forcing

Consider the case where we place the forcing at the western wall. In low frequency limit studied here, only the Kelvin waves are effective carriers of energy eastward. Short Rossby waves also have eastward group velocities, but due to their short zonal scales we expect them to be dissipated rather quickly. They will not play any major role in the solutions, especially far away from the forcing region. In addition, the Kelvin and short Rossby modes are mutually orthogonal. Therefore, only Kelvin waves will be included in our model.

The zonal velocity signal and dispersion relation for the Kelvin wave were given in relations $(A.2)$, $(A.10)$ and $(A.11)$ in Appendix A. In general, we can express our forced solution as a sum of an infinite number of Kelvin wave vertical normal modes (e.g., McCreary, 1984), i.e.,

$$u = \frac{1}{2\pi} \sum_{n=1}^{\infty} A_n \int_{-\infty}^{+\infty} \hat{u}(\omega) e^{-i(kx-\omega t)} d\omega \, \exp - \left\{ \frac{\beta y^2}{2c_n} \right\} \cos \frac{N}{c_n} z \qquad (5.2)$$

where A_n is a constant, $\hat{u}(\omega)$ is the Fourier transform in time, k and ω are dimensional frequency and zonal wavenumber respectively, and c_n is given by

$$c_n = \frac{NH}{2n\pi} \qquad (5.3)$$

where H is the total ocean depth. The eigenvalues c_n are found by solving the vertical structure equation $(A.3)$ in Appendix A, subject to the boundary conditions $G = 0$ at $z = \pm H/2$. We do not include the barotropic mode $n = 0$ in the sum in (5.2), since it is not relevant when looking for jet-like flows.

To determine our forced solutions, one has to match expression (5.2) to the boundary condition (5.1) at $x = 0$ to find the coefficients A_n and the form of the Fourier transform $\hat{u}(\omega)$. The part of the forcing exciting the Kelvin wave is that which projects onto the basis functions $\exp(-\beta y^2/2c_n)$ (e.g., Ponte, 1986). To do this projection, we

first expand the forcing in (5.1) as a double sum over the complete set of vertical and meridional modes of Appendix A, but only retain the terms referring to meridional mode $j = 0$ because all the others are orthogonal to the Kelvin wave mode and therefore do not have any projection onto the solutions considered here. Then, by equating the expansion coefficients of the forcing to those of the solution (5.2) evaluated at $x = 0$, we arrive at

$$\hat{u}(\omega) = \hat{U}_0(\omega) \tag{5.4a}$$

$$A_n = \frac{2}{H} \cos\left(n\pi\frac{l}{H}\right) \frac{2m_0}{m_0{}^2 - (2n\pi/H)^2} \frac{\int\limits_{-\infty}^{+\infty} \exp-\{(\mu + \frac{\beta}{2c_n})y^2\}\, dy}{\int\limits_{-\infty}^{+\infty} \exp-\{\frac{\beta y^2}{c_n}\}\, dy} \tag{5.4b}$$

where we have used the orthogonality of the cosine functions. Evaluating the integrals over y in (5.4b) yields

$$\frac{\int\limits_{-\infty}^{+\infty} \exp-\{(\mu + \frac{\beta}{2c_n})y^2\}\, dy}{\int\limits_{-\infty}^{+\infty} \exp-\{\frac{\beta y^2}{c_n}\}\, dy} = \sqrt{\frac{2}{1 + 2\mu c_n/\beta}} \tag{5.5}$$

Thus, the coefficients A_n are given by

$$A_n = \cos\left(n\pi\frac{l}{H}\right) \frac{4m_0 H}{(Hm_0)^2 - (2n\pi)^2} \sqrt{\frac{2}{1 + 2\mu c_n/\beta}} \tag{5.6}$$

The above expression implies that $A_n \sim n^{-2}$. This is helpful when we numerically evaluate the sum over vertical modes in (5.2), assuring for rapid convergence of the solutions. Notice that there is no singularity occurring for $m_0 H = 2\pi n$, since for such n the cosine term also goes to zero and the limit turns out to be finite.

The effect of linear friction on these solutions can be easily accomodated by letting the Kelvin wave dispersion relation become

$$\omega = c_n k - ir \tag{5.7}$$

110

where r is a friction coefficient. This is equivalent to having Rayleigh friction terms as well as Newtonian cooling in the Kelvin wave equations, with the additional assumption of these coefficients being equal (see McCreary, 1985). Our solutions are then modified by the inclusion of an exponential term of the form

$$\exp - \left\{ \frac{r}{c_n} x \right\}$$

in (5.2), which simply results from solving the dispersion relation (5.7) for k and substituting it in (5.2). Each vertical mode will decay in x, as it propagates away from the forcing region. High modes travel slower, therefore they will not penetrate as far into the interior as lower modes, before being dissipated. The decay scale c_n/r decreases linearly with mode number n.

This effect will be more pronounced for the case of Laplacian friction (i.e., frictional operator of the type ∂_{zz}), which can be solved just as easily for a constant N ocean as we have assumed here. The appropriate dispersion relation is then

$$\omega = c_n k - i\nu \left(\frac{N}{c_n} \right)^2 \tag{5.8}$$

with ν being the frictional coefficient. The e-folding zonal decay scale goes as c_n^3, rather than c_n as for the linear friction case, therefore the dependence on mode number is much stronger.

5.2.2 Solutions for eastern boundary forcing

We now study the case where a forcing jet is present at the eastern wall. Long Rossby waves play the same dominant role as Kelvin waves in the previous section, since they are the only waves available to carry energy westward away from the source, at low frequencies. We might be concerned about the possibility of poleward propagating coastal Kelvin waves leaking energy away from the equatorial waveguide, but again these waves only have meridional flows associated with them and therefore would not be forced very efficiently by our oscillatory zonal jet.

Although long Rossby waves have a meridional as well as a zonal velocity signal, for our purposes we need only consider the latter. The general form for this signal is given by expressions $(A.2)$ and $(A.8b)$ and the proper dispersion relation (3.2) has been used in Chapter 3. If we use (3.2) in $(A.8b)$, we can easily arrive at the following expression

$$u = \frac{1}{2\pi} \sum_{n=1}^{\infty} \sum_{j=1}^{\infty} A_{n,j} \int_{-\infty}^{+\infty} \hat{u}(\omega) e^{-i(kx-\omega t)} d\omega \, \cos \frac{N}{c_n} z \left[\frac{\psi_{j-1}}{\sqrt{2j}} - \frac{\psi_{j+1}}{\sqrt{2(j+1)}} \right] \quad (5.9)$$

Our solutions consist of a double sum over vertical and meridional mode number. The latitudinal structure of long Rossby waves is more complicated than the Kelvin wave simple exponential form, involving in addition various nodes and phase shifts according to the actual mode number j (see Figure 3.6 for an illustrative example).

To determine the forced response, we again expand the forcing (5.1) as a double sum over the complete set of vertical and meridional modes of Appendix A and solve for the constants $A_{n,j}$ by matching (5.9) to the boundary condition at $x = 0$, just as previously done for the Kelvin wave solutions. Using the orthonormality of the Hermite functions, this procedure yields

$$\hat{u}(\omega) = \hat{U}_0(\omega) \quad (5.10a)$$

$$\sum_{j=1}^{\infty} A_{n,j} \left[\frac{\psi_{j-1}}{\sqrt{2j}} - \frac{\psi_{j+1}}{\sqrt{2(j+1)}} \right] = B_n \sum_{j=1}^{\infty} \psi_j \int_{-\infty}^{+\infty} \exp - \left\{ \left(\frac{\mu c_n}{\beta} \right) \eta^2 \right\} \psi_j(\eta) \, d\eta \quad (5.10b)$$

where B_n is given by

$$B_n = \cos\left(n\pi \frac{l}{H} \right) \frac{4m_0 H}{H{m_0}^2 - (2n\pi)^2} \quad (5.11)$$

and the nondimensionalization $(A.4)$ was used to express the integral in terms of the nondimensional variable η. Our forcing function $\exp -\{\mu y^2\}$ is even in y. Therefore only Hermite functions of even j will be part of the expansion. If we take this into consideration and equate coefficients in $(5.10b)$, we obtain

$$\frac{1}{\sqrt{2}} \left[\frac{A_{2m+1}}{\sqrt{2m+1}} - \frac{A_{2m-1}}{\sqrt{2m}} \right] = B \int_{-\infty}^{+\infty} \exp - \left\{ \left(\frac{\mu c_n}{\beta} \right) \eta^2 \right\} \psi_{2m}(\eta) \, d\eta \quad (5.12)$$

for $m = 1, 2, ...$, where for simplicity we have dropped the subscript n pertaining to the vertical mode number under consideration (the only subscript refers to meridional mode number). Similarly, for the special case of $m = 0$, one easily arrives at

$$\frac{A_1}{\sqrt{2}} = B \int_{-\infty}^{+\infty} \exp - \left\{ \left(\frac{\mu c_n}{\beta} \right) \eta^2 \right\} \psi_0(\eta) \, d\eta \quad (5.13)$$

The integrals on the right of expressions (5.12) and (5.13) can be evaluated with the help of a table of integrals (Gradshteyn and Ryzhik, 1965). We then have

$$\frac{A_1}{\sqrt{2}} = B\pi^{1/4} \left(q + \frac{1}{2} \right)^{-1/2} \quad (5.14a)$$

$$\frac{1}{\sqrt{2}} \left[\frac{A_{2m+1}}{\sqrt{2m+1}} - \frac{A_{2m-1}}{\sqrt{2m}} \right] = B \frac{(\sqrt{\pi}(2m)!)^{1/2}}{2^m m!} \left(q + \frac{1}{2} \right)^{-1/2} \left(\frac{1/2 - q}{1/2 + q} \right)^m \quad (5.14b)$$

for $m = 1, 2, ...$ and with $q = \mu c_n/\beta$. Finally, putting $2m + 1 = j$ in $(5.14b)$ leads to the following recursion relation for the coefficients A_j

$$\frac{A_j}{\sqrt{2}} = B \frac{(\sqrt{\pi} j!)^{1/2}}{2^{\frac{j-1}{2}} \left(\frac{j-1}{2} \right)!} \left(q + \frac{1}{2} \right)^{-1/2} \left(\frac{1/2 - q}{1/2 + q} \right)^{\frac{j-1}{2}} + \sqrt{\frac{j}{2(j-1)}} A_{j-2} \quad (5.15)$$

113

for $j = 3, 5, 7, ..., 2m + 1$. Only odd j's will enter when actually computing the sums in (5.9).

The introduction of dissipation in our Rossby wave solutions is again done by letting the dispersion relation (3.2) become

$$\omega = -\frac{c_n k}{2j + 1} - ir \tag{5.16}$$

for the case of Rayleigh friction. Solutions will have an extra exponential decay term of the form

$$\exp - \left\{ \frac{r}{c_n} (2j + 1) x \right\}$$

The zonal decay scale still decreases with vertical mode number n, just as we had for the Kelvin wave case, but now there is an additional strong dependence on meridional mode number j as well. In general, the higher meridional modes have slower zonal group speeds, therefore they are more closely trapped to the forcing region located at the eastern boundary. The inclusion of small linear dissipation in the solutions (5.9) will thus insure that the sums over vertical and meridional modes will converge for finite n and j. This improvement in the convergence rate will be more significant for solutions computed farther away from $x = 0$.

5.3 Solutions with periodic forcing

In this section, the response of the model to periodic forcing in time is studied. We assume the forcing boundary jet to oscillate at a particular frequency, in which case the Fourier transform $\hat{U}_0(\omega)$ in (5.1) is a Dirac delta function and the time dependence of the forcing takes the simple $\cos \omega t$ form. The Kelvin wave solution (5.2) becomes

$$u = U_0 \sum_{n=1}^{\infty} A_n \cos(kx - \omega t) \exp - \left\{ \frac{\beta y^2}{2c_n} \right\} \cos \frac{N}{c_n} z \qquad (5.17)$$

while the Rossby wave solution (5.9) becomes

$$u = U_0 \sum_{n=1}^{\infty} \sum_{j=1}^{\infty} A_{n,j} \cos(kx - \omega t) \cos \frac{N}{c_n} z \left[\frac{\psi_{j-1}}{\sqrt{2j}} - \frac{\psi_{j+1}}{\sqrt{2(j+1)}} \right] \qquad (5.18)$$

with the coefficients A_n and $A_{n,j}$ still given by (5.6) and (5.14) respectively. Here, U_0 is the amplitude of the forcing.

Before calculating any solutions, we choose the following values for the various parameters appearing in our model:

$$H = 3500 \, m \qquad (5.19a)$$

$$l = 200 \, m \qquad (5.19b)$$

$$\mu = 1.6 \times 10^{-10} \, m^{-2} \qquad (5.19c)$$

$$U_0 = 10 \, cm/s \qquad (5.19d)$$

$$T = \frac{2\pi}{\omega} = 4 \, yr \qquad (5.19e)$$

$$N = 2 \times 10^{-3} \, s^{-1} \qquad (5.19f)$$

Our mid-depth forcing jet has a maximum amplitude of 10 cm/s, oscillates at a period of 4 years and extends over 200 m in the vertical. The latitudinal e-folding decay scale was chosen to be 80 km. These values are more or less arbitrary, since knowledge about the forcing boundary processes we are trying to model here is scarce at best,

but they seem like reasonable choices. The rather long forcing period is intended to mimic interannual variability of processes such as deep water formation, and to replicate roughly the time scales observed in the data, at the 350 *sm* and 560 *sm* bands. The buoyancy frequency value represents approximately the observed average value in our data. The basic character of our solutions will not depend critically on the choices of values just made, as we shall see later.

5.3.1 The Kelvin wave response

Let us first examine the nature of our model's response to western boundary forcing, which was treated in subsection 5.2.1. Solutions given by (5.17) and (5.6) were evaluated numerically, by summing the first 50 vertical modes (i.e., only modes with $n \leq 50$ were retained when calculating the sum in (5.17)). This number was sufficicient to assure convergence of our solutions. Unless otherwise stated, all pictures presented here relate to solutions calculated with no friction.

Figure 5.1 shows contours of zonal velocity signal in the y-z plane, at a distance of 5000 km from the western boundary located at $x = 0$. The structure of the flow is dominated by two main eastward jet-like features centered on the equator at depths of roughly $\pm$ 125 m, with maximum amplitudes of about 4 cm/s. No energy is seen in the remaining part of the water column. In addition, currents are strongly trapped to the equator, with decay scales more or less equal to the meridional structure of the forcing. If we look further eastward ($x = 10000\,km$), the same basic pattern is observed (see Figure 5.2), but now the two main jets appear further away from $z = 0$, lying at depths of $\pm 250\,m$. The vertical scale of these currents is roughly 200 m, in fact equal to the vertical extent of the forcing. Another minor difference between the two figures is the absence of any significant flows in between the two main jets, for the solution at $x = 10000\,km$ (Figure 5.2), while closer to the source at $x = 5000\,km$ (Figure 5.1), there are weak westward flows.
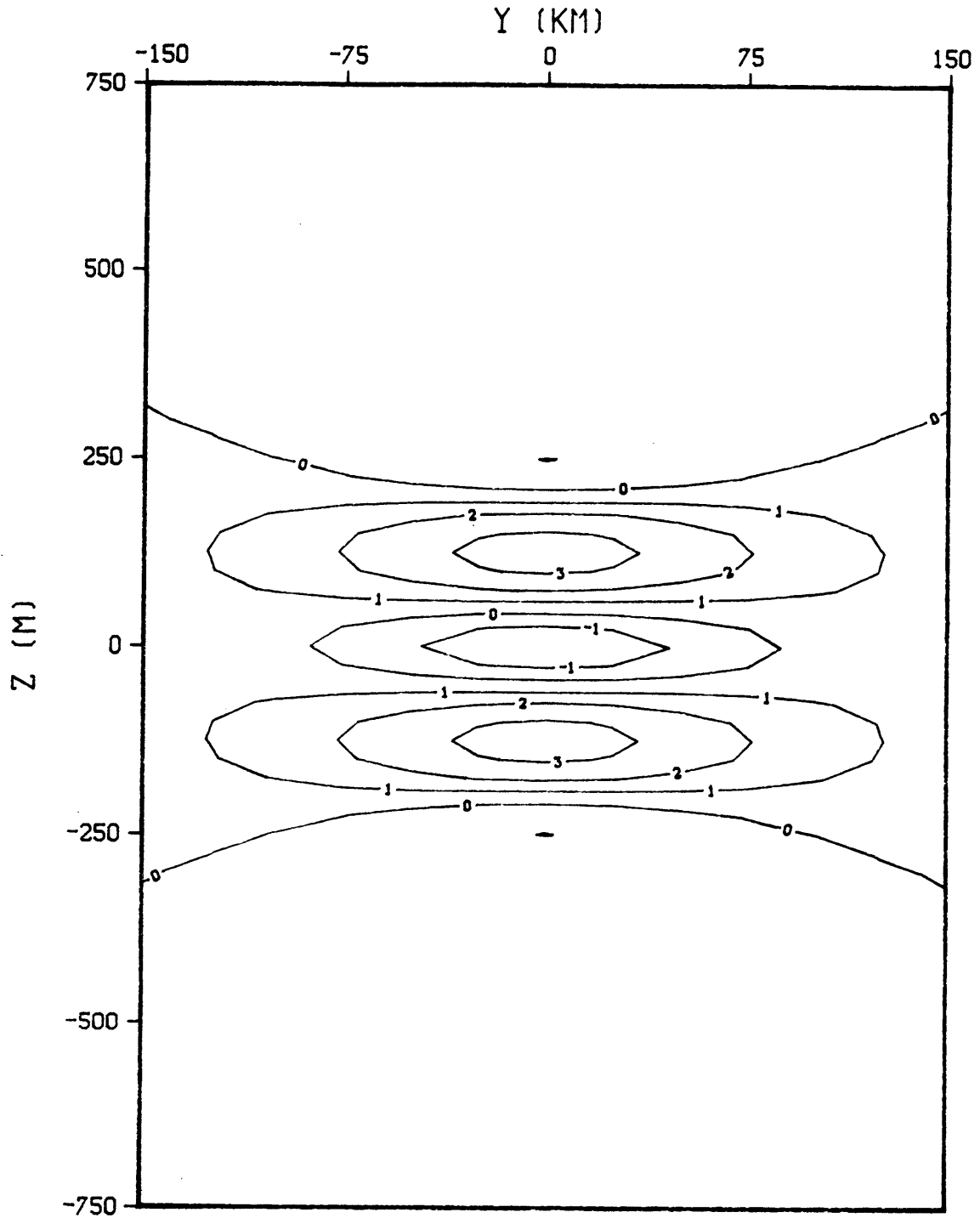
116

Fig 5.1. Zonal velocity contours in the y-z plane, computed at $x = 5000\,km$. Contour values are in cm/s. Our forcing jet was placed at $x = 0$ and centered at $z = 0$. Since only significant flows occur within 400 m of $z = 0$, the vertical coordinate in the plot does not reflect the full depth of the ocean ($H = 3500\,m$).
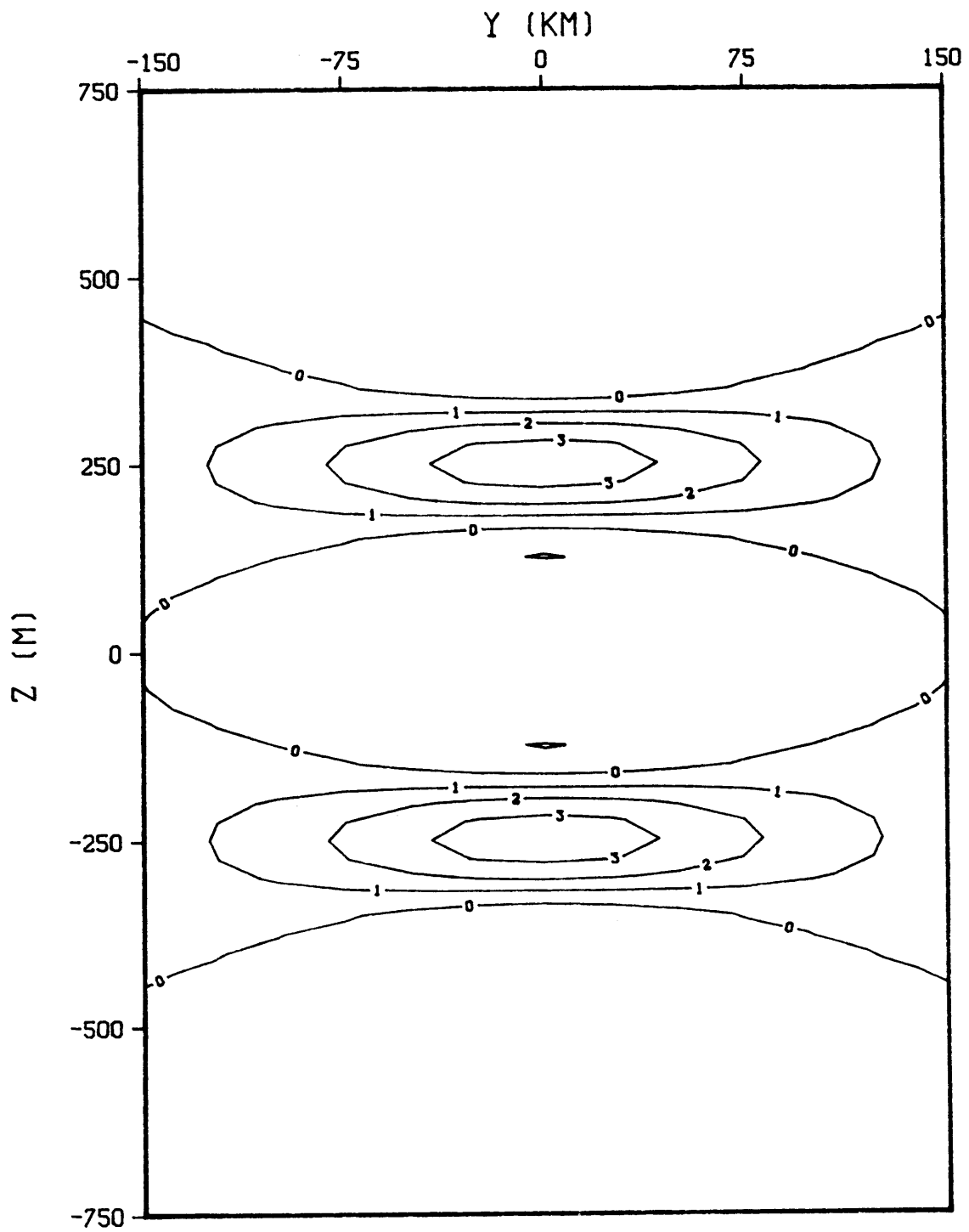
117

Fig 5.2. As in Figure 5.1, but for solutions computed at $x = 10000\,km$.

Solutions documented in Figures 5.1 and 5.2 can be rationalized in terms of very simple equatorial wave arguments. Our model's response consists of eastward propagating Kelvin waves, carrying energy from the western boundary along ray paths whose slopes with the horizontal are given by $\pm\omega/N$ (see, e.g., McCreary,1985), the ratio of the wave frequency to the buoyancy frequency. For our case of periodic forcing placed at mid-depth, energy can travel along two separate ray paths which diverge away from the source at very shallow angles due to the extremely low frequency chosen in (5.19e). In fact, if one computes the actual depths the two rays emanating from $z = 0$ would attain at $x = 5000\,km$ and $x = 10000\,km$, we find them to coincide with the depths at which the peak velocities in Figures 5.1 and 5.2 are observed. Therefore, the two main jets in those pictures consist of Kelvin wave packets in vertical and zonal wavenumber, which essentially replicate along two well defined ray trajectories the forcing signal present at $x = 0$.

To illustrate the validity of the simple interpretation just presented, we have plotted in Figure 5.3 zonal velocity contours in the x-z plane. The two main paths of energy propagation are clearly indicated in the picture, which resembles in some aspects the equatorial beam-like solutions obtained by McCreary (1984) in a slightly different context. Notice that clear separation of the upward and downward going rays only occurs somewhat east of the forcing region, due to the extremely small slopes associated with them. Close to the western boundary, these two rays overlap giving a region with velocities on the order of $7\,cm/s$. At a distance of 4000 km away from the source, they become separate features in the flow field.

The two Kelvin wave packets present in the solutions shown in Figures 5.1-5.3 carry energy in opposite directions in the vertical. Therefore, the upward (downward) going packet has positive (negative) vertical group velocity associated with it. Linear equatorial theory then implies that vertical phase speeds be in the opposite sense, i.e., downward (upward) vertical phase propagation should occur across the upward
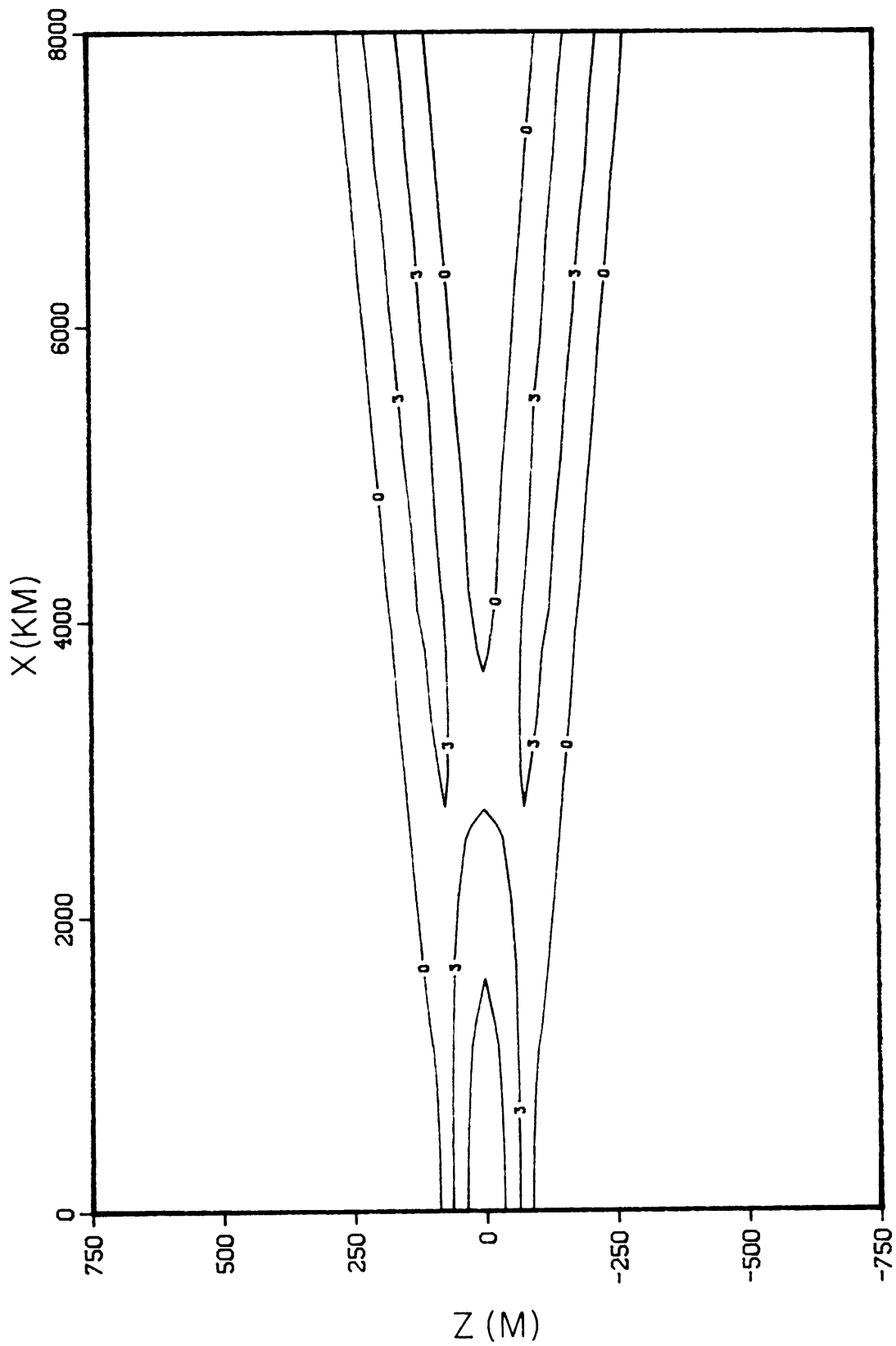
119

Fig. 5.3. Zonal velocity contours in the x-z plane. The contouring interval was 3 cm/s. The strongest currents occur near the forcing region where the two energy rays overlap. Towards the east, these rays diverge and become distinct.

(downward) going energy beam. This is indeed what happens in the solutions, as indicated in Figure 5.4, which shows a time sequence over approximately 2 years (1/2 of the forcing period) of vertical profiles of zonal velocity, obtained on the equator at $x = 6000\,km$. Figure 5.4 is a perfect illustration of how phase propagation occurs in a wave packet. If we take for example the upper energy ray, as time goes on we basically see the gradual appearance of a new westward jet, which emerges from the upper edge of the packet and propagates downward increasing in amplitude, while the strong eastward jet, which is present at the first time step in the sequence, slowly migrates down and decays in amplitude as it disappears on the lower edge of the packet. Another relevant detail in Figure 5.4 is the apparent standing oscillation pattern underlying the evolution of the flow present between the Kelvin wave packets (i.e., in the vicinity of $z = 0$). The energy seen in these weaker currents travel along rays which emanate from off-center points in the source and cross each other over depths $\mid z \mid < 100\,m$. Therefore, close to $z = 0$ there is no vertical propagation of energy and we mainly end up with the standing oscillation pattern noticed in Figure 5.4.

The maximum amplitudes attained by the main jets in these solutions are smaller than that of the forcing jet $(U_0 = 10\,cm/s)$ reflecting in part the dispersion of the energy available at the source between two diverging ray paths. In addition, amplitudes depend on how well the meridional structure of the forcing projects on each vertical Kelvin mode making up the solutions. If we computed a vertical wavenumber spectrum of the forcing (5.1), we would find most of the energy at the low wavenumbers. Thus, the amplitude of the solutions generally depends on how strongly we can force these large vertical scales. The projection integrals in (5.5) suggest that the shorter the meridional extent of the forcing jet (i.e., the larger the value of μ), the smaller the amplitudes of the response, simply because the low vertical modes are less strongly excited. In this respect, the most efficient latitudinal shape for the forcing would be a constant in y [i.e., $\mu = 0$ in (5.5)], in which case all vertical modes would project
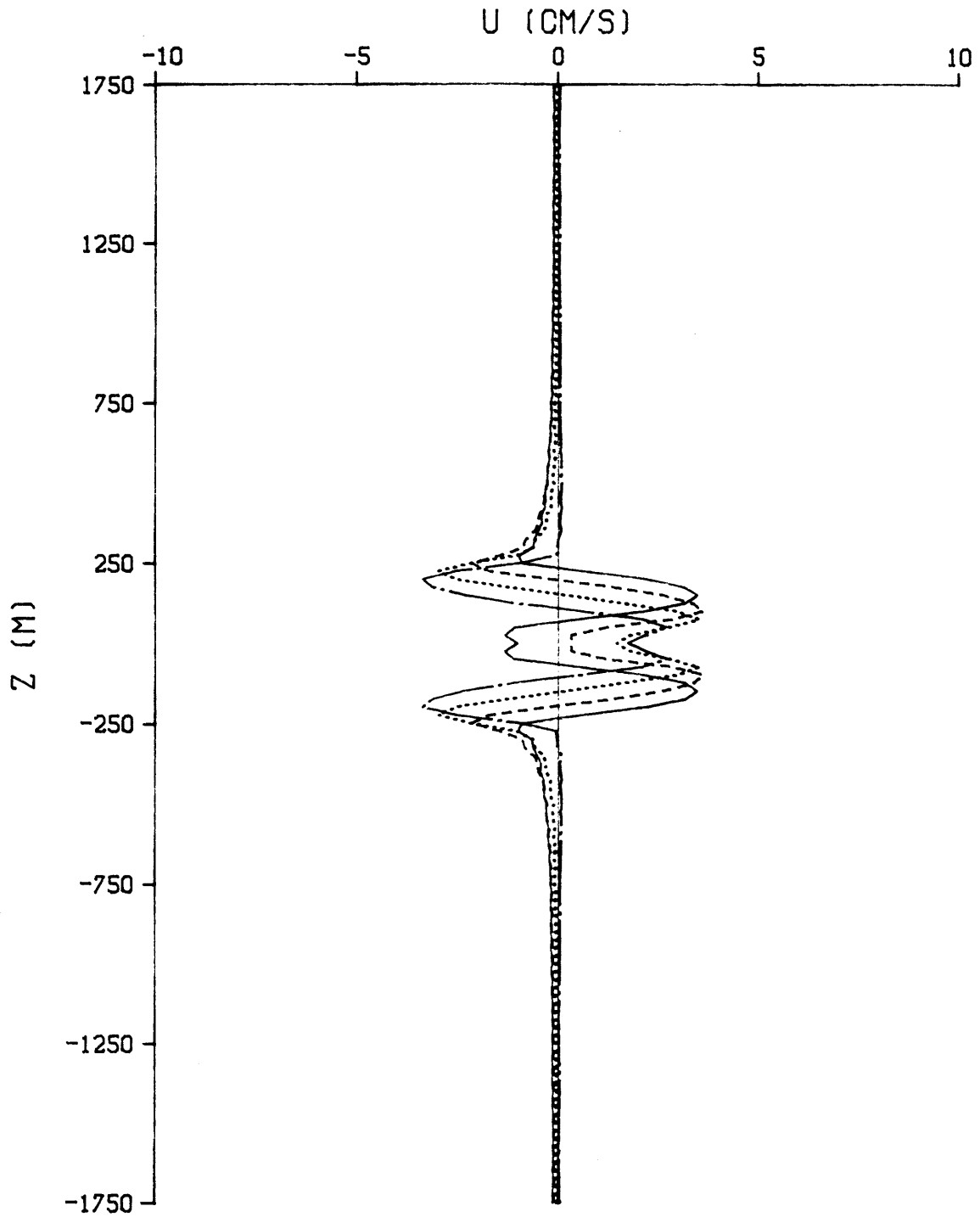
Fig. 5.4. Time sequence of zonal velocity profiles obtained at $y = 0$ and $x = 6000\,km$ [solid $(t = 0)$, dashed $(t = 6$ months), dotted $(t = 1$ year) and chaindotted $(t = 18$ months)].

equally well on the forcing, with the result (5.5) being independent of mode number n. These considerations are important in understanding what controls the magnitude of the forced solutions.

Frictional processes will also affect the amplitudes of the response, according to the considerations made at the end of subsection 5.2.1. Figure 5.5 shows the effect of including linear friction in the solution of Figure 5.3, with a spin down time of 4 years. Overall, the amplitudes are slightly lower than in Fig. 5.3, with peak values along the main two jets on the order of 3 cm/s as compared to 4 cm/s in the frictionless solutions. For $r = 1/4 \, yr^{-1}$, the zonal decay scales r/c_n given in 5.2.1 are very large, especially for the lowest vertical modes which have the faster zonal phase and group speeds (e.g., for $n = 10$, the decay scale is 14000 km). This explains why the maximum amplitudes decay so slowly to the east in Fig. 5.5. Since friction is more efficient in dissipating high vertical modes, some broadening of vertical scales should occur as the Kelvin wave packets propagate to the east. However, Fig. 5.5 does not show any sizable broadening because of the very small effects of friction on this particular solution.
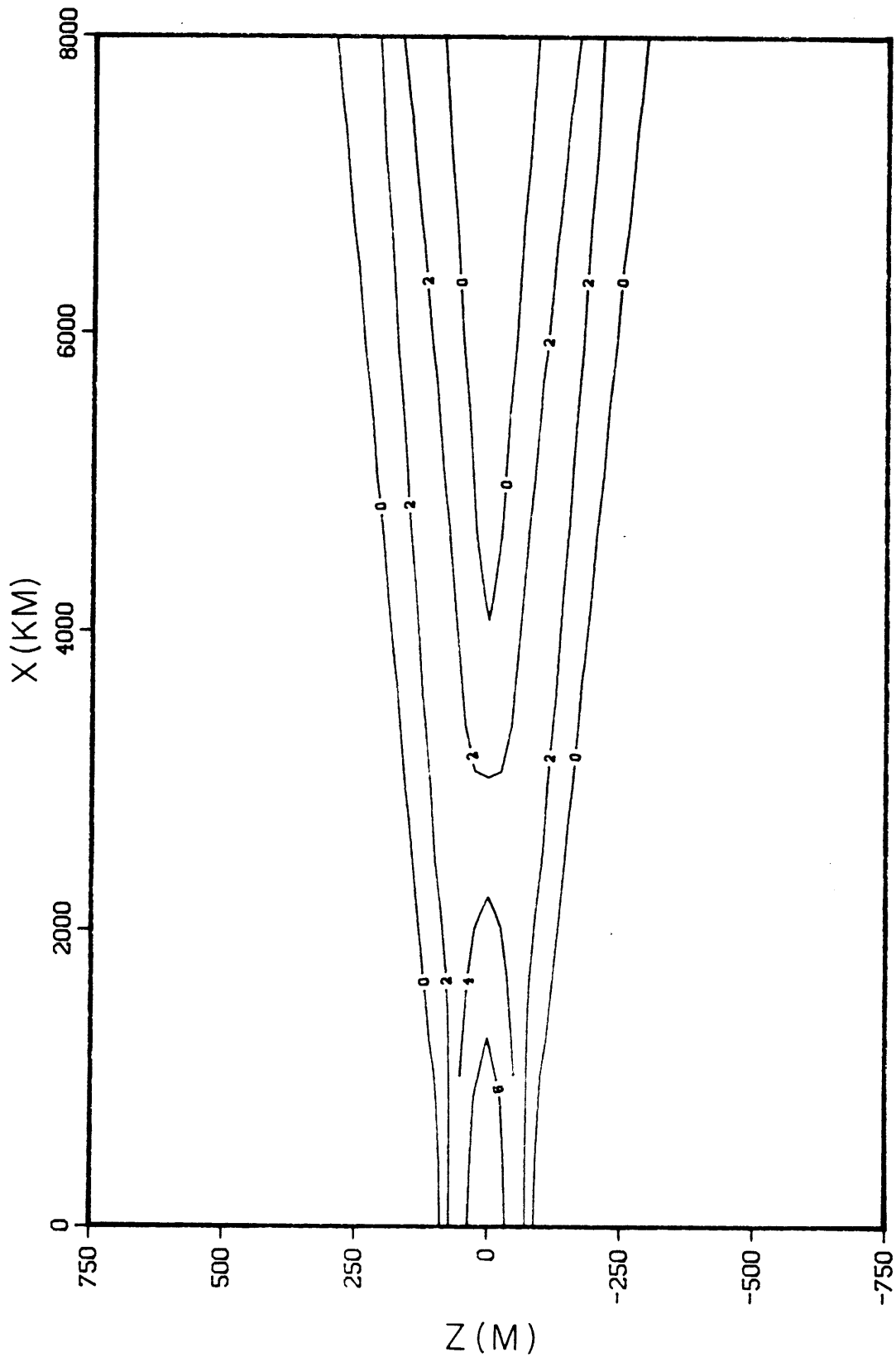
Fig. 5.5. Zonal velocity contours on the x-z plane obtained from solutions with linear friction. Spin down time used was 4 years. The contouring interval is 2 cm/s. Compare with the frictionless solution in Fig. 5.3.

5.3.2 The long Rossby wave response

We now turn our attention to the response of the model to eastern periodic boundary forcing. Much of the insight gained in studying the previous Kelvin wave solutions is helpful in anticipating what the long Rossby wave response will be when we put the oscillating zonal jet at the eastern wall. Again energy will propagate along rays, but now even for periodic forcing, an infinite number of ray paths are possible with slopes given by

$$\pm \frac{\omega}{N}(2j + 1)$$

Each meridional mode propagates energy at different angles to the horizontal, with the steepest paths occurring for the highest modes. We might expect then surface and bottom reflections to play a more important role in these solutions than in the previous section, where the very small slopes prevented the rays from hitting the top and bottom ocean boundaries within reasonable distances from $x = 0$. Friction will also have a more significant role in shaping the form of solutions since it will affect each of these rays and its reflections differently, as discussed at the end of subsection 5.2.2. All these points will be clearly illustrated when we examine some actual solutions below.

The sums over meridional and vertical modes in the mathematical solutions defined by (5.18) and (5.14) were evaluated numerically. Unless otherwise stated, we carried the summation to $n = 50$ and $j = 69$, with only odd j's entering in the calculations. Therefore only 35 meridional modes will be part of the computed solutions. Figures 5.6a and 5.6b show vertical profiles of zonal velocity at the equator for a distance of 3000 km and 4000 km west of the forcing, respectively, and calculated for the case of no friction (i.e., $r = 0$). The vertical structure of these flows is much different than those of the Kelvin wave flows of the previous section, with several jets now clearly visible throughout the water column. Energy is not confined closely to the depth at which the source is located, but rather it spreads out much more rapidly to fill
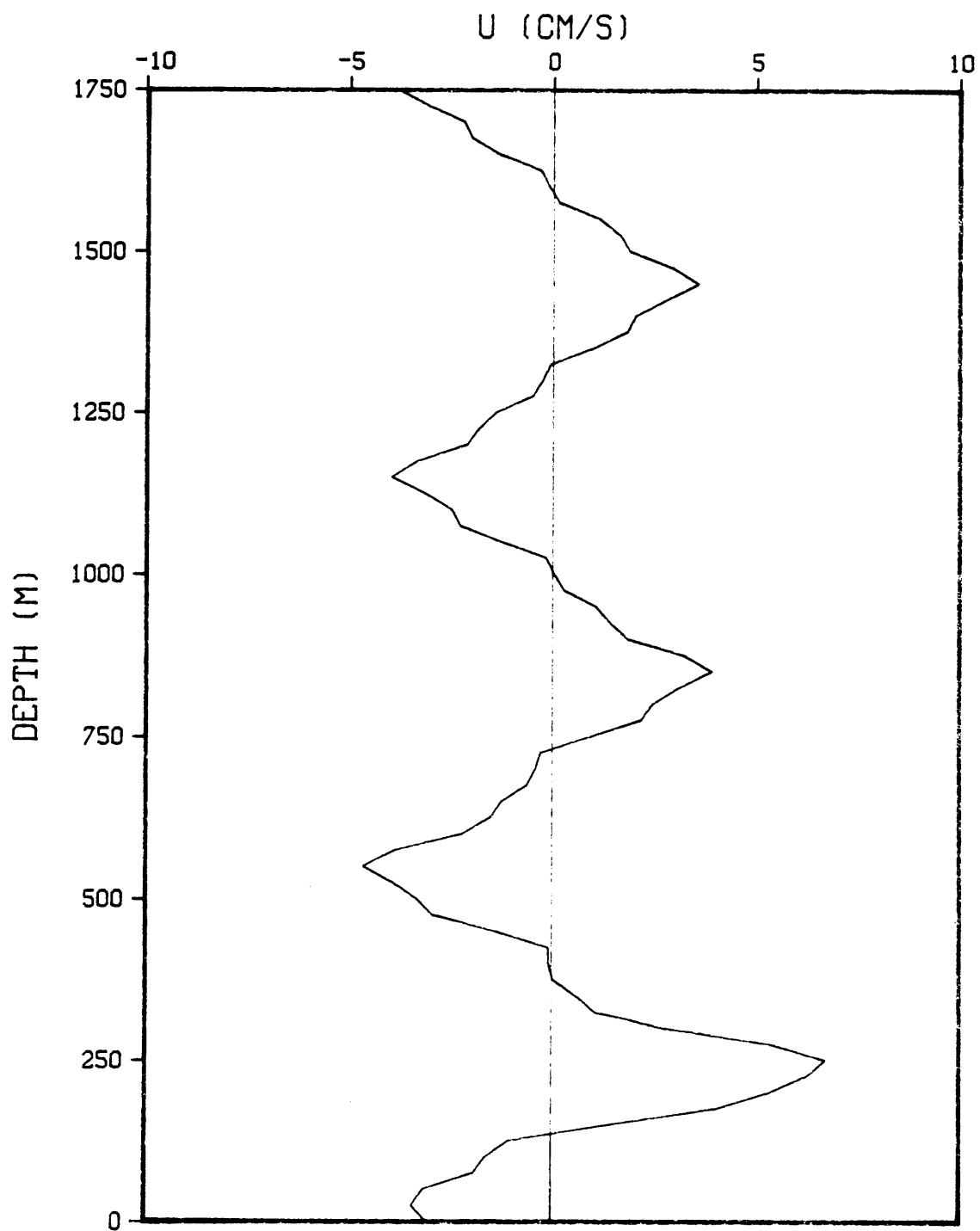
Fig. 5.6a. Vertical profile of zonal velocity obtained for solutions with no friction computed at the equator, at $x = -3000\,km$. Only the upper 1750 m of the water column are shown. The solutions are symmetric about the line $z = 0$.
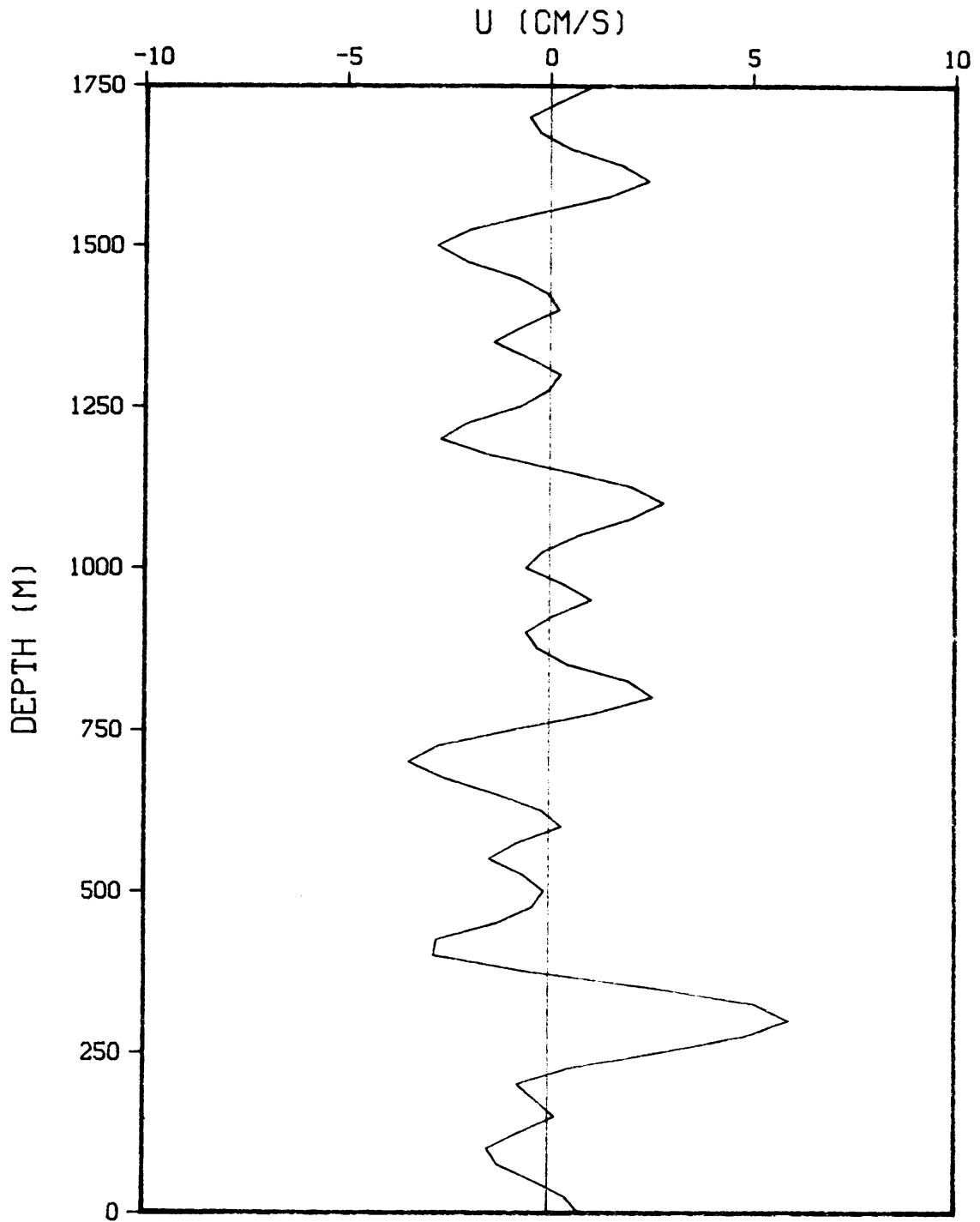
Fig. 5.6b. As in 5.6a, but for $x = -4000\,km$. Notice the marked difference between the dominant vertical scales here as compared with the scales in 5.6a.

Table 5.1. Distance X_r (expressed in kilometers) at which rays emanating from the point $(x, z) = (0, 0)$ strike the top or bottom ocean boundaries, for the values of ω and N given in (5.19).

j	X_r
1	23400
11	3050
21	1630
51	680

the whole ocean interior. Table 5.1 gives the zonal distance from the eastern wall at which the rays associated with several different meridional modes strike the top or bottom ocean boundaries, assuming they emanate from the point $(x, z) = (0, 0)$. At $x = -3000\,km$, only the rays corresponding to mode numbers $j = 1, 3, 5, 7, 9$ and 11 have not gone through any reflection process. In fact, for modes with $j > 21$, both top and bottom boundary reflections have occurred before the rays reach $x = -3000\,km$. Thus, the observed flow configurations in Figure 5.6 are essentially the manifestation of an interference pattern between 35 different energy rays, most of them having already reflected from the surface and bottom boundaries.

In light of the complicated pattern of ray crossings and the resultant constructive/destructive interference, it is perhaps not surprising that the vertical structure of the two solutions in Figure 5.6 computed at $x = -3000\,km$ and $x = -4000\,km$ (only 1000 km apart) is markedly different. Another factor contributing to this disparity is the divergence of the rays associated with the more strongly forced gravest meridional modes which have not yet undergone reflections at these longitudes.

Although the inclusion of a large number of meridional modes prevents a clear identification of each jet in Figure 5.6 in terms of the corresponding mode number, the signature of the $j = 1$ mode is still apparent in the largest eastward jet, centered at about 250 m (300 m), at $x = -3000\,km$ ($x = -4000\,km$). In fact, all the other peaks

in velocity are directly related to the presence of the $j = 3, 5, 7, 9$ and 11 modes, as illustrated in Figure 5.7, where we plot the same zonal velocity profile of Figure 5.6a, but now with only the first 6 meridional modes included in the summation. The maximum eastward and westward velocities in Figure 5.7 occur at the same depths predicted from tracing the different ray paths associated with each meridional mode and emanating from the point $(x, z) = (0, 0)$. The eastward jet at the surface corresponds to the $j = 11$ mode which, as given in Table 5.1, hits the upper boundary roughly 3000 km away from the coast. The existing wiggles in between the main jets come from the difficulty in reproducing, with a finite number of vertical modes, the discontinuity in the first derivative of the forcing function (5.1) at the upper and lower edges $(z = \pm l/2)$.

Since the character of solutions depicted in Figures 5.6 and 5.7 depends rather strongly on the energy reflection processes occurring at the top and bottom boundaries, one may doubt that these solutions would actually be realized in the real ocean. Afterall, the upper equatorial ocean exhibits a rich mean current system and critical layer absorption of wave energy would almost certainly happen in those surface layers (e.g., McPhaden et $al.$, 1986) . Also, the roughness of the bottom boundary would give rise to energy losses during the reflections at depth. We will not attempt to model these complicated processes here. Instead, the addition of small linear friction to our solutions will show that the energy traveling along the steeper ray paths is severely damped before penetrating too far into the ocean interior.

Figure 5.8 shows the zonal velocity field calculated as for Figure 5.6a, but with a linear friction coefficient equivalent to a spin down time of 8 years. A comparison of the two solutions reveals the strong effect of dissipation on the amplitude and structure of the flow field. All the jets seen in Figure 5.6a appear now with much smaller amplitudes, with the exception of the eastward jet at 250 m which corresponds to mode $j = 1$. It is useful to give the e-folding decay scales $c_n/r/(2j + 1)$ for some meridional modes, for the case of $n = 1$. Table 5.2 shows the disparity in the scales between different
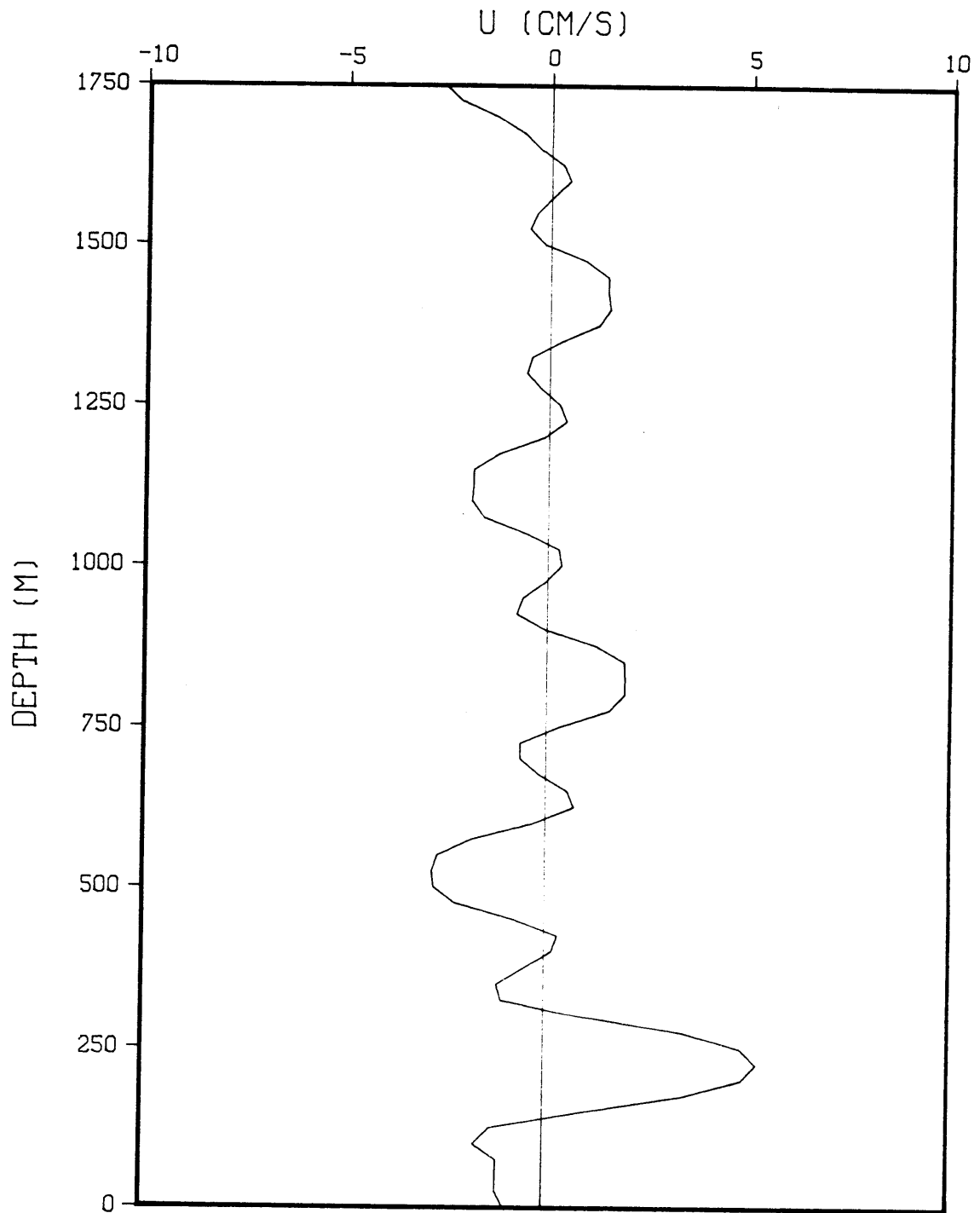
Fig. 5.7. Same as in Figure 5.6a, but here only the first 6 meridional modes are included in the solutions.
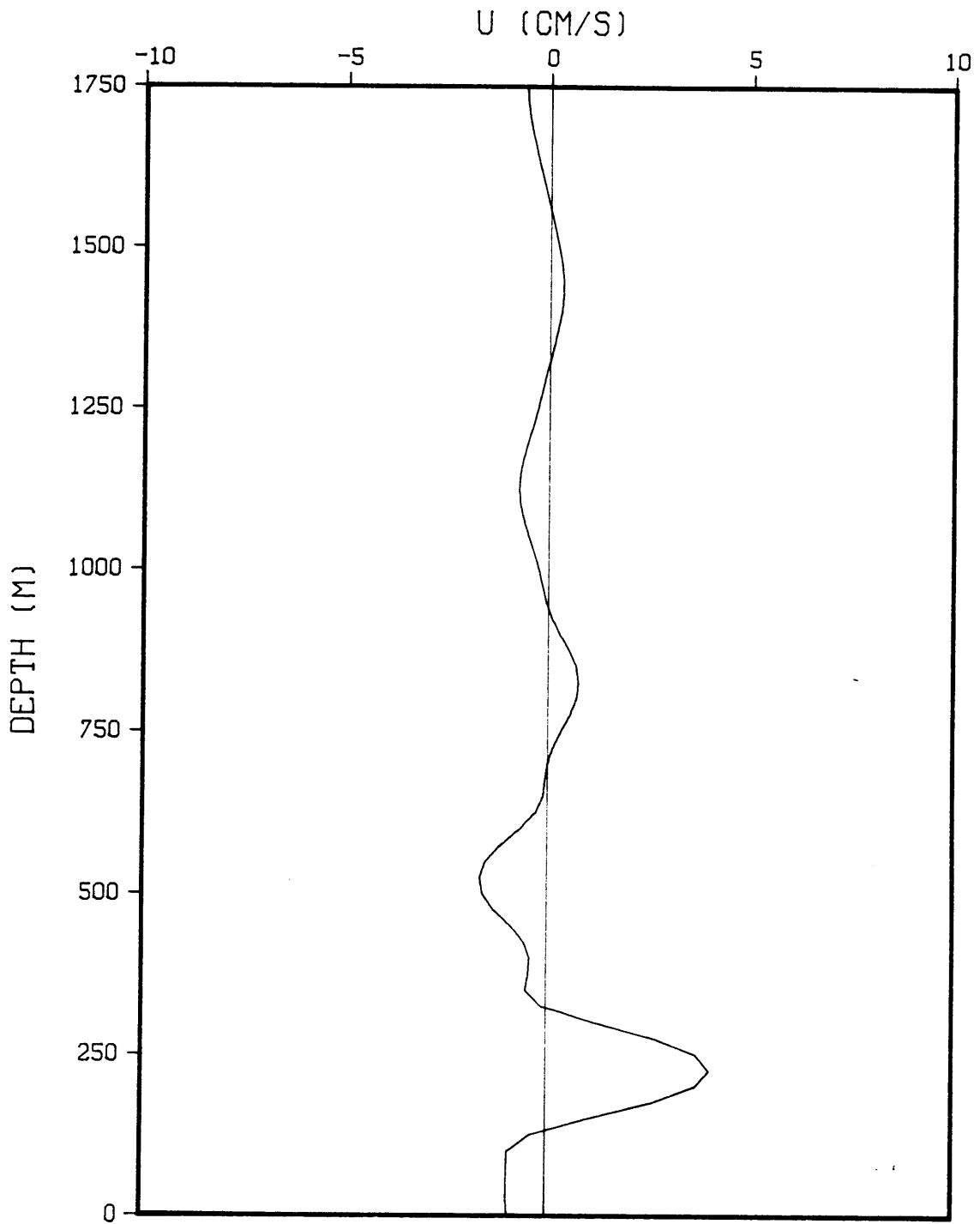
Fig. 5.8. The same as in Figure 5.6a, but here we add linear damping to the solutions. The spin down time used was 8 years.

Table 5.2. E-folding zonal decay scale X_e (expressed in kilometers) as a function of meridional mode number j, for the first vertical mode. Values for higher vertical modes can be obtained by dividing these by the respective mode number n.

j	X_e
1	93600
11	12200
31	4461
41	2285

meridional modes, resulting essentially from the large difference between their zonal group velocities. To get the e-folding scales for higher vertical modes, one has to divide the values in Table 5.2 by mode number n. It is then clear that most of the energy associated with high meridional modes will not make it too far west before being dissipated. Linearly damped solutions are primarily determined by the first few meridional modes, especially in the far field. The reflection processes at the top and bottom boundaries become irrelevant.

The meridional structure of this linearly damped solution is best shown in the contour plot of Figure 5.9. The latitudinal decay scale of the jet at 250 m closely follows that of the forcing ($\sim 80\,km$). All the other flows have magnitudes smaller than 1 cm/s, with the exception of the weak westward jet at 500 m, associated with meridional mode number $j = 3$.

Although we do not include any figure showing the time evolution of the flow field, the basic pattern of upward (downward) vertical phase propagation across each downward (upward) going ray observed for the Kelvin wave solutions is still present here, as expected from linear wave theory. Solutions with linear friction will exhibit this sort of behaviour, but this is not the case for the less realistic undamped solutions,
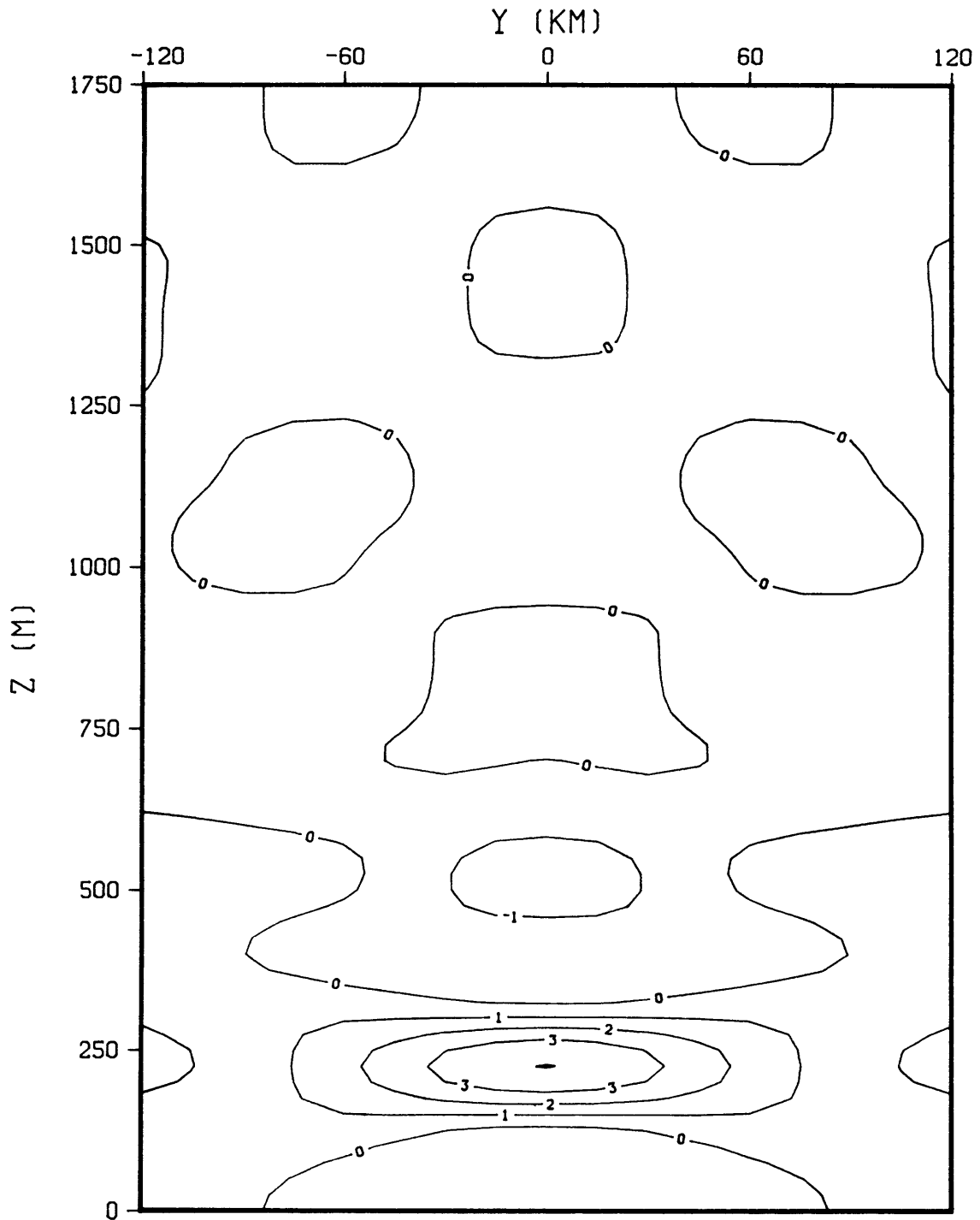
Fig. 5.9. Contours of zonal velocity in the y-z plane for linearly damped solution computed at $x = -3000\,km$, with a spin down time of 8 years. Contouring interval was 1 cm/s. Only the upper 1750 m are shown since solution is symmetric about the line $z = 0$.

133

where the sense of energy propagation is blurred by all the boundary reflections and consequent ray crossings.

5.4 Solutions for transient forcing

The periodic solutions analysed in the previous section showed the importance of the frequency composition of the forcing in determining the vertical structure of the flow fields. An interesting situation may arise if the time dependence of the forcing is not periodic. In the absence of any knowledge about the frequency composition of processes such as deep current fluctuations, it was sensible to assume the existence of a strong peak in the spectrum at some particular period. Nevertheless, it is possible that these hypothesized forcing mechanisms may be transient in character rather than periodic. Instead of looking at periodic solutions, here we consider the response to transient type forcing, where more than one frequency is present. To illustrate the basic differences between oscillatory and transient solutions, we choose a simple exponential time dependence for the boundary jet of the form

$$U(t) = U_0 \exp \left\{ - \left(\frac{t}{\Delta T} \right)^2 \right\} \tag{5.20}$$

where again the maximum amplitude U_0 is 10 cm/s and ΔT will be chosen latter. This particular choice is convenient since its Fourier transform is again an exponential of the same form, allowing for easy inversion of the Fourier transforms in (5.2) and (5.9).

If we use the Kelvin wave dispersion ($A.11$) to express k in terms of ω in (5.2) and evaluate the Fourier integral, we obtain solutions of the form

$$u = U_0 \sum_{n=1}^{\infty} A_n \exp - \left\{ \left(\frac{x}{c_n} - t \right) / \Delta T \right\}^2 \exp - \left\{ \frac{\beta y^2}{2 c_n} \right\} \cos \frac{N}{c_n} z \tag{5.21}$$

A similar procedure for the case of long Rossby wave solutions (5.9) yields

$$u = U_0 \sum_{n=1}^{\infty} \sum_{j=1}^{\infty} A_{n,j} \exp - \left\{ \left[(2j+1) \frac{x}{c_n} - t \right] / \Delta T \right\}^2 \cos \frac{N}{c_n} z \left[\frac{\psi_{j-1}}{\sqrt{2j}} - \frac{\psi_{j+1}}{\sqrt{2(j+1)}} \right] \tag{5.22}$$

In anticipation of the similarity between the Kelvin and Rossby solutions observed in the previous results, we will only show some relevant examples of the response to western boundary forcing. We use the same vertical and meridional scales for the boundary jet as given in (5.19), again summing only the first fifty vertical Kelvin modes in (5.21) and neglecting any frictional effects.

By choosing a relatively small value for ΔT, the exponential in (5.20) resembles to some extent an impulse occurring a $t = 0$. If we were actually forcing the model with a Dirac delta function $\delta(t)$, all vertical modes would be excited simultaneously at $t = 0$. As these modes propagated from the boundary, they would become separated due to their different propagation speeds. If we were to sit at some point x_0 far from the source, we would observe first the passage of the lowest mode which has the faster phase speed. All the other modes would follow sequentially, each one appearing separately at our site. Thus, a continuously changing, dominant vertical scale would be observed, unlike the solutions previously studied. Kawase (private communication) finds a similar pattern in his spin-up studies of an equatorial ocean, using a fully nonlinear model.

To illustrate this effect, we computed solutions for a value of $\Delta T = 1$ month. Figure 5.10 shows a time sequence of the zonal flows realized at a distance of 5000 km east of the forcing region and at $y = 0$. A change in the vertical scale is observed, as time progresses. At $t = 2$ months, a very broad first baroclinic mode predominates in the records, while for example 10 months later a vertical wavelength of roughly 500 m (corresponding to mode $n = 7$) is seen. The particular time pattern in Figure 5.10 is easily rationalized in terms of the different times each vertical mode takes to travel the 5000 km separating the "observation" point from the source. For instance, mode $n = 1$ takes roughly two months while mode $n = 7$ takes one year to cover that distance. Since the largest forcing amplitude occurs at $t = 0$, at $x = 5000$ km we are mainly seeing the energy associated with each vertical mode forced at $t = 0$, which has become dispersed zonally with time.
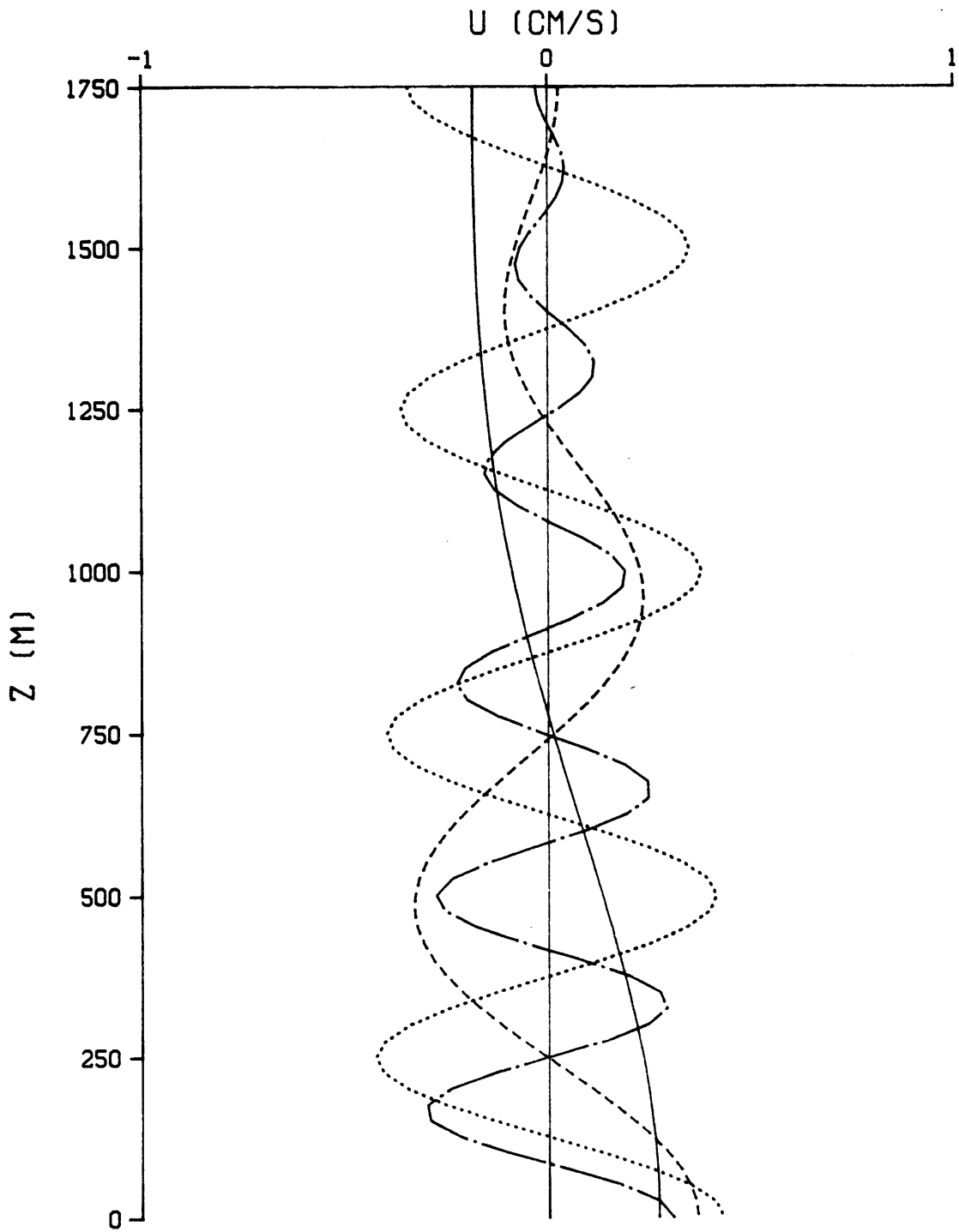
Fig. 5.10. Time sequence of Kelvin wave solutions showing the zonal velocity field 5000 km east of the source region, at $t = 2$ months (solid), $t = 6$ months (dashed), $t = 12$ months (dotted) and $t = 18$ months (chaindotted). Transient forcing of the form (5.20) was used, with $\Delta T = 1$ month and $U_0 = 10$ cm/s.

The vertical structure of these transient solutions is expected to vary substantially with longitude. Furthermore, the amplitude of the flows in Figure 5.10 is very small because of the short duration of the forcing and the dispersion effect discussed above. For a larger value of ΔT, stronger flows should therefore be observed together with slower variation in time of the dominant vertical scale, simply because more superposition of modes will occur. Figure 5.11 shows the same time sequence of Figure 5.10, but for solutions computed using a value of $\Delta T = 6$ months. Zonal flows are confined more closely to the depth where the forcing is placed, losing the individual mode character depicted in Figure 5.10. The longer time duration of the forcing allows for the coexistence of more vertical modes at each point in time and space. The absence of significant flows away from $z = 0$ is caused by destructive interference between these various modes.

In the time sequence of Figure 5.11, there is a clear increase in "baroclinicity" (i.e., number of wiggles) of the currents as time progresses. At $t = 2$ months, a rich mixture of modes combine to give a flow pattern closely resembling what we would expect from a steady forcing, with one main jet centered at $z = 0$. At latter times, the energy associated with the lowest modes has propagated faster to the east, leaving behind the higher baroclinic modes, which gradually gain more prominence in the solutions.
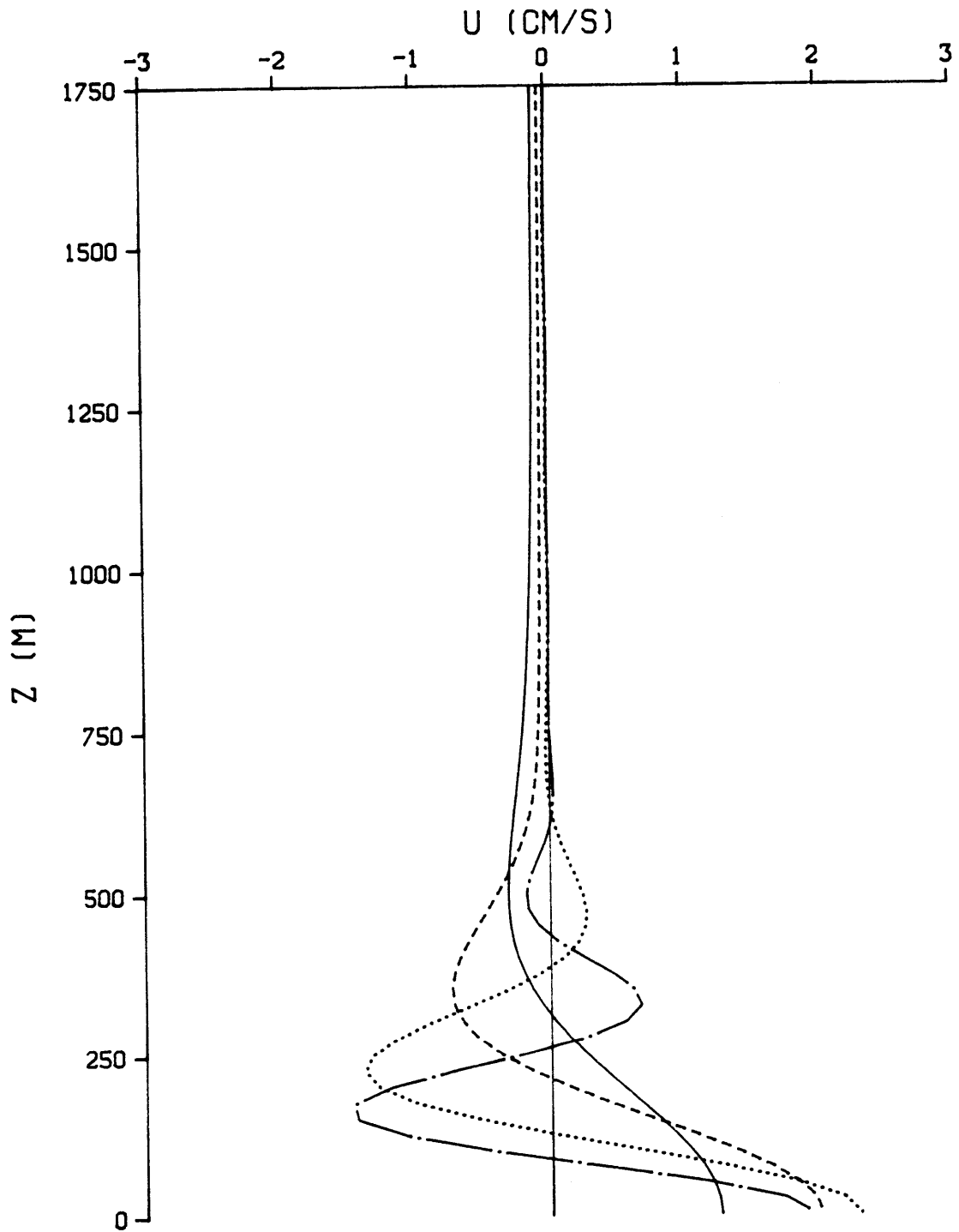
Fig. 5.11. The same as in Figure 5.10, but here we used $\Delta T = 6$ months, instead of the previous value of one month.

5.5 Forcing the model with a frequency spectrum

In most situations, a realistic description of the forcing involves a continuous distribution of energy among the various frequencies. We then characterize that dependence by defining a frequency spectrum. This section examines the response of our model to spectral forcing.

We begin by redefining the Fourier transforms of the solutions (5.2) and (5.9) to be

$$\hat{u}_k(\omega, x, y, z) = \sum_{n=1}^{\infty} A_n \hat{U}_0(\omega) e^{-i(x\omega/c_n)} \exp - \left\{ \frac{\beta y^2}{2c_n} \right\} \cos \frac{N}{c_n} z \qquad (5.23)$$

and

$$\hat{u}_r(\omega, x, y, z) = \sum_{n=1}^{\infty} \sum_{j=1}^{\infty} A_{n,j} \hat{U}_0(\omega) e^{ix(2j+1)\omega/c_n} \cos \frac{N}{c_n} z \left[\frac{\psi_{j-1}}{\sqrt{2j}} - \frac{\psi_{j+1}}{\sqrt{2(j+1)}} \right] \qquad (5.24)$$

where subscripts k and r stand for Kelvin and Rossby solutions respectively, with $\hat{U}_0(\omega)$ being the Fourier transform of the forcing as in (5.1).

To obtain the frequency response spectrum, we need to make the usual stochastic assumption of random phases between different frequency components of the forcing (e.g., Ponte, 1986). In mathematical terms,

$$< \hat{U}_0(\omega) \hat{U}_0^*(\omega') > = \Phi_f(\omega) \delta(\omega - \omega') \qquad (5.25)$$

where the angular brackets denote an ensemble average, the asterisk stands for complex conjugate, $\Phi_f(\omega)$ is the forcing spectrum and δ is the Dirac delta function.

Multiplying (5.23) and (5.24) by their complex conjugates, taking the ensemble average on both sides and using expression (5.25) yields

$$\Phi_k(\omega, x, y, z) = \sum_{n=1}^{\infty} \sum_{m=1}^{\infty} A_n A_m \Phi_f(\omega) Q_k(y, z) \exp \left\{ i\omega x \left(\frac{1}{c_n} - \frac{1}{c_m} \right) \right\} \qquad (5.26)$$

where

$$Q_k(y, z) = \exp \left\{ -\frac{\beta y^2}{2} \left(\frac{1}{c_n} - \frac{1}{c_m} \right) \right\} \cos \frac{N}{c_n} z \cos \frac{N}{c_m} z \qquad (5.27)$$

and

$$\Phi_r(\omega, x, y, z) = \sum_{n=1}^{\infty} \sum_{j=1}^{\infty} \sum_{s=1}^{\infty} \sum_{l=1}^{\infty} A_{n,j} A_{s,l} \Phi_f(\omega) Q_r(y, z)$$

$$\exp i \left\{ \frac{x}{c_n}(2j+1)\omega - \frac{x}{c_s}(2l+1)\omega \right\} \tag{5.28}$$

where

$$Q_r(y, z) = \cos \frac{N}{c_n} z \cos \frac{N}{c_s} z \left[\frac{\psi_{j-1}}{\sqrt{2j}} - \frac{\psi_{j+1}}{\sqrt{2(j+1)}} \right] \left[\frac{\psi_{l-1}}{\sqrt{2l}} - \frac{\psi_{l+1}}{\sqrt{2(l+1)}} \right] \tag{5.29}$$

Relations (5.26) and (5.28) give the frequency power spectrum of the Kelvin and Rossby wave response in terms of the forcing spectrum $\Phi_f(\omega)$, at each spatial point (x, y, z). Notice that the frequency dependence of $\Phi_k(\omega, x, y, z)$ or $\Phi_r(\omega, x, y, z)$ is not simply given by the spectral shape of $\Phi_f(\omega)$ but includes another factor dependent on the particular dynamics of the ocean response. These expressions do not include frictional effects, but they can be easily accomodated by carrying the exponential decaying terms discussed in section 5.2 in the calculations.

Using (5.26) or (5.28), one can compute the time variance associated with a particular frequency as a function of depth, at some point (x, y). Although not shown here, such calculations reveal a peak in variance along the expected energy ray paths associated with each frequency, just as we have found for the periodic case in section 5.3. This confirms a peculiar aspect of our model solutions: that energy associated with different frequencies tends to appear at separate depths in the water column.

Alternatively, assuming some form of $\Phi_f(\omega)$, one can integrate expressions (5.26) and (5.28) over ω and look at the z-structure of the total time variance. Results of such computations are presented in Figure 5.12. We assumed the forcing spectrum to

be constant up to a frequency corresponding to a period of 1 year and zero for higher frequencies. This choice was arbitrary, but it will serve our purposes here.

Plots in Figure 5.12a-b represent the total time variance on the equator at $x = 5000$ and $x = 10000$ km respectively, normalized by the value at $z = 0$, and associated with Kelvin wave solutions. No friction was included in the calculations. There is a maximum in energy centered at $z = 0$ related to the forced response at $\omega = 0$ (i.e., steady response). The energy present at other depths comes from higher frequency motions. The depth at which the variance decays to zero corresponds to the actual depth of the ray path associated with the highest frequency in the forcing spectrum (in our case, the equivalent period is one year). Energy is found within the cone traced by these steepest rays emanating from the source at $(x, z) = (0, 0)$. This is why at $x = 10000$ km energy is seen further away from $z = 0$ than at $x = 5000$ km. No other particular structure is realized in the distribution of energy with depth.

The same pattern arises in Rossby wave solutions, with the spectral forcing placed on the eastern boundary, as illustrated in Figure 5.12c. Here, we included small linear friction in the calculations, with a spindown time of eight years, to avoid all the reflections from the top and bottom boundaries as we have discussed in section 5.3. Only the first four even meridional modes were included, since higher modes contribute very little to the energy as discussed in section 5.3. The depth of the sharp cutoff in variance around 800 m corresponds to the depth of the steepest ray associated with first meridional modes. One slight difference between the Rossby and Kelvin solutions is the small energies seen at depths greater than 800 m in Fig. 5.12c, which come from the higher Rossby meridional modes (primarily mode $j = 3$).

If instead of a flat forcing spectrum, we had chosen a more structured form in frequency, the computed total variance would be itself more structured in depth. For instance, a general red spectrum would cause the sharp decays in energy at certain depths to be more gradual, while the presence of peaks at some frequencies would show
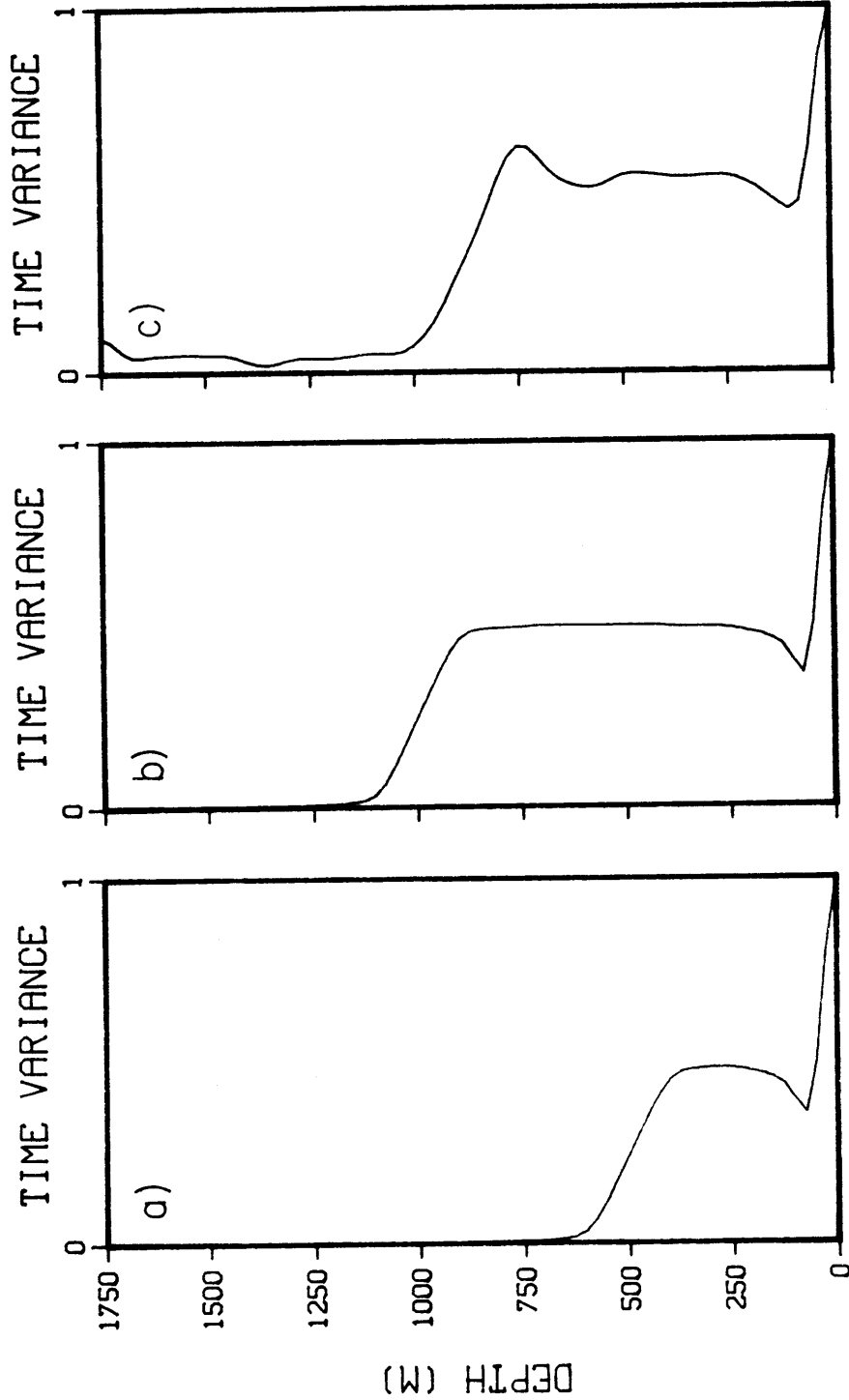
Fig. 5.12. Total time variance for Kelvin wave solutions at $y = 0$ and $a)$ $x = 5000$ km $b)x = 10000$ km and $c)$ Rossby wave solutions at $x = -3000$ km. Amplitudes were all normalized by amplitude at $z = 0$. Because of the symmetry about $z = 0$, only the top half of the water column is shown.

up as maxima in energy at depths coinciding with ray paths associated with those frequencies.

5.6 Discussing model results

The simple model solutions we have discussed serve to illustrate the basic nature of the linear response of the equatorial waveguide to forcing at mid-depth. For both eastern and western boundary forcing, the energy propagates away from the source into the interior along the possible ray paths predicted by linear wave theory. This was particularly evident in the periodic solutions studied in section 5.3. The essential difference between the two cases lies in the number of rays available. The energy available at the eastern wall can in theory propagate along an infinite number of rays sloping at different angles to the horizontal, each one associated with a different long Rossby wave meridional mode. However, in practice, the presence of small linear friction severely damps most of these energy beams due to their very slow zonal group speeds (the higher the mode number j, the slower the group velocity). Frictional solutions for the Kelvin and Rossby wave response look in fact very similar in the far field.

With both periodic and transient forcing, our model is able to produce highly baroclinic zonal flow fields which resemble, at least qualitatively, the sheared flows in the observations. The short vertical scales of the response are essentially set by the vertical scale of the forcing. Although little is known about the actual scales of deep energy sources (e.g., cross-equatorial deep water mass signals) at the equator, it is reasonable to suppose that these deep currents have vertical scales of the same order of the values we have assumed for our boundary jet. Deep boundary forcing of the equatorial regions will most likely give rise to interior flows of short vertical wavelengths.

The model is also able to account for the difficulty in observing vertical phase propagation in the records. Depending on where we look in the water column, even

for the simple periodic case, model solutions can exhibit both upward and downward phase propagation (across each energy beam) or behave in a standing mode fashion. If the forcing comprised both periodic, transient and steady components, the propagation patterns would be even more blurred. The pattern of vertical phase and energy propagation also depends on the actual depth at which we place the forcing jet. For the symmetric case of a source exactly at mid-depth (the case considered here in more detail), upward and downward energy propagation occurs above and below $z = 0$ respectively. If instead we assume the forcing to be at the bottom (surface), upward (downward) energy propagation would predominate in the solutions, provided that no significant boundary reflections took place. The occurrence of wave solutions carrying energy upward is itself a relevant feature of this model, not easily reproduced with models that put the forcing at the ocean surface.

Discrepancies between some model features and the observed records should be mentioned. The particular pattern of zonal currents depends on whether the forcing is assumed to be periodic, transient, or some mixture of these two kinds of time dependence. In the case of periodic forcing, instead of the series of alternating zonal currents seen in the observations, both Kelvin and Rossby wave solutions exhibit in general only two main jets associated with the two ray paths available (Rossby solutions have a second but weaker jet associated with the third meridional mode). If we force our model with an oscillatory jet at more than one frequency, then the available number or ray paths is much larger in general (recall that ray slopes are given by $\pm\omega/N$ for the Kelvin wave, and $\pm(2j + 1)\omega/N$ for the long Rossby wave). Since the baroclinic structure of the flow fields in this case merely reflects the possible energy propagation patterns, the frequency composition of the forcing is of ultimate importance in determining such structure. This is an unfortunate feature of the model when combined with the total lack of observational knowledge we have on such composition. On the other hand, the single baroclinic mode like flows observed in the case of transient forcing show a greater

resemblance to the observations (see Figure 5.10), but they have very small amplitudes and are not zonally homogeneous (i.e., vertical scales at a given time change rapidly with zonal distance).

Flow amplitudes in the model are in general small (less than 5 cm/s), as compared with EDJ observed values (more like 10 cm/s). Although we could increase the amplitude of the forcing jet, a deep current oscillating with amplitudes much larger than 10 cm/s is not likely to occur. In addition, if there are strong currents in the deep ocean, they most probably do not reverse direction as implied in the forcing used here. Hence, a more reasonable representation for such deep processes would include a mean plus an oscillatory flow. However, to the extent that the model is linear, the oscillatory response would be the same in both cases. The wave solutions considered here would be superposed on the mean circulation resulting from the steady part of the forcing. The character of this mean flow response has not been studied in detail, but at least its geostrophic component is easily determined by letting the forcing frequency ω go to zero in the solutions discussed here. In this case, the steady response simply consists of a strong jet centered at $z = 0$ and decaying away from the boundaries in the zonal direction due to frictional effects.

Some of the assumptions made in our model were obviously arbitrary. For solutions so dependent on the actual ray paths, it is clear that the buoyancy frequency profile chosen will affect the overall pattern of energy propagation. By using a constant N, we made all the rays paths straight lines in the x-z plane. If we had chosen N to be a function of z, then energy would not travel along straight lines anymore, but would be refracted towards the region of lower buoyancy frequency values (i.e., rays would bend downward). This would destroy the symmetry of solutions about the line $z = 0$, with upward going rays becoming more horizontal as they approached the thermocline region where N is usually large, and downward going rays becoming steeper. Moreover, for the case of eastern boundary forcing, the rate at which the long Rossby wave rays

diverge away from the source would decrease (increase) for the ones carrying energy upward (downward) from the forcing region. Since the divergence of ray paths is one of the causes for the change in vertical structure between zonal flows computed at different longitudes, a variable N would in general make the flow fields above the forcing depth (i.e., $z > 0$ in our case) look more homogeneous horizontally. The reverse situation would be true for the flow field lying below the forcing depth.

Although the model discussed here does not provide a definite explanation of the EDJ, it nevertheless suggests the general importance of deep boundary energy sources in forcing deep flows in the equatorial band. More observations are certainly needed near the boundaries to reveal the connections (if any) between boundary processes and the interior circulation. In particular, monitoring of deep water mass signals as they enter the equatorial regions would be needed to understand how much of these cross-equatorial flows actually turn along the equator and on what time scales do they vary. This may be a difficult goal to accomplish, given the likely small amplitudes and long time scales of these processes. Furthermore, oceans such as the Pacific do not present a clear choice on where to look for them. It may well be that significant energy sources exist at several longitudes and depths, in which case the observational task becomes even more difficult.

It remains to be seen whether a more complicated model will provide solutions much different than the ones obtained here. Kawase (private communication) plans to run his numerical model with periodic forcing in the near future. To the extent that his spin-up solutions exhibit in general a linear character, perhaps the model's response to periodic forcing will not differ much from the scenarios presented here, unless his off-equatorial forcing excites flows along the western boundary and near the equator, with vertical structures significantly more complex than the single zonal jet confined to a certain depth that we have assumed here.

PART II. Equatorial Kelvin waves in the presence of mean flows

5.7 Introduction

We have seen previously the general difficulty in getting energy associated with surface forced low frequency linear equatorial waves to propagate down into the deep ocean, either because of critical layer absorption effects (McPhaden *et al.*, 1986), reflections from the thermocline (Gent and Luyten, 1985) or, perhaps more important, because of slow vertical group velocities (and consequent shallow rays descending from the surface). This led us to consider in Part I the alternative possibility of having deep energy sources exciting the wave guide. Here, we explore a different mechanism by which energy input at the surface can efficiently drive the deep ocean and create currents at considerable depth, in the presence of mean flows.

Instead of forcing the ocean with surface winds (or surface heat fluxes for that matter), we propose that the deep ocean is driven by divergence or convergence patterns associated with upper ocean currents (e.g., the equatorial Undercurrent) or upward and downward movements of the thermocline, and acting essentially as a vertical velocity at the base of the thermocline region. In this case, no energy loss due to the absorption or reflection effects mentioned before will occur in the active upper ocean layers. Solutions from the primitive equation numerical model of Philander and Pacanowski (1981) show these processes at work. In one case, Rossby waves observed in the deep ocean are forced by the divergence associated with the equatorial Undercurrent impinging on the eastern boundary. Furthermore, it is reasonable to assume (Philander, 1979) that the deep ocean does not affect the upper ocean on time scales shorter than a diffusive time scale. Therefore, for our purposes, we may treat the shallow and deep oceans as being essentially uncoupled, and parameterize the highly nonlinear upper ocean processes in some crude way to come up with a "surface" forcing boundary condition for the deep ocean.

The existence of mean flows may strongly influence the characteristics of linear waves and the patterns and rates of energy propagation of energy associated with them, either by simply allowing for resonances to occur (i.e., situations where the zonal group velocity vanishes) or by providing for possible instabilities or wave-mean flow interactions to take place. McCreary and Lukas (1986) were able to generate short vertical scale steady zonal flows corresponding to resonant stationary Kelvin waves forced by a patch of steady zonal wind, by assuming the presence of a constant mean westward flow from top to bottom. Their solutions at depth qualitatively resembled the observations, but the corresponding upper ocean circulation was very unrealistic. Here, we wish to model similar Kelvin wave resonances using different assumptions about the forcing, but also examine the effects of large scale mean vertical shear on the character of the solutions and qualitatively discuss possible wave-mean flow interaction phenomena.

5.8 A simple Kelvin wave-mean flow model

The present observational evidence for the existence of mean deep zonal flows in the equatorial regions, particularly in the Pacific, is not by any means conclusive, but there seems to be a reasonably number of studies which have found westward flow below the equatorial Undercurrent (e.g., Taft *et al.*, 1974; Eriksen, 1985; Firing, 1987), with a wide range of amplitudes on the order of roughly 10 *cm/s*. A mean computed from all the PEQUOD equatorial profiles also reveals a region of westward flow extending to 1000 *m*. It remains to be seen whether these flows, sometimes referred to as the Equatorial Intermediate current, really persist in time as to be considered part of the mean equatorial circulation, but it is rather curious that some of the theoretical models of the upper ocean (e.g., see review by McCreary, 1985) also develop mean westward flows below the Undercurrent as part of their steady solutions.

Given our hypothesis that the relevant forcing for the deep ocean occurs at the base of the thermocline, the presence of these hypothetical westward mean currents below the core of the Undercurrent must play a role in shaping the deep ocean response. In particular, eastward propagating Kelvin waves can be held stationary leading to the possibility of resonances to occur. Consider then a simple model of Kelvin waves imbedded in zonal mean flow U. For the moment we take U to be constant, but later we will examine the effect of having a mean vertical shear. In this case, after eliminating p and w, the Kelvin wave equations become

$$\Re u + p_x = 0 \tag{5.30a}$$

$$\beta y u + p_y = 0 \tag{5.30b}$$

$$\Re p_{zz} - N^2 u_x = 0 \tag{5.30c}$$

where the operator $\Re = \partial_t + U\partial_x + r$, u and p are the perturbation zonal velocity and reduced pressure respectively and r is the coefficient of linear damping. Our model ocean has no boundaries. Energy reflections off side or bottom walls will not contribute to the solutions. Eliminating p between (5.30b) and (5.30c) leads to the equation in u

$$\beta y \Re u_{zz} + N^2 u_{xy} = 0 \tag{5.31}$$

which we solve by assuming general solutions of the form

$$u = \left(\frac{1}{2\pi}\right)^2 \int\limits_{-\infty}^{+\infty}\int\limits_{-\infty}^{+\infty} \hat{u}(\omega, k, y, z)e^{i(kx-\omega t)}dk d\omega \tag{5.32}$$

Substitution of expression (5.32) in equation (5.31) leads to the following form for the Fourier transform

$$\hat{u}(\omega, k, y, z) = A(\omega, k)e^{imz}\exp - \left\{\frac{\beta m y^2}{2N}\right\} \tag{5.33}$$

149

with the dispersion relation being given by

$$\omega = \left(\frac{N}{m} + U\right) k - ir \tag{5.34}$$

The choice e^{imz} instead of e^{-imz} in (5.33) assures the proper sign of energy propagation at large z (i.e., we want solutions with positive vertical phase speed, to satisfy the usual radiation boundary condition at $z \to -\infty$). $A(\omega, k)$ is determined by the amplitude of the prescribed forcing at each frequency and zonal wavenumber component. The vertical wavenumber m is in turn determined from the dispersion relation for each given ω and k. Notice that with the inclusion of linear damping, m becomes a complex quantity, giving rise to an exponential decay term in z in solutions (5.32). This also affects the meridional dependence, contributing an oscillatory part to the usual exponentially decaying term $\exp(-\beta my^2/2N)$.

Let us consider the model response to a localized steady pattern of downwelling, i.e., we assume our ocean is forced at $z = 0$ by a vertical velocity of the form

$$w = w_0 e^{-(\gamma x^2 + \mu y^2)} \tag{5.35}$$

where γ and μ define the decay scales in x and y. We may think of this vertical velocity as being associated with the downwelling which likely occurs below the core of the Undercurrent, as some models indicate (McCreary, 1985). The exponential dependence is convenient because its Fourier transform has the same form. In the steady case considered here, we set $\omega = 0$ in (5.34), which amounts to letting $\partial_t = 0$ in the operator $\mathfrak{R}$ of equation (5.31). Solving the dispersion relation (5.34) for m yields

$$m_r = -\frac{Nk^2 U}{U^2 k^2 + r^2} \tag{5.36a}$$

$$\begin{aligned} m_i &= -\frac{Nkr}{U^2 k^2 + r^2} \\ &= \frac{m_r}{Uk} r \end{aligned} \tag{5.36b}$$

150

where subscripts r and i denote the real and imaginary parts of m, respectively. Notice that m_i^{-1}, the decay depth scale, is just equal to the vertical group velocity of the Kelvin wave with vertical wavenumber m_r times the spindown time r^{-1}. For solutions to decay away from the forcing region at $z = 0$, only positive zonal wavenumbers, for which $m_i < 0$, should be considered in the Fourier integral (5.32).

To determine $A(k)$ in (5.33), we use continuity to find w from zonal velocity solutions and match it to the boundary condition (5.35) expressed as a Fourier transform in x. After some algebra, we obtain

$$A(k) = -2w_0 \frac{m}{k} \hat{w}_f(k) \frac{\int\limits_{-\infty}^{+\infty} \exp -\{(\mu + \frac{\beta m}{2N})y^2\}\, dy}{\int\limits_{-\infty}^{+\infty} \exp -\{\frac{\beta m y^2}{N}\}\, dy} \qquad (5.37)$$

where

$$\hat{w}_f(k) = \left(\frac{\pi}{\gamma}\right)^{1/2} \exp\left\{-\frac{k^2}{4\pi\gamma}\right\} \qquad (5.38)$$

is the Fourier transform of the forcing function (5.35) and the integrals over y on the right hand side of (5.37) come from the projection of the meridional structure of the forcing onto the Kelvin waves, as already explained in section 5.2.1. The factor of two in (5.37) arises because we only consider positive zonal wavenumbers. The integrands in (5.37) are complex (recall that m is complex) and to evaluate them, it is easier to separate each of them into two integrals involving only real integrands. The algebra is a little messy, but with the help of a table of integrals (Gradshteyn and Ryzhik, 1965), we arrive at

$$A(k) = -2w_0 \frac{m}{k} \hat{w}_f(k) \left[\frac{4\beta^2(m_r^2 + m_i^2)}{(2N\mu + \beta m_r)^2 + \beta m_i^2}\right]^{1/4}$$
$$\exp\left\{\frac{1}{2}\tan^{-1}\frac{|m_i|}{m_r} - \frac{1}{2}\tan^{-1}\frac{\beta|m_i|}{2N\mu + m_r}\right\} \qquad (5.39)$$

where m_r and m_i are the real and imaginary parts of m defined in (5.36). Notice that if we let m_i go to zero (i.e., $r = 0$), we regain the results found in (5.5) for the case of m real, as we should.

151

The Fourier transform $\hat{u}(k, y, z)$ of our solution, now completely defined by expressions (5.38-5.39), is a fairly complicated function of zonal wavenumber k. However, in the special case of no linear friction (i.e., $r = 0$), the vertical wavenumber is simply given by

$$m_r = -\frac{N}{U}, \qquad m_i = 0 \tag{5.40}$$

from (5.36). There is no decay in z, but more importantly, m is now a constant, independent of k, and the vertical structure of solutions is dominated by a single wavelength determined from the values of N and U. The flow field corresponds to that of the stationary Kelvin wave with zonal phase speed $c_x = N/m$ equal and opposite to the mean flow U.

The addition of friction makes m dependent on k in general, and the mathematics a lot more complicated, but solutions should retain the selective character with respect to vertical scale, present in the frictionless case. To find linearly damped solutions we inverted the Fourier transform $\hat{u}(k, y, z)$ numerically. Because of the exponential decay term contained in (5.38), we cut the numerical integration at relatively low wavenumbers without affecting the results. Also, to have solutions decaying away from $z = 0$, integration was carried out over positive wavenumbers only.

Figure 5.13 shows the zonal flow field obtained for the following values of the parameters:

$$U = -10\,cm/s \tag{5.41a}$$

$$w_0 = -10^{-4}\,cm/s \tag{5.41b}$$

$$\mu = 1.6 \times 10^{-10}\,m^{-2} \tag{5.41c}$$

$$\gamma = 1.6 \times 10^{-3}\,m^{-2} \tag{5.41d}$$

$$N = 2 \times 10^{-3}\,s^{-1} \tag{5.41e}$$
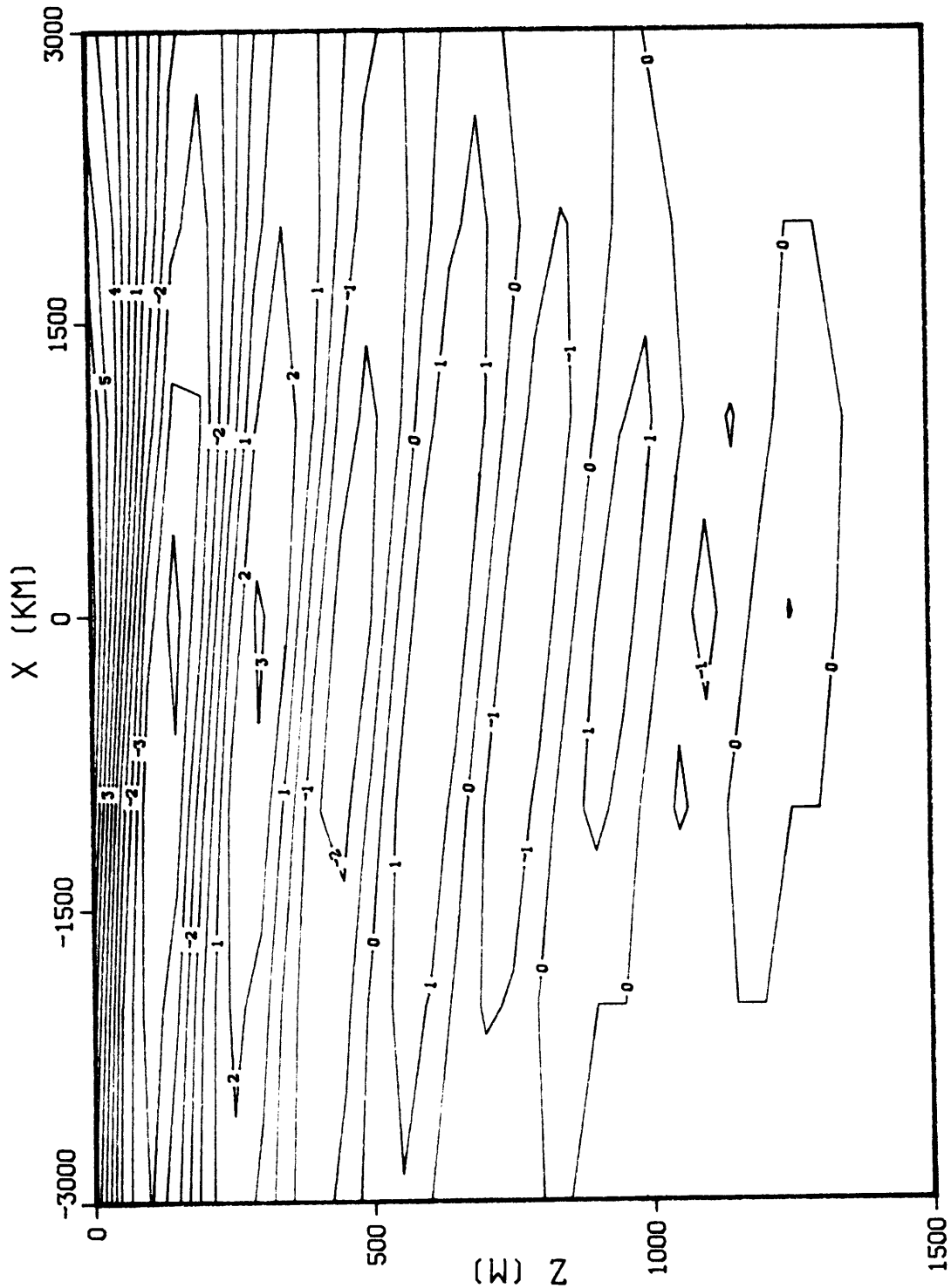
$$r^{-1} = 10\,yr \tag{5.41f}$$

Fig. 5.13. Contour plot of the zonal currents along the equator, obtained with forcing function (5.35) centered at $x = 0$. Only the perturbation flow is shown. Contour interval is 1 cm/s. Maximum amplitudes of 7 cm/s are observed right below the region of strongest forcing at $(x, z) = (0, 0)$ and decay with depth, becoming smaller than 1 cm/s below 1400 m. Notice the short vertical scales and the downward tilt of phase lines to the east.

The values for γ and μ correspond to zonal and latitudinal decay scales of 2500 km and 80 km, respectively. A westward mean flow of 10 cm/s seems a reasonable estimate for U (e.g., Eriksen, 1985) and an order of magnitude estimate for w_0 was chosen based on solutions of some theoretical models (McCreary, 1981; McPhaden, 1981). These choices are more or less arbitrary, and some of them will affect the character of the solutions. The dependence of model results on the parameters will be discussed below.

The zonal currents displayed in Fig. 5.13 consist of alternating bands of eastward and westward flow decaying in amplitude with depth from a maximum of 7 cm/s at the surface, with the strongest flows occurring right below the region of maximum amplitude in the forcing. To get the total velocity field, the mean westward flow would have to be added to Fig. 5.13. The currents shown are associated with stationary Kelvin waves forced at $z = 0$. There is a definite tilt of constant phase lines down toward the east in the solutions, corresponding to a zonal wavelength of roughly 12000 km. We can explain the sign of this tilt by considering the actual spin-up process of such solutions. To set up the steady flow, energy is carried down from the forcing region by Kelvin waves with upward phase propagation. This implies in turn phase line tilts of the sign observed in Fig. 5.13. The meridional structure of the solutions is best seen in the contour plot displayed in Fig. 5.14, in which the equatorial trapped nature of the flow is evident. The meridional decay scale follows roughly that of the forcing (80 km). The observed dominant vertical wavelength on the order of 300 m corrresponds to that of a Kelvin wave with zonal phase speed of roughly 10 cm/s, equal and opposite to the mean flow. Thus, the oscillatory vertical scale of the frictional solutions is in fact determined by the value of U and N ($c_x = -U = N/m$). Doubling the value of U would double the vertical wavelength of the currents in Figs. 5.13-5.14 to 600 m.

The flow amplitudes at the surface are essentially determined by the amplitude w_0 of the forcing. For our choice of parameters, solutions in Figs. 5.13-5.14 are reasonably linear especially away from the surface, in the sense that the perturbation flows are
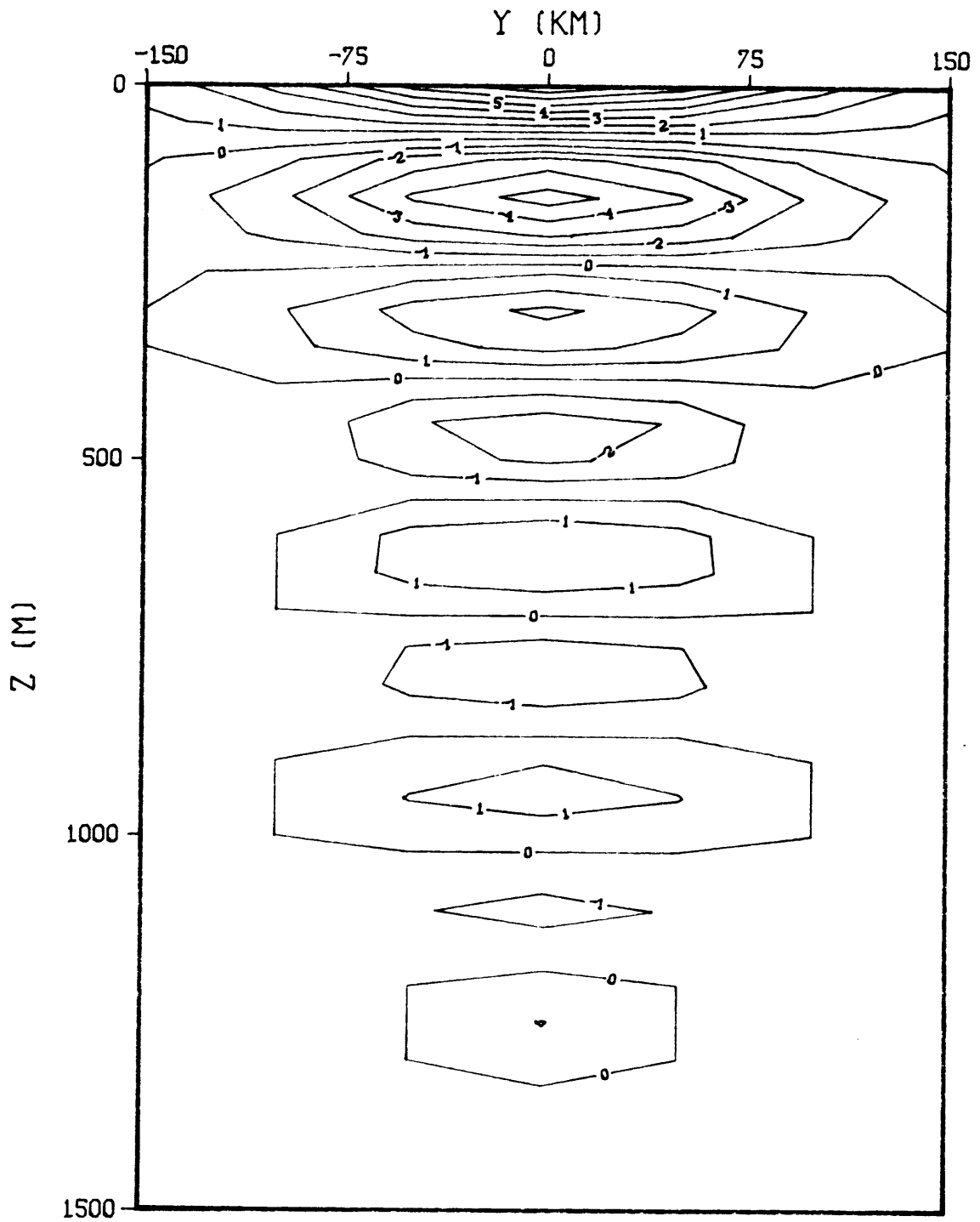
Fig. 5.14. Contour plot of zonal currents in the y-z plane, obtained at $x = 0$ where the forcing is strongest. Contour interval is 1 cm/s.

smaller than the mean flow U. Assuming larger values of w_0 would lead to stronger currents, but that would also make the perturbation approach invalid, since the neglected nonlinear term $u\partial_x$ in (5.30) would become of the same order (or actually bigger) than $U\partial_x$. Amplitudes decay away from the surface due to linear friction. The value of 10 years for the spindown time seems reasonable. For a wavelength of 300 m, it corresponds to a vertical mixing coefficient of roughly 0.1 $cm^2 s^{-1}$. Longer spindown times lead to an increase in the depth of energy penetration, but have little effect on changing the general amplitudes of the currents. The decay scale roughly agrees with that of a Kelvin wave with zonal and vertical scales of 12000 km and 300 m respectively, as given by relation (5.36b).

The qualitative agreement (in the deep ocean) found between our solution and that of McCreary and Lukas (1986) is not surprising, given that in both models stationary Kelvin waves play a dominant role in setting up the flow field. However, we must interpret them in a different context because of the different assumptions made about how the deep ocean is driven. The inability of their model to produce a realistic circulation in both the upper and deep oceans (for reasonable flows at depth, the surface currents have unreasonably large amplitudes and very short vertical scales) suggests that surface winds are probably not relevant in forcing deep stationary Kelvin waves. Furthermore, the upper ocean mean zonal circulation is fairly strong and changes direction, in contrast with the weak flows needed to get waves with vertical scales resembling the observations. If resonant Kelvin waves are indeed responsible for the presence of strong flows of a dominant short vertical scale in the deep ocean circulation, then they are most likely forced below the Undercurrent as assumed here, where mean flows (if any) are certainly weaker and less strongly sheared in the vertical.

As for the relevance of these solutions to deep jet dynamics, they have some obvious strong and weak points. Provided that a mean westward flow of amplitude roughly equal to the one assumed here exists, they give rise to Kelvin wave like currents of

156

a dominant short vertical scale and long zonal scales, with phase lines tilting down towards the east, all of which are features of the PEQUOD data. Their steady character may also account for the difficulty in observing large vertical phase shifts in the records. However, they still decay rapidly away from the surface and can not explain, for example, the occurrance of the strongest jets around 1500 m which is seen in the raw records (Figs. 2.2 and 2.3). Another weak point is the strong dependence of the vertical scale on the value of U.

One possible way of enhancing the downward propagation of energy is to hypothesize the presence of a mean negative vertical velocity, in which case the dispersion relation is given by

$$\omega = \left(\frac{N}{m} + U\right) k + Wm - ir \tag{5.42}$$

where W is the mean vertical velocity. Regardless of whether these flows really exist, in addition to getting energy to penetrate deeper, they also have the adverse effect of causing the Kelvin waves to become dispersive in the zonal direction (i.e., c_x is no longer equal to c_{g_x}). Therefore, for stationary solutions, energy does not stay below the forcing region but appears much further to the east, with boundary reflections more likely to become important.

The treatment of the time dependent problem, where we let the forcing in (5.35) be a function of time, is considerably more complicated than the steady problem, because both eastward and westward traveling waves are in general possible and critical layers may occur. However, in the case of eastward traveling forcing disturbances, solutions are still Kelvin waves with zonal phase speed $c_x = N/m + U$ equal to that of the forcing. Therefore, in the presence of mean westward flow the forced vertical wavelength is longer than for the case $U = 0$. An upper limit for the value of m is set by the amplitude of U, since for reasonably high vertical wavenumbers, c_x would become negative.

5.9 Stationary Kelvin waves in vertically sheared zonal mean flows

Although the claim for the presence of mean westward zonal flow below the Undercurrent has some observational and theoretical basis, the assumption that it is constant in z and extends to the bottom is totally unfounded, from either point of view. Perhaps a more realistic assumption is to have the flow decay slowly with depth. In this section, we analyse the effects of mean vertical shear on the solutions previously discussed. The subject of linear equatorial waves in shear flow has been extensively studied in the meteorological literature (e.g., Holton, 1975). The relevant work to our problem was that of Lindzen (1971), where he used the mathematical method of multiple scales to find the zeroth order fields of Kelvin and Yanai waves propagating through vertical shear. The necessary condition for the validity of this technique is that the vertical wavelength of the waves be smaller than the characteristic scale of variation of the mean flow. This condition is certainly violated in the surface layers of the equatorial ocean where the vertical scale of the shear associated with the Undercurrent is on the same order of the wave scales of interest. Thus, the theory has never been applied to the oceans. However, in our case we may use the multiple scale method under the assumption that the deep mean flows have relatively large scale shear.

Here, we will use the Kelvin wave solutions found by Lindzen (1971). To keep the presentation brief, only the necessary details of his procedure will be included. For a complete derivation, the reader should consult Lindzen's paper or the summary given in Holton (1975). We consider linear equatorial waves embedded in a mean zonal flow $U(z)$ taken to be constant in latitude, and in geostrophic balance. Our constant N ocean has no boundaries. The governing perturbation equations are

$$\Re u + wU_z + -\beta yv + p_x = 0 \qquad (5.43a)$$

$$\Re v + \beta yu + p_y = 0 \qquad (5.43b)$$

$$p_z + \frac{g}{\rho_0}\rho = 0 \qquad (5.43c)$$

$$u_x + v_y + w_z = 0 \qquad (5.43d)$$

$$\Re\rho + v\left(\frac{\beta y}{g}U_z\right) - w\frac{N^2}{g} = 0 \qquad (5.43e)$$

where again the operator $\Re = \partial_t + U\partial_x + r$. The last terms in the density equation
(5.43e) represent the advection of mean density field gradients $\bar{\rho}_y$ and $\bar{\rho}_z$ after use of
the thermal wind relation and the definition of N. The system (5.43) can be combined
to yield a single equation for perturbation pressure p, which is generally not separable
in y-z. To proceed, Lindzen splits the vertical dependence into two variables: a "slow"
variable $\tau = \epsilon z$, where $\epsilon \ll 1$, on which U varies by order one (i.e., $U = U(\tau)$ only);
and a "fast" variable $\hat{z} = \int_0^z f(\tau)dz'$, on which the wave fields vary, where $f(\tau)$ is a local
vertical wavenumber which is determined from the solution. In addition, y is replaced
by the scaled variable $\xi = y/l(\tau)$, where $l(\tau) = l_0(\tau) + \epsilon l_1(\tau) + ...$ is also determined
from the solution. This accounts for the effect of the mean shear on the meridional
scale of the waves. Making these change of variables in the equation for p and further
assuming the Richardson number $Ri = N^2/U_z^2$ to be large, solutions are then found
by expanding p in powers of ϵ and solving the equation at each order. The complete
zeroth order zonal velocity field for the Kelvin wave is given by

$$u \sim c^{-3/4}e^{-\xi^2/2}e^{i\hat{z}} \qquad (5.44)$$

with

$$c = \frac{\omega}{k} - U + i\frac{r}{k} \qquad (5.45)$$

and

$$f(\tau) = \frac{N}{c} \qquad (5.46)$$

$$l = l_0\left(1 - i\frac{1}{2}Ri^{-1/2}\right) \qquad (5.47)$$

$$l_0 = \left(\frac{c}{\beta}\right)^{1/2} \tag{5.48}$$

where ω and k are given Kelvin wave frequency and zonal wavenumbers, respectively. Notice that c is in general a complex quantity whose real part is the Doppler shifted phase speed of the wave (ω/k is the phase speed relative to the ground).

The solution (5.44) has an amplitude factor $c^{-3/4}$ which depends on the "slow" variable τ and accounts not only for the usual WKB scaling factor arising due to the changes in the medium, but also for the effects of changing meridional scale $l(\tau)$. As the waves propagate into regions of decreasing meridional scale, conservation of the total wave energy implies an increase in the amplitudes. This also explains why, even for c real, lines of constant phase on the y-z plane are not straight lines as it is the case for Kelvin waves on a motionless basic state. In the absence of friction, the amplitude becomes infinitely large as the wave approaches a critical level, where the phase speed is Doppler shifted to zero by the mean flow (i.e., $\omega/k = U$). At these critical levels, considerable transfer of momentum takes place from the waves to the mean flow (see, e.g., Holton, 1975).

Let us consider a simple linear shear profile of the form

$$U = U_0 + \epsilon z \tag{5.49}$$

where U_0 is the amplitude of the mean flow at the surface. The phase factor $\hat{z}$ contains real and imaginary parts which can be determined by performing the integral

$$\hat{z} = \int_0^z \frac{N}{c} dz' \tag{5.50}$$

The complex valued integral can be split into two integrals over real functions of z, whose evaluation leads to the result

$$\hat{z} = -\frac{N}{2\epsilon} \ln\left(\frac{c_r^2 + c_i^2}{c_{r_0} + c_i}\right) - i\frac{N}{\epsilon}\left[\tan^{-1}\left(-\frac{c_r}{c_i}\right) - \tan^{-1}\left(-\frac{c_{r_0}}{c_i}\right)\right] \tag{5.51}$$

160

where c_r and c_i are the real and imaginary parts of c, as expressed in (5.45), and c_{r_0} denotes the value of c_r at $z = 0$. The second term reflects the frictional decay of the wave energy in the vertical. Taking into account the fact that the amplitude factor $c^{-3/4}$ is also complex, the z dependence of solution (5.44) can be written in the form

$$u \sim A(z)e^{i\theta(z)} \tag{5.52}$$

where $A(z)$ is the real amplitude given within a constant by

$$A(z) \sim (c_r^2 + c_i^2)^{-3/8} \exp\left\{\frac{N}{\epsilon}\left[\tan^{-1}\left(-\frac{c_r}{c_i}\right) - \tan^{-1}\left(-\frac{c_{r_0}}{c_i}\right)\right]\right\} \tag{5.53}$$

and $\theta(z)$ is the real quantity

$$\theta(z) = -\frac{N}{2\epsilon}\ln\left(\frac{c_r^2 + c_i^2}{c_{r_0} + c_i}\right) + \frac{3}{4}\tan^{-1}\frac{c_i}{c_r} \tag{5.54}$$

The exponential factor in $A(z)$ represents the effects of friction on the amplitude and it is equal to one for the frictionless case ($c_i = 0$). To get a measure of the local wavenumber m_l, we may take the derivative $\theta'(z)$ to obtain

$$m_l = \frac{Nc_r}{c_r^2 + c_i^2} - \frac{3}{4}\frac{\epsilon c_i}{c_r^2 + c_i^2} \tag{5.55}$$

Except for an order ϵ correction, the local vertical wavenumber is just equal to the real part of f in (5.46).

The stationary Kelvin waves studied in section 5.8 were embedded in a constant 10 cm/s mean westward flow. To see how those solutions are modified by the presence of vertical shear, here we shall take surface currents of the same magnitude by choosing $U_0 = -10$ cm/s in (5.49). We examine first a case of relatively weak shear, letting $\epsilon = -2 \times 10^{-5}\,s^{-1}$ in (5.49). These choices correspond to a 10 cm/s surface westward current linearly decreasing to zero at 5000 m. Figure 5.15 displays how the zonal velocity amplitude and vertical scale change with depth, as computed from the asymptotic expressions (5.53) and (5.54) for the case of a stationary ($\omega = 0$) Kelvin
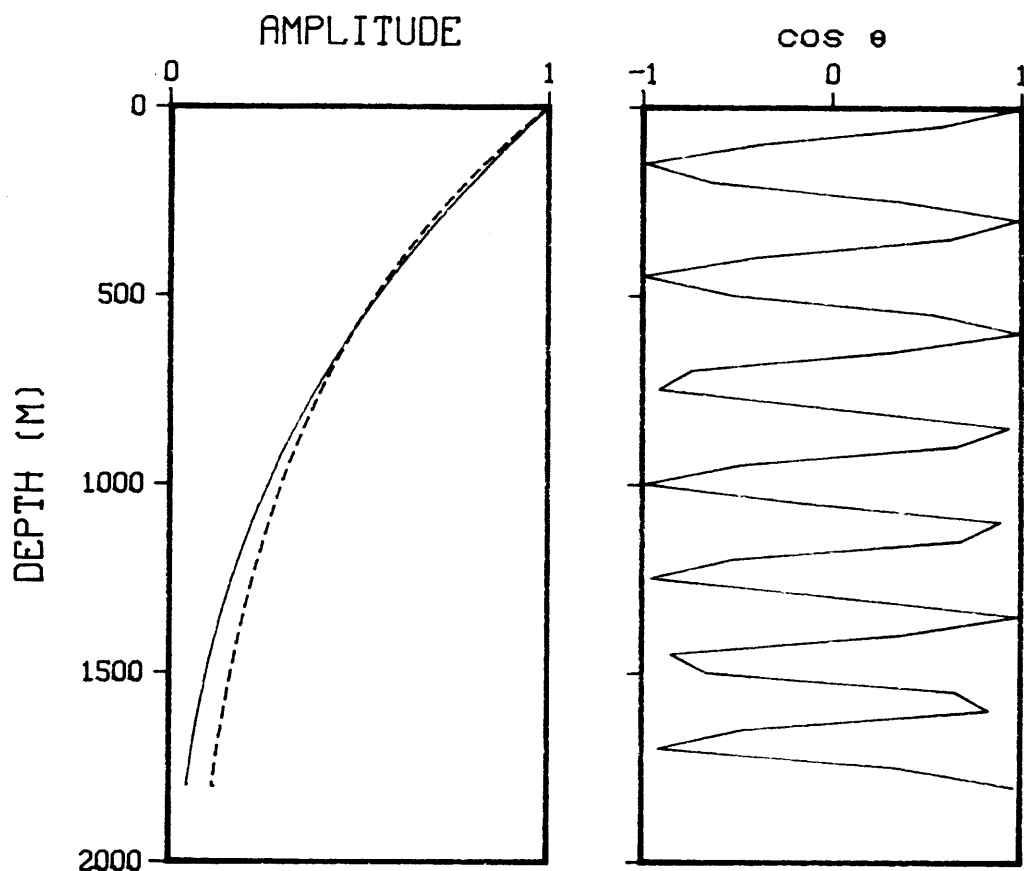
Fig. 5.15. Plots of amplitude $A(z)$ and $\cos\theta(z)$, as given by expressions (5.53) and (5.54), for a stationary Kelvin wave in the shear flow defined in the text. The dashed line represents the amplitude of a stationary Kelvin wave with *constant* vertical wavelength of 315 m, as if it were embedded in constant mean flow. The spiky lines in the right panel are due to the coarse resolution of the plot.

162

wave, with zonal wavelength of 12000 km. The spindown time (10 years) and the value of N are the same as before. Also shown for comparison is the amplitude as a function of depth for the case of a stationary Kelvin wave of the same zonal scale, but embedded in *constant* mean flow. Both amplitudes are normalized by their surface values. The two curves follow each other rather closely, with amplitudes in the shear case being slightly higher near the top and the reverse being true below roughly 600 m. This is connected in part to the decrease in vertical scale with depth, from a local vertical wavelength (as computed from (5.55)) of 315 m at the surface to 210 m at 1800 m, in the shear case. The factor $(c_r^2 + c_i^2)^{-3/8}$ in (5.53), which expresses the effect of shear on $A(z)$, increases with depth and compensates somewhat for the frictional decay. Thus, the shear amplitudes are higher close to the surface. At the same time, an increasing m_l implies slower vertical group speeds. Therefore at depths where the vertical wavelength has become small enough to significantly change the rate of vertical energy propagation, amplitudes of the waves in shear will decay faster than if they were in a constant mean flow. The meridional scale of the wave l_0 decreases with depth like $c^{1/2}$, as given by (5.48). The relevant difference between the sheared and constant U cases, as portrayed in Fig. 5.15, is not so much the different amplitudes, but rather the relatively large changes in the vertical scale with depth, present even for such small vertical shear.

In Fig. 5.16 we show the effect of increasing the shear by letting $U_0 = -20$ cm/s and $\epsilon = -4 \times 10^{-5} \, s^{-1}$. Now, the forced vertical wavelength at the surface has doubled to roughly 630 m and the depth of energy penetration is much greater because larger vertical scales imply larger downward vertical group speeds. The difference in amplitudes between the shear and no shear cases are now more apparent. Also more rapid is the change in vertical scale with depth, with estimates of the local vertical wavelength going from 630 m at the surface to roughly 200 m at depth. This example illustrates how the presence of shear allows for the existence at large depths of relatively
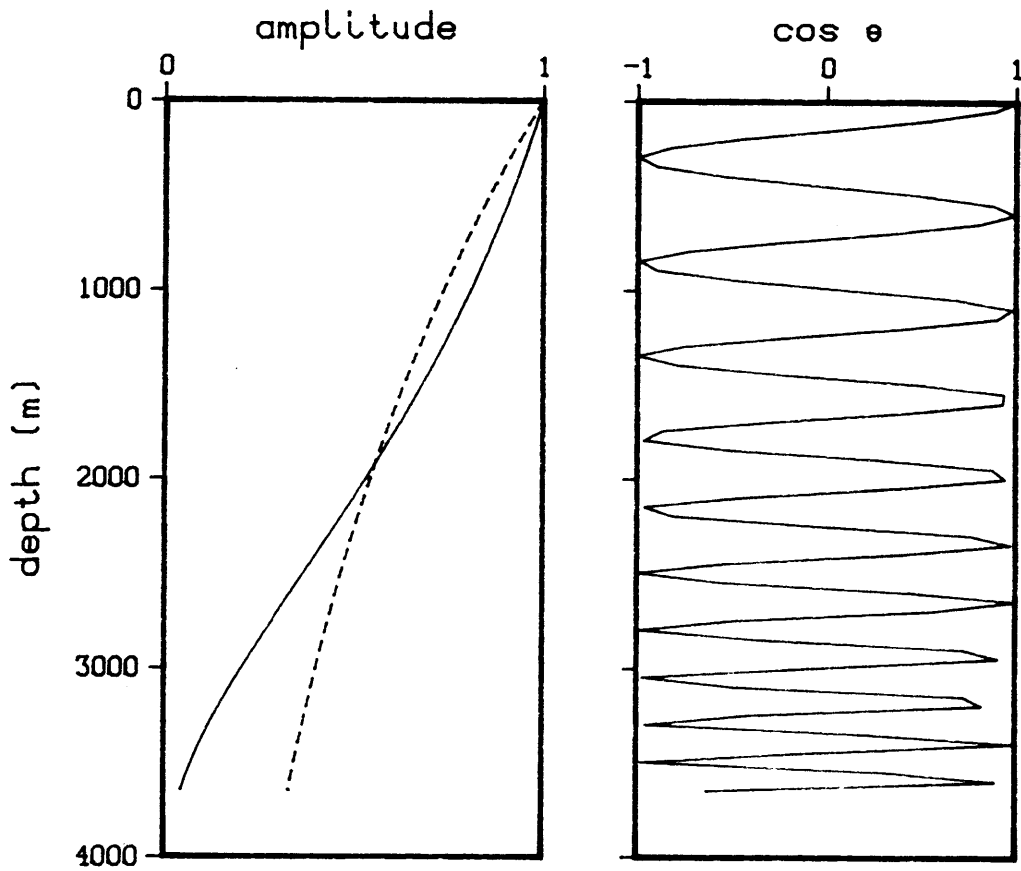
Fig. 5.16. Same as in Fig. 5.15 but for a mean flow with a surface value of -20 cm/s and linearly decreasing to zero at 5000 m.

164

short vertical wavelengths, with considerable amplitudes. For constant mean flows, the presence of the same short scales with the same amplitudes at depth requires much smaller values for the linear damping coefficient r. In shear flow, the surface current U_0 is not the only important parameter in setting the vertical scale of the solution as it is in the constant U case. The actual shape of the shear profile chosen determines how the vertical scale of the wave adjusts with depth. For the shear in (5.49) this adjustment is linear, while for other profiles where shear is mostly concentrated at particular depths, sharp changes in the wave scales and amplitudes may occur over small regions (in fact, such cases may violate the multiple scale assumption).

For the shears used in Figs. 5.15 and 5.16, the presence of damping causes a relatively smooth decay of wave amplitude with depth. This implies in turn a divergence of the total vertical momentum flux, meaning the Kelvin waves are depositing eastward momentum on the mean flow over a broad range of depths (Holton, 1975). This forcing of the mean flow by the eddy fluxes would tend to erode the westward mean current in a more or less uniform way in depth, unless the waves encounter regions of strong shear or critical levels where sharp absorption occurs. For the mean flows considered so far, the critical level occurs at 5000 m (depth at which $U = 0$), and the stationary Kelvin waves are damped well before reaching such depth. However, perhaps a more realistic representation of the flows associated with the equatorial Intermediate current would take the mean westward flow to decay to zero at considerably shallower depths. Fig. 5.17 shows the case where we let $U_0 = -10$ cm/s and $\epsilon = 10^{-4}s^{-1}$, for which $U = 0$ at 1000 m. Here, we plot the local vertical wavelength instead of $\cos\theta(z)$. Near critical levels we may question the validity of the asymptotic formulas used here, but for sufficiently strong damping, Lindzen (1971) found his asymptotic results to be in close agreement with numerical calculations. In any case, the results in Fig. 5.17 can be taken as a qualitative statement of what happens when critical levels are closer to the surface. The Kelvin wave is strongly damped as it approaches the critical layer,
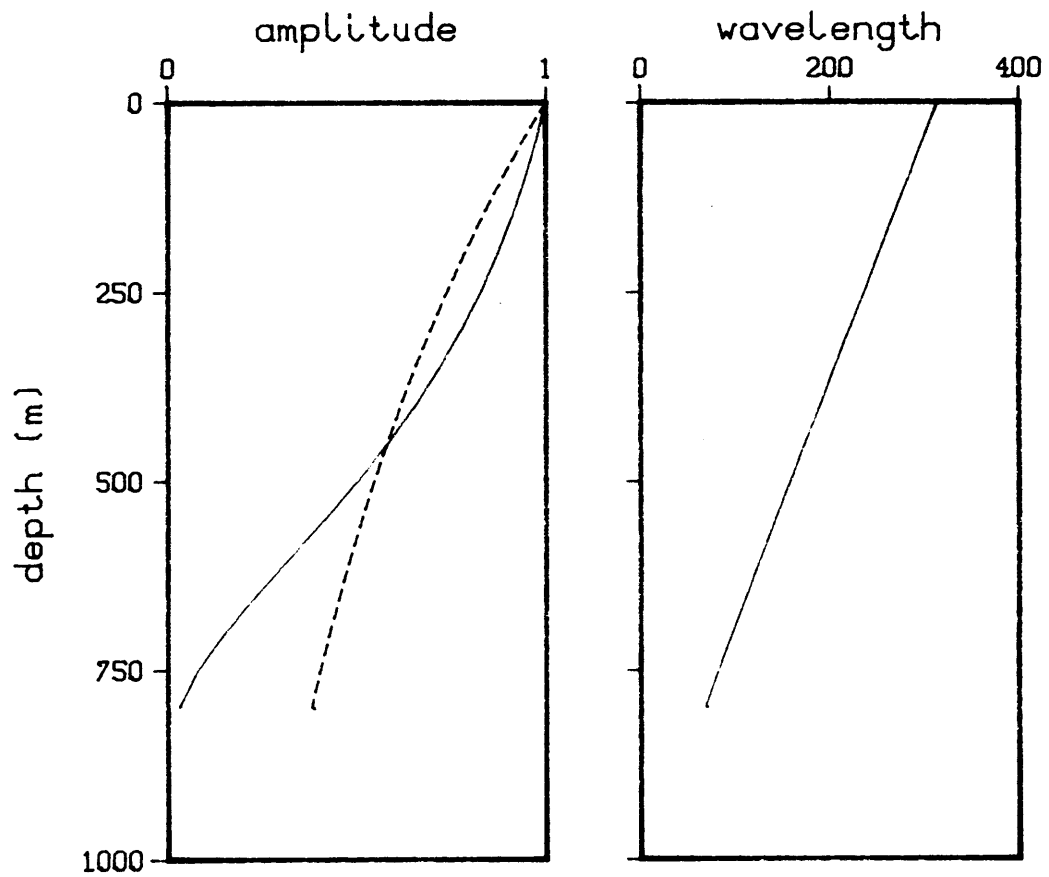
Fig. 5.17. Same as in Fig. 5.15 but for the case of a mean shear with a critical layer at 1000 m. Here, it was convenient to plot the vertical wavelength as a function of depth.

166

because of the quick vanishing of its vertical wavelength and vertical group velocity. For weaker friction the wave would be absorbed closer to the critical level at 1000 m and over a shorter region. The amount of damping essentially determines the vertical extent of the strong absorption region above the critical layer.

5.10 Discussion

The presence of a mean westward flow below the Undercurrent proves to be important in establishing short vertical scale deep alternating zonal flows directly underneath the forcing region, with no need for reflections from oceanic lateral walls. These flows are associated with stationary Kelvin waves as in McCreary and Lukas (1986). The effect of mean vertical shear is basically twofold: it changes the vertical and meridional scales of the waves with depth, as well as the amplitudes; and it provides for the possibility of critical layer absorption to occur. These effects are very much dependent on the actual shear profile.

The rate at which Kelvin waves of a given vertical scale propagate energy downward is the same whether or not they are embedded in mean zonal flow. Therefore, if the magnitude of U at the forcing region is such that short vertical wavelengths are generated, for reasonable amounts of friction, the associated wave energy is still strongly trapped to the upper layers in contrast with the general character of the observations. This is what we found when assuming values of $U_0 = -10$ cm/s in both shear and no shear cases. For faster surface flows, the energy penetration is improved because of the larger vertical scales at the surface, with the shear adjusted wavelengths becoming smaller with depth. We may argue that a spindown time of ten years is too short, and that by just doubling its value we would double the vertical decay scale of the wave energy. However, regardless of the amount of friction in the solutions, the probable occurrance of relatively shallow critical layers provides a more fundamental barrier to the penetration of Kelvin wave energy to great depths. Unless the mean westward

flows extend considerably deeper than one thousand meters below the Undercurrent, the role of stationary Kelvin waves in deep jet dynamics becomes somewhat doubtful.

On the other hand, the existence of shallow critical layers raises the possibility of having strong forcing of mean flows due to large divergence of wave momentum fluxes at those levels. Previous authors (Philander and Pacanowski, 1981; McPhaden *et al.*, 1986) have suggested the possibility of the equatorial jets being mean currents generated by waves. In fact, atmospheric phenomena such as the quasi-biennial oscillation have been attributed to the interplay between vertically propagating equatorial waves and the mean flow (Holton, 1975). As a qualitative description of what might happen in our case, the absorption of Kelvin waves at a critical level would lead to the generation of mean eastward flows which would migrate upward due to the implicit shifting of the critical level in the same direction. The process would eventually cause a complete replacement of the originally present westward flow by eastward flow. One could continue to speculate on these lines, bringing in other stationary equatorial waves (carrying westward momentum downward) to reverse the process, but such discussion would be premature.

On the general issue of wave-mean flow interactions as a generating mechanism for the deep jets, the above comments suggest that fairly elaborate interaction processes can perhaps occur in the ocean, depending on the existence of a given spectrum of waves and some initial shear profile. One might remark though that if the alternating currents in the records are indeed mean flows forced by propagating waves, it would require both easterly and westerly waves to generate them. Provided that such waves exist and are able to provide the necessary accelerations to the mean flow, it is still far from obvious how a multiple cell structure of alternating currents could evolve and be maintained in such fashion, since in general the first double cell would serve as an efficient absorber of most of the energy carried down by the waves.

CHAPTER 6
General conclusions and remarks

This final chapter provides a summary of the main results and conclusions drawn from the work described in detail in the previous chapters. It discusses the more general implications of our findings and defines some of the relevant issues that should be addressed in the future, if one is to improve the present knowledge and understanding of the deep equatorial circulation.

The PEQUOD data set analyzed here revealed some surprising features of the equatorial central Pacific deep circulation. Instead of a single dominant vertical scale in the zonal velocity records, spectral analysis unveiled two narrow band peaks centered at vertical wavelengths of 560 sm and 350 sm. The first was not apparent from visual inspection of the raw records, while the second corresponded to the conspicuous wiggles in the vertical profiles of zonal current, previously observed in other records and normally referred to as the equatorial deep jets. Both signals were present in the data from all three cruises, with the 350 sm peak showing remarkable little amplitude change in time. There was a significant increase in energy at the 560 sm feature occurring between the first and last cruises.

Time and space scales associated with the 560 sm signal seemed consistent, within error bars, with the presence of a first meridional mode long Rossby wave packet, propagating energy downward at periods of about four years, and with zonal wavelengths on the order of 10000 km. Preliminary calculations recently done by Firing (private communication) on his time series of profiles at 159°W (Firing, 1987) suggest the presence in those records of upward phase propagation at similar vertical wavelengths. His estimates on the order of three years for the period seem to independently confirm our findings.

The equatorial deep jets, identified with the peak centered at 350 sm, are best defined as a finite narrow band process in vertical wavenumber (311-400 sm), embedded in a broad band energetic background, and accounting for only 20% of the total variance in the records. A general tilt of phase lines downward towards the east at the jets wavenumber band yielded estimates of 10000-16000 km for their zonal wavelengths. The jets shifted coherently in the vertical during PEQUOD, but definitive determination of their apparent interannual time scales would require records much longer than the ones used here (on the other of at least five years). Although the PEQUOD observations are not conclusive about whether the deep jets are really associated with equatorial waves or not, they do not preclude the linear wave hypothesis either. We showed how finite bandwidth (in frequency and wavenumber) Kelvin wave processes of periods on the order of three to five years could account for the observations. Thus, these relatively simple linear wave processes remain a plausible explanation for the jets.

Although the linear wave interpretation of the two signals seems more robust for the 560 sm peak than for the deep jets peak, it is nevertheless important to stress the apparent evidence in both cases for waves at interannual time scales. Considerable Rossby wave energy at periods long compared to one year has been observed in the North Pacific (e.g., Magaard (1983) found a peak in potential energy spectra at periods of roughly seven years, from records covering the area 20-25°N and 130-175°W). More recently, records analyzed by White (private communication) suggested that off-equatorial (i.e., 10° latitude) interannual Rossby wave activity is connected to the onset of El Niño events. Our results indicate the general importance of long time scale wave motions in the whole equatorial region. The signals observed in the PEQUOD records may be the deep ocean manifestation of the strong interannual variability present in the upper ocean and associated with El Niño.

In light of the long time scale of the narrow band signals, the broad band character of the energetic background and the opposing directions of phase and group velocity

for equatorial waves, extremely careful judgement is needed when inferring vertical propagation from the data. It is perhaps not surprising that systematic and coherent vertical shifts of the deep jets have been so elusive. In fact, the solutions discussed in Chapter 5 (where both upward and downward vertical phase propagation occur across different energy rays) may suggest that clear evidence for propagation will be difficult to document, even with records longer than the ones considered here.

Analysis of the background spectra of velocity and vertical displacement records showed in general the decay of energy away from the equator, as expected for equatorially trapped wave fields. This decay was most evident in the velocity records. The decay scales for u and ς were much broader than the Kelvin wave scaling at each vertical wavenumber, suggesting the existence of Rossby waves in the records. Zonal velocity records were apparently dominated by broad band Rossby and Kelvin wave activity in the 933 sm and 140-400 sm bands, respectively. This latter result is strikingly similar to the findings of Eriksen (1981) and seems to define a climatological feature of the deep equatorial Pacific fields.

The theoretical work in Chapter 5 was in part motivated by the basic linear wave signature of both zonal velocity signals displayed in the records and by the recent works of McCreary and Lukas (1986) and Kawase (1987). Deep energy sources located at the oceanic lateral boundaries or mean westward deep flows below the EUC were both found to be potentially important to the existence of deep baroclinic currents in the equatorial ocean. In the first case, boundary forced low frequency Kelvin or long Rossby waves can propagate into the interior, giving rise to flows with vertical scales essentially determined by the vertical extent of the forcing. By assuming a deep energy source, in one case presumably associated with deep water mass formation processes as suggested by Kawase (1987), one conveniently avoids the difficulty of propagating energy downward from the surface at low frequencies. The existence of mean westward

flows below the EUC allows in turn for resonating Kelvin waves to dominate the solutions in the deep ocean. Large scale convergence or divergence patterns associated with upper ocean currents such as the EUC may be the forcing mechanism in this case. In contrast with solutions using constant mean flows, the presence of vertical shear cause the vertical scale of the stationary Kelvin waves to decrease with depth, allowing for the existence at large depths of relatively short vertical wavelengths, even with moderate amounts of damping. Another consequence of having sheared flows is the possible occurrance of strong wave absorption at critical layers. In the case of shallow critical layers, the damping of the wave prevents it from playing any role in the deep ocean solutions.

There is one common aspect to the two different ideas explored in Chapter 5. In both cases, direct surface wind forcing is not considered to be the primary mechanisn for generating the deep ocean velocity fields, but instead we let the side walls and the sub-thermocline region perform that task. The ultimate source of energy obviously lies at the ocean surface. However, the energy input at the top can follow very different and sometimes not so obvious paths to reach the deep ocean, as the work of Kawase (1987) illustrates. Just as deep water formation processes may influence the equatorial band, perhaps the same can be said of the sub-tropical circulation. The connection between these two flow regimes (tropical and sub-tropical) has recently been made by Pedlosky (1987). His work is an extension of the ventilated thermocline model to the equator, where the Sverdrup relation breaks down and relative vorticity becomes important. The two layer model produces a sub-tropical gyre flow converging on the equator, and turning into a strong eastward jet (an inertial undercurrent) close to the equator where the dynamics become nonlinear. The relevant idea is that flows impinging on the equator and conserving potential vorticity may acquire a strong zonal signature, as originally pointed out by Fofonoff and Montgomery (1955). In the case of a stratified ocean, these zonal flows may be sheared in the vertical. A related issue is

what would be the response of the equatorial band to seasonal or interannual oscillations occurring at higher latitudes. Whether such steady and time varying components of the sub-tropical circulation are significant to the deep equatorial circulation remains an interesting question.

The clear need for improved data sets in the future is one of the outcomes of this discussion. More observations for example are necessary to resolve the mean and time dependent components of the deep circulation, or to test the validity of theoretical models of features such as the EDJ. For instance, in light of the ideas presented here, it would be important to establish observationally the existence of a mean westward flow below the EUC and determine its amplitude and vertical structure. Collection of basin wide equatorial transects of deep zonal velocity and intense observations along the western or eastern boundaries would shed some light on whether the jets can be traced to deep energy sources located at the oceanic side walls, as hypothesized in Chapter 5. Furthermore, knowledge of the mean and time dependent component of the deep circulation is crucial in studies of instability or wave-mean flow interaction phenomena. These may be relevant to the existence of energetic motions at particular scales like the ones found in the PEQUOD records.

In addition to trying to explore the possible connection between the sub-tropical intermediate and deep circulation and the equatorial circulation, or attempting insta- bility and wave-mean flow interaction studies, another fair way to proceed is to develop numerical models with sufficient vertical resolution to study the deep circulation and see under.what circumstances they develop flow patterns resembling the available ob- servations. With the recent exception of Kawase (private communication), all previous efforts in the tropics have focused on the study of roughly the upper 500 meters of the ocean, essentially neglecting the bottom portion of the water column. A particu- lar challenge to these numerical models would be to reproduce the short vertical scale zonal flows associated with the deep jets.

In the course of this work considerable new knowledge and insight was gained on the character of the deep fields in the central equatorial Pacific region, especially with regard to the energetic short vertical scale zonal flows. In trying to explain the records, emphasis was purposefully put on simple ideas and processes, but much observational and theoretical work remains to be done in the future before a better understanding of the subject is achieved. There is a fair possibility that a considerably improved overall picture of the deep equatorial circulation may emerge from the upcoming observational program being planned for the tropics, in the context of the World Ocean Circulation Experiment. Perhaps then will some of the questions raised here be answered more decisively.

APPENDIX A
Short Review of Linear Equatorial Wave Theory

Linear equatorial wave theory has been known for quite some time and numerous articles have treated it in detail. Moore and Philander (1976) and McCreary (1985) provide good reviews on the subject. As a quick reference to the reader, here we briefly outline the relevant aspects of the theory.

The linearized, Boussinesq, equatorial β-plane equations are

$$u_t - \beta y v + p_x = 0 \qquad\qquad (A.1a)$$

$$v_t + \beta y u + p_y = 0 \qquad\qquad (A.1b)$$

$$p_z + g\frac{\rho'}{\rho_0} = 0 \qquad\qquad (A.1c)$$

$$\rho'_t + w\rho_z = 0 \qquad\qquad (A.1d)$$

$$u_x + v_y + w_z = 0 \qquad\qquad (A.1e)$$

where conventional notation is used. The mean stratification ρ is a function of z only and the buoyancy frequency N is defined as $N^2 = -(g/\rho_0)\rho_z$.

Using the polarization relations

$$\begin{bmatrix} u \\ v \\ w \\ p \end{bmatrix} = Ae^{i(kx-\omega t)} \begin{bmatrix} U(y)G'(z) \\ iV(y)G'(z) \\ iW(y)G(z) \\ c_n P(y)G'(z) \end{bmatrix} \qquad\qquad (A.2)$$

in equations $(A.1)$ leads to the separation of the horizontal and vertical problem, with c_n being the separation constant. The function $G(z)$ is a solution of the vertical structure equation

$$G''(z) + \frac{N^2(z)}{c_n^2}G(z) = 0 \qquad\qquad (A.3)$$

subject to the boundary conditions $G = 0$ at the bottom, and $G = 0$ (rigid surface) or $G'(z) - (g/c_n^2)G(z) = 0$ (free surface) at $z = 0$. The horizontal structure equation in terms of $V(y)$, and using the nondimensional variables

$$\eta = (\frac{\beta}{c_n})^{1/2}y, \quad \sigma = \frac{\omega}{\beta c_n^{1/2}}, \quad s = (\frac{c_n}{\beta})^{1/2}k \qquad (A.4)$$

is

$$V_{\eta\eta} + [\sigma^2 - s^2 - (\frac{s}{\sigma}) - \eta^2]V = 0 \qquad (A.5)$$

Solutions to this equation which decay away from the equator are known to be the Hermite functions

$$\psi_j(\eta) = \frac{e^{-\frac{\eta^2}{2}}H_j(\eta)}{(2^j j!\pi)^{1/2}} \qquad (A.6)$$

where $H_j(\eta)$ are Hermite polynomials. The free modes obey the dispersion relation

$$\sigma^2 - s^2 - \frac{s}{\sigma} = 2j + 1 \qquad (A.7)$$

which is cubic in σ (for a plot of $(A.7)$ see for example Wunsch and Gill (1976)). General solutions to $(A.5)$ take the form

$$V_j(\eta) = A_j\psi_j(\eta) \qquad (A.8a)$$

$$U_j(\eta) = -A_j\left[\frac{(\frac{j}{2})^{1/2}\psi_{j-1}}{\sigma + s} + \frac{(\frac{j+1}{2})^{1/2}\psi_{j+1}}{\sigma - s}\right] \qquad (A.8b)$$

$$P_j(\eta) = A_j\left[\frac{(\frac{j}{2})^{1/2}\psi_{j-1}}{\sigma + s} - \frac{(\frac{j+1}{2})^{1/2}\psi_{j+1}}{\sigma - s}\right] \qquad (A.8c)$$

where j is the meridional mode number. For $j \geq 1$, these are called Rossby waves (small σ) and gravity waves (large σ).

For the case $j = 0$, solutions yield the mixed Rossby-gravity wave, with dispersion relation

$$\sigma - \frac{1}{\sigma} = s \qquad (A.9)$$

Another special solution obtained by setting $v = 0$ in $(A.1)$ is called a Kelvin wave, with wave functions given by

$$U_{-1}(\eta) = A_{-1}\psi_0 \qquad\qquad (A.10a)$$

$$V_{-1}(\eta) = 0 \qquad\qquad (A.10b)$$

$$P_{-1}(\eta) = A_{-1}\psi_0 \qquad\qquad (A.10c)$$

and dispersion relation

$$\sigma = s \qquad\qquad (A.11)$$

A detailed description of these different waves and their dynamical fields can be found in Gill (1982). It is relevant to notice here that for each wave, the zonal velocity and the pressure variables have the opposite symmetry of the meridional velocity. Waves having a zonal velocity signal at the equator, do not contribute to the meridional velocity signal and vice-versa.

References

Blandford, R., 1966. Mixed gravity-Rossby waves in the ocean. *Deep-Sea Research*, *13*, 941-961.

Boyd, J. P., 1980. The nonlinear equatorial Kelvin wave. *J. Phys. Oceanog.*, *10*, 1-11.

Boyd, J. P. and Z. D. Christidis, 1982. Low wavenumber instability on the equatorial beta-plane. *Geophysical Research Letters*, *9*, 769-772.

Boyd, J. P. and Z. D. Christidis, 1983. Instability on the equatorial beta-plane. In: *Hydrodynamics of the Equatorial Ocean*, J. C. J. Nihoul, editor, Elsevier Science Publishers, Amsterdam, pp. 339-351.

Cane, M. A. and S. E. Zebiak, 1985. A theory for El Niño and the Southern Oscillation. *Science*, *228*, 1085-1086.

Eriksen, C. C., 1980. Evidence for a continuous spectrum of equatorial waves in the Indian Ocean. *J. Geophys. Res.*, *85*, 3285-3303.

Eriksen, C. C., 1981. Deep currents and their interpretation as equatorial waves in the Western Pacific Ocean. *J. Phys. Oceanog.*, *11*, 48-70.

Eriksen, C. C., 1982. Geostrophic equatorial deep currents. *J. Marine Research, Supplement to 40*, 143-157.

Eriksen, C. C., 1985. Moored observations of deep low-frequency motions in the Central Pacific: Vertical structure and interpretation as equatorial waves. *J. Phys. Oceanog.*, *15*, 1085-1113.

Firing, E., 1987. Deep zonal currents in the central equatorial Pacific. *J. Marine Research*, *45*, 791-812.

Fofonoff, N. P., and R. B. Montgomery, 1955. The equatorial undercurrent in the light of the vorticity equation. *Tellus*, *VII*, 518-521.

Garrett, C., and W. H. Munk, 1979. Internal waves in the ocean. *Annu. Rev. Fluid Mech.*, *11*, 339-369.

Gradshteyn, I. S., and I. M. Ryzhik, 1965. *Table of Integrals, Series and Products*, 4th ed. Academic Press, 1086 pp.

Gent, P., and J. R. Luyten, 1985. How much energy propagates vertically in the equatorial ocean? *J. Phys. Oceanog.*, *15*, 997-1007.

Gill, A. E., 1982. *Atmosphere-Ocean Dynamics*. Academic Press, Inc., New York, New York, 662 pp.

Goldenberg, S. G., and J. J. O'Brien, 1981. Time and space variability of tropical Pacific wind stress. *Mon. Wea. Rev.*, *109*, 1190-1207.

Hayashi, Y.-Y., and W. R. Young, 1987. Stable and unstable shear modes of rotating parallel flows in shallow water. *J. Fluid Mech.*, *184*, 477-504.

Hayes, S. P., and H. B. Milburn, 1980. On the vertical structure of velocity in the Eastern Equatorial Pacific. *J. Phys. Oceanog., 10*, 633-635.

Holton, J. R., 1975. *The Dynamic Meteorology of the Stratosphere and Mesosphere.* Vol. 15, No. 37, Amer. Meteor. Soc., 218 pp.

Kawase, M., 1987. Establishment of deep ocean circulation driven by deep water production. *J. Phys. Oceanogr.,* in press.

Koopmans, L. H., 1974. *The Spectral Analysis of Time Series.* Academic Press, 366 pp.

Leetmaa, A. and P. F. Spain, 1981. Results from a velocity transect along the equator from 125 to 159 W. *J. Phys. Oceanog., 11*, 1030-1033.

Lighthill, M. J., 1978. *Waves in Fluids.* Cambridge University Press, Cambridge, Great Britain, 504 pp.

Lindzen, R. S., 1971. Equatorial planetary waves in shear: Part I. *J. Atmos. Sci., 27*, 609-622.

Lukas, R., and E. Firing, 1985. The annual Rossby wave in the central equatorial Pacific ocean. *J. Phys. Oceanogr., 15*, 55-67.

Luther, D. S., and D. E. Harrison, 1984. Observing long-period fluctuations of surface winds in the tropical Pacific: initial results from island data. *Mon. Wea. Rev., 112*, 285-302.

Luyten, J. R., and J. C. Swallow, 1976. Equatorial undercurrents. *Deep-Sea Research, 23*, 1005-1007.

Luyten, J. R., G. Needell and J. Thomson, 1982. An acoustic dropsonde — design, performance and evaluation. *Deep-Sea Research, 29*, 499-524.

McCreary, J. P., 1981. A linear stratified ocean model of the Equatorial Undercurrent. *Phil. Trans. Roy. Soc. London, A298*, 603-635.

McCreary, J. P., 1984. Equatorial beams. *J. Marine Research, 42*, 395-430.

McCreary, J. P., 1985. Modeling the equatorial ocean circulation. *Ann. Rev. Fluid Mech., 17*, 359-409.

McCreary, J. P. and R. Lukas, 1986. The response of the equatorial ocean to a moving wind field. *J. Geophys. Res., 91*, 11691-11705.

McPhaden, M. J., 1981. Continuously stratified models of the steady-state equatorial ocean. *J. Phys. Oceanogr., 11*, 337-354.

McPhaden, M. J., J. A. Proehl and L. M. Rothstein, 1986. The interaction of equatorial Kelvin waves with realistically sheared zonal currents. *J. Phys. Oceanogr., 16*, 1499-1515.

Moore, D. W. and S. G. H. Philander, 1976. Modeling of the tropical oceanic circulation. *The Sea: Ideas and Observations on Progress in the Study of the Seas,* Vol.

6, Marine Modeling, E. D. Goldberg, I. N. McCave, J. J. O'Brien and J. H. Steele, Eds., John Wiley, Interscience, 319-361.

O'Neill, K., 1982. Observations of vertically propagating equatorially-trapped waves in the deep Western Indian Ocean. *Woods Hole Oceanographic Institution Tech. Rep. WHOI-82-II.*

Pedlosky, J., 1987. An inertial theory of the Equatorial Undercurrent. *J. Phys. Oceanog., 17,* 1978-1985.

Philander, S. G. H., 1976. Instabilities of zonal equatorial currents, I. *J. Geophys. Research, 81,* 3725-3735.

Philander, S. G. H., 1978. Instabilities of zonal equatorial currents, II. *J. Geophys. Research, 83,* 3679-3682.

Philander, S. G. H., 1979. Comments on deep equatorial currents. (unpublished manuscript)

Philander, S. G. H. and R. C. Pacanowski, 1981. Response of equatorial oceans to periodic forcing. *J. Geophys. Res., 86,* 1903-1916.

Philander, S. G. H. and R. C. Pacanowski, 1984. Simulation of the seasonal cycle in the tropical Atlantic Ocean. *Geophys. Res. Lett., 11,* 802-804.

Ponte, R. M., 1986. The statistics of extremes, with application to El Niño. *Reviews of Geophysics, 24,* 285-297.

Stommel, H., 1960. Wind drift near the equator. *Deep-Sea Research, 6,* 208-302.

Taft, B. A., B. M. Hickey, C. Wunsch and D. J. Baker,Jr., 1974. Equatorial Undercurrent and deeper flows in the central Pacific. *Deep-Sea Research, 21,* 403-430.

Voorhis, A., J. R. Luyten, G. Needell and J. Thomson, 1984. Wind forced variability of the upper ocean dynamics in the Central Equatorial Pacific during PEQUOD. *J. Phys. Oceanog., 14,* 615-622.

Warren, B. A., 1981. The deep circulation of the world ocean. In: *Evolution of Physical Oceanography,* The MIT Press, Cambridge, 623 pp.

Weiss, R. F., J. L. Bullister, R. H. Gammon, and M. J. Warner, 1985. Atmospheric chlorofluoromethanes in the deep equatorial Atlantic. *Nature, 314,* 608-610.

Wunsch, C., 1977. Response of an equatorial ocean to a periodic monsoon. *J. Phys. Oceanog., 7,* 497-511.

Wunsch, C. and A. E. Gill, 1976. Observations of equatorially trapped waves in Pacific sea level variations. *Deep-Sea Research, 23,* 371-390.

Acknowledgements

Since the very first days of my tenure as MIT/WHOI student, many people helped me endure the tribulations of this very long journey. I would like to thank my advisor, James Luyten, for giving me all the support and encouragement without which this dissertation could not have been completed. Our quasi-biweekly discussions provided me with the energy to climb some of the steepest hills standing on my way. His guidance was essential to keep me on the right track. I would also like to thank my advisor for the first three years in the Joint Program, Carl Wunsch, for helping me develop my scientific skills during that crucial period. As a member of my Ph.D. thesis committee, he provided many useful insights and generously shared his own views and ideas on how to proceed. Comments and suggestions from the remaining members of the committee, Glenn Flierl, Joseph Pedlosky and John Toole, were important in improving the clarity of this dissertation.

The much needed computer assistance was provided by Charmaine King, Gerald Needell and Susan Johnson. Bud Brown helped with some of the figures. I also can not forget all the dwellers of the 13th floor in the Green Building since September 1982, who helped make my stay at MIT a very enjoyable experience (thanks for the scientific discussions, the computer tutorials, the tea hour cookies, the tennis practices and, above all, the many good laughs). This includes, of course, my student colleagues, from whom I learned a great deal over the years.

I have saved the last words to express my deepest gratitude to my parents, Plínio Ponte and Celina Melo, for all they have done over the years, to my sister Lusa for being always there when I needed, and to my wife Ana for everything (and I really mean everything). This dissertation is dedicated to them.